

**COMPENSATION FOR DISTRIBUTION
OF TIMING AND REFERENCE
SIGNALS OVER OPTICAL FIBRE
NETWORKS FOR TELESCOPE
ARRAYS**

By

Shukree Wassin

Submitted in fulfilment of the requirements for the
degree of

PHILOSOPHIAE DOCTOR

To be awarded at the Nelson Mandela University

April 2018

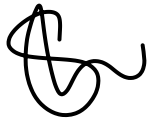
Promoter: Prof T. Gibbon

Co- Promoter: Prof A. W. R. Leitch

Co- Promoter Dr R. R. G. Gamatham

DECLARATION

I, *Shukree Wassin 50316133*, hereby declare that the *thesis* for *PhD* is my own work and that it has not previously been submitted for assessment or completion of any postgraduate qualification to another University or for another qualification.



.....

Shukree Wassin

Official use:

In accordance with Rule G5.6.3,

5.6.3 A treatise/dissertation/thesis must be accompanied by a written declaration on the part of the candidate to the effect that it is his/her own work and that it has not previously been submitted for assessment to an other University or for another qualification. However, material from publications by the candidate may be embodied in a treatise/dissertation/thesis.

DEDICATION

*This thesis is dedicated to my
family*

ACKNOWLEDGEMENTS

بِسْمِ اللَّهِ الرَّحْمَنِ الرَّحِيمِ

(In the name of ALLAH the most Gracious, most Merciful)

I begin by expressing my sincere praise and gratitude unto Almighty ALLAH for giving me the ability to pursue the degree of Philosophiae Doctor in science, and to execute several challenging tasks in life. My many teachers, lecturers and professors have taught me some invaluable lessons during my time spent in the classrooms and lecture venues. However, an important lesson I have learnt during this time is that whilst a certain level of personal intellectual aptitude is required for scientific research, true growth is aided through open dialogue with fellow research peers and mentors. During my lengthy, interesting and at times very difficult journey that started at NMU Missionvale campus (former Vista University), I have been carried by a number of influential individuals who believed in my ability and invested a great amount of their time and effort in me. To Professor Tim Gibbon, words cannot sufficiently express and convey my heart-felt appreciation. From the latter part of my honours year, when you took me under your wing, you have been nothing short of an extraordinary supervisor, promoter, mentor and greater friend. I sincerely thank you. I further thank you for granting me the freedom to express my thoughts and ideas and most important, for not giving up on me at times when even I had given up on myself. To my co-promoters Dr. Romeo Gamatham and Prof. Andrew Leitch thank you for the time and positive input you provided towards my PhD studies. Thank you Mrs McClelland for your words of encouragement, unending support and assistance during my time at the Center for Broadband Communication. I am especially thankful to the academic and administrative staff of the Nelson Mandela University Physics department for their knowledge, support and encouragement during my studies. I would like to take this opportunity to sincerely acknowledge the research funding and equipment support from the following organizations: SKA, ALC, NLC, NRF, DST, Cisco, Telkom, Dartcom, THRIP, NMU and Ingoma Services. There is no way to express how much it meant to me to have been part of the Center for Broadband Communication research group. These brilliant friends and colleagues inspired me over the many years, Dr. Enoch Rotich, Dr. Valentine Chabata, Dr. Duncan Boiyi,

George Isoe, Phumla Dlamini, Kagiso Leburo and all the former Center for Broadband Communication post graduate students. I would like to thank Megan De Jager whose friendship went as far as reading and editing this thesis, thanks Megs. To my two greatest buddies, Lucian and Warren we started this journey together and we're finally ending it the same way we started Lui. The funny thing is, I never appreciated the time we spent on and off campus from our undergrad day, thanks guys. Many thanks for the good and bad times we had, the multitudes of espressos and inter-disciplinary discussions we had and not forgetting all the many arguments. Remember boys, true friends don't say good-bye, we just take extended leave of absences from each other. I would like to thank and express my sincere gratitude to my parents-in-law for their unfailing support and encouragement during my studies. To my dearest mother and father, I thank you for showing faith in me, for your unconditional love, selflessness, patience, prayers, caring and absolute sacrifices you made for education. Although you hardly understood what I did, you were willing to support my decisions. I also express my thanks to my brother and sister for their support and prayers. Finally, to wife Tasneem whom I owe a very special thanks. I'm deeply grateful for your continued patience, sacrifices, unfailing love, positive support, understanding and encouragement during my pursuit of this PhD degree. You were always around at times of difficulty and even when I thought that it was impossible to continue, you helped kept things in perspective. To my kids Madeniyah and Muhammad Taha, I appreciate the patience you showed during the stressful times and while writing the various research papers and most importantly, this thesis. Words cannot express how grateful I am to both of you. I'm blessed to have such a loving and caring family.

Shukree Wassim

CONTENTS

DECLARATION	i
DEDICATION	ii
ACKNOWLEDGEMENTS	iii
ABSTRACT	ix
CHAPTER 1: INTRODUCTION	1
CHAPTER 2: THE SQUARE KILOMETRE ARRAY	
2.1 The journey of the SKA and its key science projects	4
2.2 System design requirements	7
2.3 SKA optical fibre transport network	8
2.4 Synchronization and timing for the SKA	10
2.5 Review of existing synchronization and timing techniques	11
CHAPTER 3: PHASE STABILITY AND FREQUENCY FLUCTUATIONS	
3.1 Timing signals, accuracy and stability	13
3.2 Characterization of phase noise and frequency fluctuations	14
3.2.1 Phase noise and frequency stability	14
3.2.2 Allan variance and Overlapping Allan variance	16
3.2.3 Phase noise and frequency stability measurement techniques	17
3.2.3.1 Time Interval Counter Method	17
3.2.3.2 Heterodyne Method	18
3.2.3.3 Phase Lock Loop (PLL) Method	19
3.2.4 Converting between frequency stability and phase noise	20
3.2.5 Timing jitter	21
CHAPTER 4: TECHNIQUES FOR TIME AND FREQUENCY TRANSFER OVER OPTICAL FIBRE AND A REVIEW OF EXISTING TELESCOPE DISSEMINATION SYSTEMS	
4.1 Basic approach of a round-trip phase noise compensation system	22

4.2 Microwave time and frequency dissemination of an intensity modulated optical carrier signal	23
4.3 Direct transfer of an optical carrier	25
4.4 Microwave and optical frequency transfer with a frequency comb	28
4.5 Comparative summary of existing time and frequency dissemination schemes	30

CHAPTER 5: IMPLEMENTATION OF TIME AND FREQUENCY SYSTEMS OVER OPTICAL FIBRE NETWORKS

5.1 Optical transmitters	33
5.1.1 Vertical cavity surface emitting laser (VCSEL)	33
5.1.2 Distributed feedback (DFB) laser	35
5.2 Atomic clocks	36
5.2.1 Cesium (Cs)	36
5.2.2 Rubidium (Rb)	36
5.2.3 Hydrogen (H)-Maser	37
5.3 Optical fibre signal impairments	38
5.3.1 Attenuation	38
5.3.2 Polarization mode dispersion (PMD)	39
5.3.3 Chromatic dispersion (CD)	40
5.4 Theoretical overview of optical wavelength conversion	42
5.4.1: Opto-electronic converters	43
5.4.2: Four-wave mixing (FWM) wavelength converter	44
5.4.3: Cross gain modulation (XGM) SOA wavelength converter	44
5.4.4: Cross phase modulation (XPM) SOA wavelength converter	45
5.4.5: Laser converters	46

CHAPTER 6: EXPERIMENTAL DEMONSTRATION OF A PPS-TIMING SYSTEM USED FOR OPTICAL FIBRE LATENCY MEASUREMENTS WITHIN NEXT GENERATION TELESCOPE ARRAY DATA TRANSPORT NETWORKS

6.1 Experimental design and implementation of the highly accurate PPS-timing system for optical fibre latency measurements	47
6.2 Optical fibre latency measurements	50
6.3: Summary of results	55

CHAPTER 7: PHASE STABILIZATION COMPENSATOR: DESIGN ANALYSIS AND ACTUATOR CONTROL

7.1 Variation of fibre length due to temperature fluctuations	56
7.2 Experimental and simulated demonstration of a 1550 nm VCSEL-actuator tunability range	61
7.3 Optical clock tone stability optimization	64
7.4 Summary	66

CHAPTER 8: IMPLEMENTATION OF THE PHASE STABILIZATION COMPENSATOR

8.1 Experimental demonstration of the VCSEL-actuator tunability	67
8.2 Error signal analysis in the electrical domain	68
8.2.1 Experimental demonstration of a phase error signal generated in the electrical domain	69
8.2.2 Error signal results as a function of time delay	70
8.3 Experimental error signal analysis along a 1310 nm VCSEL optical transmission link	72
8.3.1 Experimental demonstration of error signal generation used for feedback control of a 1310 nm VCSEL	72
8.3.2 Down converted error signal results	74
8.4 Towards the development of a time and frequency dissemination system using a VCSEL actuator	77

8.4.1 Experimental demonstration of a time and frequency distribution using a DFB phase error correction actuator	78
8.4.2 Experimental phase compensation results achieved by the DFB actuator	79
8.5 Summary	82

CHAPTER 9: TIME AND FREQUENCY TRANSFER ACROSS A 26 KM OPTICAL FIBRE LINK

9.1 Design and principle of operation	83
9.2 The dither-step algorithm	85
9.3 Experimental setup of the VCSEL based time and frequency dissemination scheme	89
9.4 Characterization of the 1310 nm VCSEL phase correction actuator	92
9.5 Performance evaluation of the dither control VCSEL phase correction actuator	93
9.6 Experimental Allan deviation analysis along the 26 km G.655 optical fibre transmission link	99
9.7 Summary	104

CHAPTER 10: CONCLUSION **105**

APPENDIX A: Research outputs in journals, peer reviewed conferences and books of abstracts	108
---	------------

REFERENCES	112
-------------------	------------

ABSTRACT

Significant advancements and developments have been made in optical frequency standards, in recent years. In order to verify the accuracy and preciseness of the disseminated RF signal, it is essential to compare its stability with the standards provided in literature as well as by metrology institutes. However, conventional frequency comparison techniques via satellites have extremely inferior stability qualities. As a result, the need for an alternative ultra-high precision RF transfer method presented itself. Highly accurate and precise frequency dissemination across optical fiber has proved a leading contender and a possible solution. When compared to conventional data transfer media, optical fiber has proven to be more superior and yields lower transmission errors and is immune to radio frequency interference. A further quality of optical fibre is that its transmission distance can be extended to greater degree than the traditional coaxial cable due to its low loss property.

This thesis deals with the compensation of phase noise in single mode optical fibre. Phase noise degrades the performance and stability of the RF signal as well as the optical carrier frequency across long-haul optical networks. This work begins by experimentally demonstrating a unique and novel way for measuring the round-trip optical fibre latency times. The technique is based on all optical wavelength conversion using a stable PPS injection signal. The result highlighted the importance for active phase error compensation along a fibre link. Various computer simulations were used to study the influence of temperature fluctuation on the optical fibre. The first ever error signals generated at NMU was experimentally demonstrated. Results illustrated that, by minimizing the error voltage the phase difference between the transmitted and reference signals were reduced to zero. Performance analysis testing of the VCSEL phase correction actuator showed that majority of the dither iterations that induced the phase compensation took approximately 0.15 s. Residual frequency instabilities of 3.39791×10^{-12} at 1 s and 8.14848×10^{-12} at 10^3 s was measured when the 26 km G.655 fibre link was running freely. Experimental results further showed that the relative frequency stabilities measured at 1 s and 10^3 s were 4.43902×10^{-12} and 1.62055×10^{-13} during active compensation, respectively. The novel work presented in this thesis is exciting since the VCSEL is used as the optical source as

well as the phase correction actuator. The benefits of such a device is that is reduces system costs and complexities.

CHAPTER 1

INTRODUCTION

Recent developments and improvements in technology have raised the importance and relevance of the Internet in social and economic developments. The easy accessibility and quality of broadband and Internet service have become one of the primary requirements in everyday life. The evolution and widespread use of optical fibre communication systems can be attributed to the ever-growing appeal and rapidly rising consumer and commercial demands for more bandwidth and fast Internet service. Single mode optical fibre forms the backbone of telecommunication networks and surpasses the performance of other transmission media because of its ability for providing higher data dissemination speeds and greater bandwidth.

During the initial period when optical fibre was first introduced, transmission occurred within the 1310 nm wavelength region due to the relatively low attenuation factor of approximately 0.5 dB/km. Chromatic dispersion (CD) was found to be negligible inside this transmission window. Despite these favourable fibre characteristics, attenuation still limited the transmission across long-haul optical links. The transmission window was shifted towards the 1550 nm wavelength region, exploiting the low attenuation property and subsequently satisfying long haul transmission. Before the advent of dense wavelength division multiplexing (DWDM), zero dispersion-shifted fibre (G.653) with zero CD at 1550 nm replaced conventional dispersion unshifted fibre (G.652), which is not recommended for transmission in the 1550 nm window due to the inherently large CD associated with this region. However, several CD compensating mechanisms and schemes such as dispersion compensating fibre have been proposed.

After successfully dealing with the challenges related to attenuation, CD and non-linear effects, polarization mode dispersion (PMD) an effect associated to birefringence surfaced. Further developments in optical fibre, semiconducting lasers and detectors together with the different modulation formats and DWDM technology, have increased the spectrum efficiency and transmission capacity. These advances

further minimize the signal impairments occurring along the fibre link. Improvements towards high transmission capacity have witnessed the evolution from 10 G, 100 G, 500 G and 1 T data dissemination systems. (Agrawal, 2002, p. 1-18; Idachaba, Ike & Hope, 2014, p. 438-442).

This is an incredible advancement for big data science projects such as the Square Kilometre Array (SKA). The need to transport data at enormous bit rates in astronomy related projects such as the SKA requires high-speed technologies within the telescope network. Optical fibre is an essential component of the SKA radio telescope forming the backbone of the antennae array and is needed to aggregate large volumes scientific data from individual receptors to a central processing station called the Karoo Array Processing Building (KAPB). Optical fibre is further required to distribute centrally generated clock tones to individual dishes within the antennae array. The SKA transport network is no exception to the high data rate previously mentioned. Approximately 160 Gbps of astronomical data will be transported across the optical fibre network from the individual dishes to the KAPB. The Digital Data Back Haul network can transport the 80 Tb/s of scientific data from the individual telescope elements across distances of 100km. The SKA telescope is required conduct synchronous astronomical observations with the individual antennae placed at various locations and therefore demands a number of revolutionary technological innovations, such as ultra-high timing and synchronization within telescope network (Norris, 2010, p. 21-24; SKA Organization).

The aim of this PhD project is to, for the first time at NMU, design and built an accurate frequency transfer and time synchronization system over optical fibre. The foundation of this work will hopefully pave the way for future phase noise compensation research at the NMU Centre for Broadband Communication. The work presented in this thesis is organized as follows, Chapter 2 briefly discusses the key science drivers for the SKA. The chapter further highlights the system design requirements and looks at the relevance for timing and synchronization within the telescope data network. The chapter concludes by reviewing the existing radio telescope projects. Chapter 3 introduces the theory related to stability of the phase and frequency of the disseminated RF signal. The chapter outlines concepts such as timing signals, accuracy and stability and discusses various techniques for measuring the

phase noise and fractional frequency stability. Chapter 4 reviews and discusses the various time and frequency dissemination schemes and strategies that have been proposed and demonstrated in the literature. Various components of a timing system are illustrated in Chapter 5. The high tech components such as VCSELs, DFB lasers, atomic clocks and optical effects that degrade the quality of a transmitted signal such as fibre attenuation, PMD and CD are introduced.

The bulk of the experimental results are presented and discussed from Chapter 6 to Chapter 9. Chapter 6 contains results of a novel technique used for measuring the round-trip latency time along an optical fibre link. The latency measurement approach is based on all-optical wavelength conversion. Chapter 7 outlines the design and operational aspects for the fast switching phase correction actuator. The chapter further proposes the use of a VCSEL as a phase correction actuator. Chapter 8 presents illustrative results related to the wavelength tunability property of the VCSEL and introduces the error signal measurements conducted at the Centre for Broadband Communication. The chapter concludes by presenting a proof of concept using a DFB phase correction actuator. Chapter 9 demonstrates and tests the complete dither controlled VCSEL compensation system and contains the most important results of this thesis. It includes the VCSEL actuator performance analysis data as well as the frequency stability results of the dissemination link when active compensation was implemented. The thesis concludes with a summary of the important findings of this study.

CHAPTER 2

THE SQUARE KILOMETRE ARRAY

For centuries scientists have been confronted with one of the oldest questions in science and philosophy, “Are we alone?” Advances in radio astronomy over the past ten years have brought the international scientific community to the brink of providing a comprehensive narrative of the history of the Universe. The Square Kilometre Array (SKA) is set to be the world’s largest, ultra-sensitive radio telescope capable of probing diverse areas in fundamental physics, cosmology, galaxy evolution and astrobiology. The aim of this chapter is thus to provide the reader with an overview of the SKA including its key scientific drivers. This chapter begins with a brief discussion of how the SKA project was born and its key scientific drivers. This chapter further outlines the stringent design requirements followed by a description of the SKA data transport network. Finally, the importance of timing and synchronization in telescope networks is highlighted.

2.1 The journey of the SKA and its key science projects

The SKA organization was initially formulated as an international, astronomer driven initiative under the guidance of the International Union for Radio Science (URSI) to study the next-generation radio wave observations (Dewdney, Hall, Schilizzi & Lazio, 2009, p. 1482-1496; SKA, 2017a). Since the establishment of the SKA organization, the group has grown and includes ten member countries and a further 100 organizations (SKA, 2017b). After a rigorous selection process and competitive bidding, two sites were identified for the construction of the SKA telescope. The Karoo region of South Africa will host the dish receivers and medium frequency aperture arrays while the low frequency radio wave dishes will be located in the Mid West region of Western Australia (ATNF, 2015). An important criterion considered during the site selection process was the radio frequency interference (RFI) level since the telescopes require a RFI free environment. Upon completion, the SKA telescope will be an array of coherently connected receivers reaching distances of about 3000 km with a combined collecting area of one square kilometer (1 km²) (SKA, 2011). The first scientific research study outlined for the SKA was edited by Taylor and Braun (1999). However, Carilli and Rawlings (2004, p.1482-1496)

provided an updated science case study for the SKA, identifying five key areas of interest in astronomy and cosmology.

The epoch of re-ionization (EoR), a process in which the first luminous entities in the universe are formed, sets a fundamental platform in cosmic structure development (Carilli et al., 2004, p. 1029-1038; White, Becker, Fan & Strauss, 2003, p. 1-14). The SKA will therefore facilitate important astronomical studies of the EoR in two critical fields. Firstly, the SKA will have the ability to investigate the redshifted neutral atomic hydrogen (HI) 21 cm line at meter wavelengths and consequently investigate the intergalactic medium (IGM) within the re-ionization process. Secondly, the unparalleled sensitivity provided by the SKA radio telescope will allow scientists to probe the Universe's thereby studying the formation of stars as well as radio emissions from the first accreting gigantic black holes (Carilli et al., 2004, p. 1029-1038; Carilli & Rawlings, 2004, 979–984; Grainge et al., 2017, p. 288–296; Huynh & Lazio, 2013, p. 1-13).

With the search for earth-like planets increasing, there is escalating enthusiasm in the areas of bioastronomy and astrobiology (Lazio, Tarter & Wilner, 2004, p. 985-991). By virtue of its sheer sensitivity and resolution, the SKA will play a key part in bioastronomical and astrobiological studies since it will have the distinctive ability of detecting and studying potential extra terrestrial signals and planet formation (Carilli & Rawlings, 2004, p. 979–984; Huynh & Lazio, 2013, p. 1-13; Lazio, Tarter & Wilner, 2004, p. 985-991). This superior telescope will allow astronomical observations of the inner regions of neighbouring protoplanetary disks. The SKA will further facilitate the detection of leakage radiation originating from potential extraterrestrial intelligence (ETI) transmitting devices of nearby stars. Such signals would provide direct evidence of life elsewhere in the Universe (Carilli & Rawlings, 2004, 979–984; Grainge et al., 2017, p. 288–296; Lazio, Tarter & Wilner, 2004, p. 985-991).

Another key scientific driver of the SKA is to confirm Einstein's theory of general relativity. Ultra-sensitive pulsar surveys with the SKA telescope will allow astrophysicists to probe fundamental theories in physics relating to general relativity and gravitational waves (Lorimer & McLaughlin, 2009, p. 131-136; SKA

Organization, 2011). The ability of the SKA to study pulsars may lead to the discovery of thousands of pulsars, thereby increasing the chance of detecting a pulsar in orbit around a massive black hole or a stellar body. This may result in the first experimental measurements of relativistic gravity in the ultra-strong-field limit (Carilli & Rawlings, 2004, p. 979–984; Kramer et al., 2004, p. 993-1002). With the SKA telescope acting as the timer, the pulsar–black hole system will be a remarkable study of relativistic gravitational theory (Damour & Esposito-Farese, 1998, p. 042001). Pulsars detected and timed with the SKA astronomical instrument will ultimately act as the endpoints of arms of an enormous, cosmic gravitational wave detector. With the SKA being at the core of this hypothetical astronomical device, it has the potential to detect such a galactic background at radio frequencies below the band accessible even to the laser interferometer space antenna (Kramer et al., 2004, p. 993-1002). Through its ultra-sensitive detection capabilities, broad frequency band and sky coverage, the SKA will have the ability to discover approximately 10000 to 20000 pulsars in the galaxy (Cordes et al., 2004, p. 1413–1438). Essentially, this large number incorporates all active pulsars that are radiated toward Earth including the discovery of an additional 1000 millisecond pulsars (Grainje et al., 2017, p. 288–296; Kramer et al., 2004, p. 993-1002).

Magnetism forms one of the four fundamental forces in the Universe. However, the origin of magnetic fields in astronomical objects remains unanswered in the areas of astrophysics and fundamental physics. It is nearly impossible to have a complete understanding of the Universe if magnetic fields are not entirely understood. The evolution of magnetic fields as galaxies evolve remains unanswered and the process of how magnetic fields are generated and maintained needs to be addressed (Gaensler, Beck & Feretti, 2004, p. 1003–1012). The SKA’s high polarimetric and spectropolarimetric attributes are the main contributors towards studying magnetic field in the distant Universe (Beck & Gaensler, 2004, p. 1289–1304). With the existing radio astronomy telescope, the only technique available for obtaining simultaneous and accurate values for intrinsic polarization position angle and Faraday rotation measures is to conduct numerous astronomical observations across a wide frequency range. However, this is a time consuming process and caution should be taken whilst analyzing data, since depolarizing effects are frequency dependent (Gaensler, Beck & Feretti, 2004, p. 1003–1012; Sokoloff et al., 1998, p. 189–206).

The superior sensitivity and wide frequency bandwidth offered by the SKA instrument will eradicate these measurement difficulties and revolutionize the study of cosmic magnetism.

Neutral atomic hydrogen (HI) is the most abundant and fundamental baryonic element of the Universe (Schilizzi, Dewdney & Lazio, 2008, p. 70121I-1- 70121I-13). The primary motivation for constructing the SKA telescope was to detect HI in the galaxy at high redshift. Furthermore, it will be the only way of experimentally investigating the cosmic evolution of neutral HI. The results produced from this study, together with data on star formation from the radio continuum, are required to better understand how stars are formed. With the ability to map out where the HI elements are located within the galaxy over a greater cosmic time period, the SKA antenna array is anticipated to be the ultimate HI imaging device. Using the SKA instrument, scientists will be able to measure the dark matter power spectrum using weak gravitational lensing (Carilli & Rawlings, 2004, p. 979–984; Grainge et al., 2017, p. 288–296).

The galactic entities that existed before the birth of galaxies and stars and the re-ionization cosmic matter can only be studied and observed using radio waves. Mapping large sections of the Universe with the SKA will provide conclusive testing of the existing cosmological models (Grainge et al., 2017, p. 288–296).

2.2 System design requirements

The SKA will be an aperture array radio telescope that adopts existing radio imaging ideas. The technical design requirements for the SKA telescope have been driven by the key science objectives proposed by the astronomy community however, it may be constrained and restricted by additional factors such as cost and feasibility. The approach implemented by the SKA is to use the five key science cases as a design reference (Dewdney et al., 2009, p. 1482-1496).

The proposed scientific objectives require the SKA radio astronomy telescope to operate within the 1 cm to 4.3 m wavelength band. This enables a wide range of astronomical science to be conducted from the low (70 MHz) to high (30 GHz) frequency band. This requirement cannot be realized with the use of a single antenna

technology, therefore a dish array with an effective collecting surface of one million square metres across the broad frequency or wavelength range is needed (Dewdney et al., 2009, p. 1482-1496; Hall, Schilizzi, Dewdney & Lazio, 2008, p. 4-19; Schilizzi et al., 2007, p. 50-55).

The starting sensitivity required for early universal HI particle imaging and detection can only be realized by deploying a very large collecting area radio telescope such as the SKA. For the SKA to meet the science objective it needs a starting sensitivity of $10^4 \text{ m}^2/\text{K}$ at frequencies in the region of 1.4 GHz. Upon completion, the SKA will have 50 times the starting sensitivity of existing telescopes (Dewdney et al., 2009, p. 1482-1496; Hall et al., 2008, p. 4-19). The high sensitivity specification together with a large field of view, enables the SKA telescope to have a fast surveying speed across the entire sky. At wavelengths beyond 20 cm, the SKA must have a surveying speed of at least $3 \times 10^9 \text{ deg}^2 \text{ m}^4/\text{K}^2$ (Dewdney et al., 2009, p. 1482-1496; Turner, 2014, p. 27-32). For optimal astronomical science to be conducted with the SKA the effective collection area of the telescope must be concentrated within a centralized space. It is proposed that 50% of the collecting area be situated within a radius of 2.5 km of the centre of the antennae array. Furthermore, 25% of the antennae collection surface must be located within 180 km of the centre. It is expected that the remaining 25% of the telescope be built out to the maximum extent of the array (Dewdney et al., 2009, p. 1482-1496; Hall et al., 2008, p. 4-19; Schilizzi et al., 2007, p. 65). Additional technical performance requirements for the SKA can be found in Dewdney et al. (2009, p. 1482-1496) and Hall et al. (Hall et al., 2008, p. 4-19).

2.3 SKA optical fibre transport network

The SKA data transport network is divided into three distinct sub networks for both the African and Australian telescopes. Optical fibre forms the backbone of the SKA and is required to aggregate large amounts of scientific data from individual dishes to a central processing facility. It is estimated that each dish within SKA-mid will generate approximately 90 Gbps of astronomical data. This suggests that data will be transmitted across optical fibre from the geographically dispersed dishes to the central computing facility at a total transmission rate of 17.7 Tbps (Grainge et al., 2017, p. 288–296). In addition to the transfer of monitoring and control signals, optical fibre will be used to disseminate centrally generated clock tone to individual dishes within

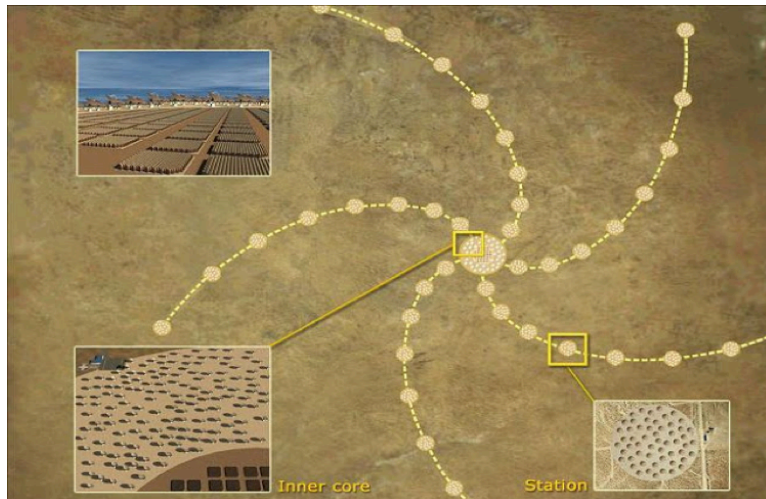


Figure 2.1: Proposed SKA telescope layout.

the antennae array (Gibbon et al., 2015, p. 028001). The proposed layout for the SKA telescope is illustratively shown in Figure 2.1.

The astronomical data transport network is split into three sub network systems, each having its own technical requirements. The primary function of the digital data back haul (DDBH) network is to aggregate the astronomical signals from each antenna to the central signal processing (CSP) facility, and will consist of commercial, off-the-shelf-technology. This network will also be adopted within the SKA1 low, SKA1 mid and SKA1 survey arrays. The SKA mid telescope array will have two distinct DDBH transport network configurations depending on the optical fibre span between the antenna and the central processing unit. Approximately 95 of the inner array dishes will be located less than 10 km from the CSP facility, while the remaining 38 outer receivers will be found at distances greater than 10 km from the CSP. The 38 outer array antennae will be using long reach DWDM transmission technology. The DDBH network within the SKA1 low antennae array needs to cater for 40 Gb Ethernet data transmission from each dish outside the core area (Grainge et al., 2017, p. 288–296; Schilizzi, 2013, p. 17-18).

Once the astronomical data has been processed at the CSP, it must then be transferred to the science data processor (SDP) unit. The main role of the SKA CSP–SDP data transport network is to support long haul transmission at high bandwidth between the CSP and the SDP. Likewise, this network will facilitate the transfer of non-scientific

data such as monitoring and control signals from the telescope manager (TM). By virtue of the extreme transmission rates and distances, the CSP–SDP data transport network will require long haul and advanced modulation technology. In Australia, a total transmission rate of 18.5 Tbps has to be transmitted across 820 km of fibre from Murchison Radio-astronomy Observatory to Geraldton and then to Perth. While in South Africa, a total data rate of 8 Tbps has to be disseminated across 915 km of optical fibre from the Karoo to Cape Town (Grainge et al., 2017, p. 288–296; Schilizzi, 2013, p. 21-22).

The Non-Science Data Network (NSDN) is primarily responsible for transmitting monitoring and control signals from the TM and the Local Monitoring and Control (LMC) interchanges to all the sub systems within the SKA antennae array. The NSDN is designed to provide operational and security support to the SKA telescope. The NSDN will either integrate or transition to the existing precursor data transport infrastructure in order to guarantee an all-inclusive network approach (Grainge et al., 2017, p. 288–296; Schilizzi, 2013, p. 34-35).

2.4 Synchronization and timing for the SKA

Synchronization and timing within the SKA telescope array networks is required to meet a number of essential requirements. A robust central reference clock system consisting of a single or an ensemble of hydrogen masers is crucial in achieving synchronization. The distribution of the stable and accurate clock signals over fibre to the dishes ensures the entire synthesis array is phase coherent. The proposed timing system cannot be commercial procured. In this regard, the establishment of a fibre based time and frequency synchronization system was required. During an astronomical measurement, the telescope array is permitted to have a maximum coherence loss of 2%, corresponding to a root mean square (RMS) phase error of 11° . At a maximum observational frequency of 20 GHz, this translates to accuracies of approximately 1.5 ps (Garrington et al., 2011, p. 25; Gibbon et al., 2015, p. 028001; Grainge et al., 2017, p. 288–296). The hydrogen maser further provides high precision timing for astrophysical occurrences such as transient and pulsar detection. Typically, 1 ns to 10 ns timing accuracies over a 10 year period is required for pulsar detection. Clock tones are further required to deliver accurate and precise frequency standards to

the local oscillators (LOs) and digitizers located at every dish within the synthesis array. Furthermore, it is also required for time stamping the incoming astronomical data. In addition, clocks are also used to derive absolute time for system management, beam steering and antenna pointing (Garrington et al., 2011, p. 25; Gibbon et al., 2015, p. 028001; Grainge et al., 2017, p. 288–296).

The precise and accurate reference signals will be disseminated across optical fibre to each of the telescopes during a scientific observation. External environmental conditions such as temperature fluctuation, together with mechanical and acoustic perturbations, may cause variations of the optical path length, thereby degrading the stability of the disseminated reference signals along the fibre. However, some of the optical fibre will be buried at a suitable depth with appropriate shielding from temperature and environmental perturbations. Nonetheless, the phase stability of the optical signal could remain susceptible to inherent polarization fluctuations along the fibre. To negate these effects, an optical fibre link stabilization system is needed in order to ensure that a stable and synchronized signal is disseminated to the remote sites with a frequency stability that exceeds the specified SKA requirements (Grainge et al., 2017, p. 288–296).

2.5 Review of existing synchronization and timing techniques

Current synchronization and timing techniques across optical fibre for telescope arrays include the Atacama large millimeter/submillimeter array (ALMA) in Chile along with the multi element radio linked interferometer network (eMERLIN) telescope in the United Kingdom. For eMERLIN telescope array, an RMS stability of 1 ps over 1 s, 2 ps over 1 min, and 4 ps over 10 min has been experimentally demonstrated for a 1.4863 GHz clock signal across 110.8 km deployed optical fibre (Gibbon et al., 2015, p. 028001; McCool, Bentley, Argo, Spencer, & Garrington, 2008, p. 1-2). ALMA however, depends on sub picosecond stability for frequencies up to 950 GHz distributed across long baseline lengths of up to 15 km (Gibbon et al., 2015, p. 028001; Shillue et al., 2011, p. 1-4). Both eMERLIN and ALMA employs highly accurate oscillators and phase locked loop technology at the individual receivers. Furthermore, both these astronomy instruments adopt round-trip phase correction strategies. In ALMA, phase monitoring and correction is realized by using a voltage-actuated piezoelectric fibre stretcher. In the eMERLIN telescope array

network, the round-trip phase error correction is applied through delay compensation by the correlator (Gibbon et al., 2015, p. 028001; Shillue et al., 2011, p. 1-4).

In summary, this chapter provides a brief overview of the SKA where the key scientific cases were summarized before discussing telescope technical requirements. Furthermore, a concise discussion of the relevance and requirements for synchronization and timing signals within the SKA telescope arrays was given. The chapter concluded with a review of the existing telescope networks synchronization and timing techniques. In the following chapter a detailed theoretical description of phase noise and frequency stability is provided together with the related characterization and measurement techniques.

CHAPTER 3

PHASE STABILITY AND FREQUENCY FLUCTUATIONS

The previous chapter provided a brief summary of the SKA, outlining the system requirements for signal and data transport. One of the most complex and technically challenging requirements of such an interferometric radio astronomy instruments is to coherently combine the astronomical signals collected by the individual receptors with the antenna array. This chapter begins by outlining concepts such as timing signals, accuracy and stability. Furthermore, this chapter touches on phase noise and frequency stability and the related characterization and measurement techniques.

3.1 Timing signals, accuracy and stability

An ideal sine wave oscillator produces a voltage signal that changes with time and is expressed as:

$$V(t) = A \cos[\omega_0 t + \varphi] \quad (3.1)$$

where A is the amplitude, ω_0 the angular frequency and φ represents a fixed phase constant. However, in a real oscillator the actual clock signal fluctuates in phase and amplitude, where the output is described as:

$$V(t) = A[1 + \alpha(t)] \cos[\omega_0 t + \varphi(t)] \quad (3.2)$$

where $\alpha(t)$ and $\varphi(t)$ represents the random amplitude and phase fluctuations (Bregni, 1997, p. 1284-1294; Howe, 2005, p. 1706-1720; Rubiola, 2009, p. 1-3).

The performance of an oscillator is described by its accuracy and stability characteristic (ISO, 2012). The accuracy of a clock is associated with the difference between the offset and an ideal value and can be defined in both the time and frequency domain. The time offset is defined as the difference between the measured and ideal rise times of an output pulse. The ideal rise time corresponds to the Coordinated Universal Time (UTC). Furthermore, the frequency offset is expressed as the difference between the measured and nominal frequency with zero uncertainty. In addition, stability of a clock specifies how well an oscillator can generate the exact time or frequency offset over a given period. The stability is usually given as a statistical approximation of the time and frequency instabilities of a clock signal. The

difference between accuracy and stability is illustratively shown in Figure 3.1 (Lombardi, 2002; Marra, 2013, p. 11; Moreira, 2014, p. 81-83).

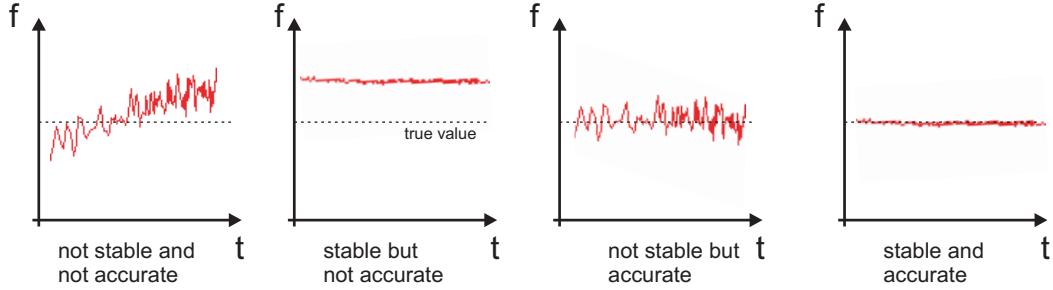


Figure 3.1: Relationship between accuracy and stability (Marra, 2013, p. 11).

3.2 Characterization of phase noise and frequency fluctuations

Information regarding the stability properties of the oscillator/link combination is extremely important as it is required within frequency dissemination and synchronization systems in which phase noise compensation is needed. It is therefore crucial to monitor and measure the fluctuations of the amplitude and phase of the clock signal over a period of time. Phase fluctuations or frequency stability measurements are performed in the time domain, whereas phase noise characterization is done in the frequency domain.

3.2.1 Phase noise and frequency stability

Phase noise is the phrase used to quantify the instability of a clock signal in the frequency domain and is caused by infinitesimally small random fluctuations or uncertainties in its phase (Dickstein, 2012). Phase noise measurements are best expressed as a power spectral density (PSD) distribution of the time domain phase fluctuations, $\varphi(t)$, given in Equation 3.2 (Marra, 2013, p. 14). Moreover, the phase noise, $L(f)$, measurement characterizes short-term instabilities of a timing signal in terms of the one-sided power spectral density of phase fluctuations, $S_{\varphi}(f)$ and is mathematically described as (Abidi & Meyer, 1983, p. 794-802; Baran & Kasal, 2009, p. 1-4; Riley, 2008, p. 5-20):

$$L(f) = 10 \cdot \log\left(\frac{1}{2} S_{\varphi}(f)\right) \quad (3.3)$$

Alternatively, the phase noise can be mathematical defined in terms of fractional frequency $y(t)$ as a one sided spectral density of the frequency fluctuations, $S_y(f)$ as (Baran & Kasal, 2009, p. 1-4, Hajimiri & Lee, 1998, p. 179-194; Howe, Allan & Barnes, 1981, p. 1-47, Razavi, 1996, p. 331–343):

$$S_y(f) = \left(\frac{f}{f_0}\right)^2 S_{\varphi, f} \quad (3.4)$$

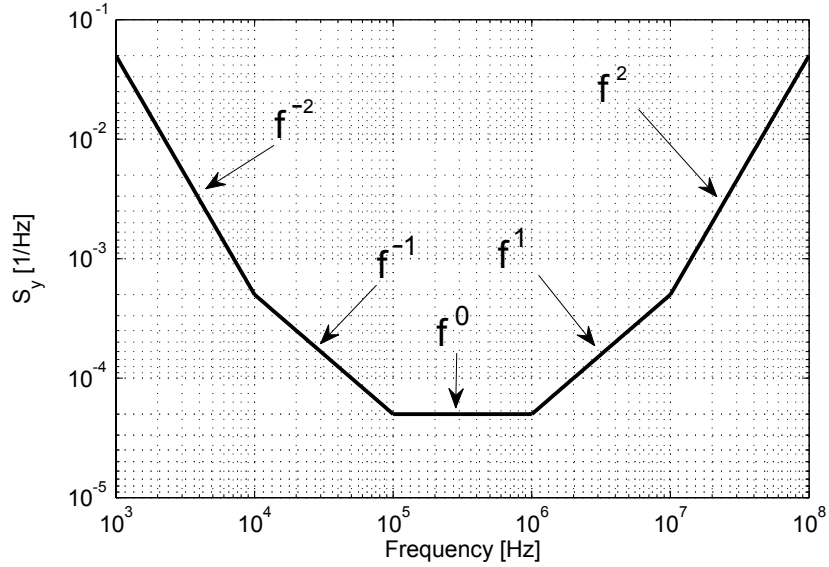


Figure 3.2: Power law spectral density distribution (Moreira, 2014, p. 88).

Figure 3.2 provides an illustrative summary of the fractional frequency spectral density distribution of the basic noise types. In Figure 3.2 f^2 , f^1 , f^0 , f^1 and f^2 refers to Random Walk Frequency Modulation (RWF), Flicker Frequency Modulation (FPM), White Frequency Modulation (WFM), Flicker Phase Modulation (FPM) and White Phase Modulation, respectively. The power spectral density distribution illustrated in Figure 3.2 can be used to characterize the various oscillator noise contributions (Moreira, 2014, p. 88).

Consider a sinusoidal timing signal with a specific frequency, it is possible to measure Δt and ΔV . The frequency associated with infinitesimally small Δt is referred to as the instantaneous frequency. The instantaneous frequency is better approximated when the Δt interval is small. However, in a realistic sense it is not possible to characterize

the instantaneous frequency due to finite bandwidths (Howe, 2005, p. 1706-1720). Consider an oscillator generating a clock signal which operates at a nominal frequency, f_0 . The frequency stability is a term used to measure the frequency fluctuations of the timing signal generated by the oscillator and is generally used when comparing the stability of one clock relative to another. Furthermore, frequency stability is best defined as the degree to which an oscillator produces a clock signal at the same frequency for any interval Δt throughout a specified time period (Baghdady, Lincoln & Nelin, 1965, p. 704–722; Howe, 2005, p. 1706-1720; Petrov & Davydov, 2015, p. 739-744). The frequency stability of an oscillator is often expressed as a fraction where the absolute frequency fluctuations are divided by the nominal frequency (Marra, 2013, p. 13). Figure 3.3 shows a typical stability versus time plot of a frequency stability measurement over a specific time period (Marra, 2013, p. 14).

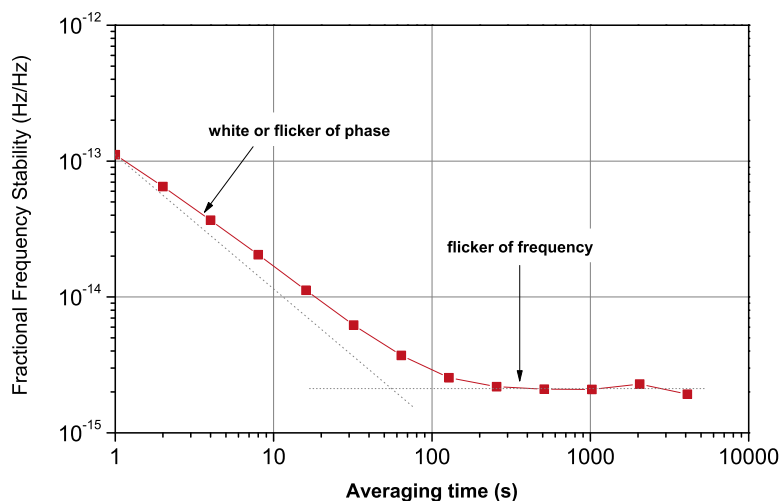


Figure 3.3: Classic frequency stability plot (Marra, 2013, p. 14).

3.2.2 Allan variance and Overlapping Allan variance

The Allan variance was primarily developed to measure the RMS frequency fluctuations of two oscillators as a function of time, and is regarded as the most common technique for characterizing the frequency stability in the time domain. The Allan variance is a non-overlapping or a two-sample variance formed by the average of the squared differences between successive fractional frequency fluctuation values of a regularly measured quantity taken over a specific sampling time period. The

Allan variance is mathematically defined as (Allan, 1987, p. 646-654; Levine, 1999, p. 2567-2596; Riley, 2008, p. 14):

$$\sigma_y^2(\tau) = \frac{1}{2(M-1)} \sum_{i=1}^{M-1} [y_{i+1} + y_i]^2 \quad (3.5)$$

where y_i is the i^{th} fractional frequency average over a sampling interval τ . M is the fractional frequency values within the sample set (Allan, 1966, p. 221-230).

Another version of the Allan variance, referred to as the overlapping Allan variance or AVAR, is given in Equation 3.6. This approach makes maximum use of the entire data set by forming all possible overlapping samples at each averaging time τ . The overlapping Allan variance can be calculated from a set of M fractional frequency values for averaging time $\tau = n\tau_0$, where, n and τ_0 are defined as the averaging factor and the basic measurement time interval, respectively (Barnes et al., 1971, p. 105-120; Riley, 2008, p. 17; Rutman, 1978, p. 1048-1075).

$$\sigma_y^2 = \frac{1}{2m^2(M-2m+1)} \sum_{j=1}^{M-2m+1} \left\{ \sum_{i=j}^{j+m-1} [y_{i+m} + y_i] \right\}^2 \quad (3.6)$$

3.2.3 Phase noise and frequency stability measurement techniques

Measuring the stability or noise allows one to predict the performance of an oscillator, either in the frequency or time domain. The most common instruments used to assess the performance of a signal generator are digital electronic counters and spectrum analyzers. The performance of a measuring system is dependent on the stability of its reference source (Barnes et al., 1971, p. 105-120; Riley, 2008, p. 80). Many of the measurement techniques used are founded on some form of heterodyne system however, the simplest approach for quantifying clock stability is to measure the time difference between them. In this section, a concise and practical attempt is made to present several methods for measuring the phase and frequency fluctuations of a timing signal.

3.2.3.1 Time Interval Counter Method

In the time interval counter method, the operational frequencies of the two sources being compared are down converted to a lower frequency. In this approach, the

relative time differences between two oscillators are measured with a high-resolution time interval counter as shown in Figure 3.4 (Riley, 2008, p. 80). In doing so, the relative stability of the two signals used can be measured. Traditional time interval counters have two input channels where one signal starts the counter while the second signal stops the measurement process. The time interval between the clock signals is measured by counting the number of cycles from the time base oscillator (Lombardi, 2002, p. 171-181).

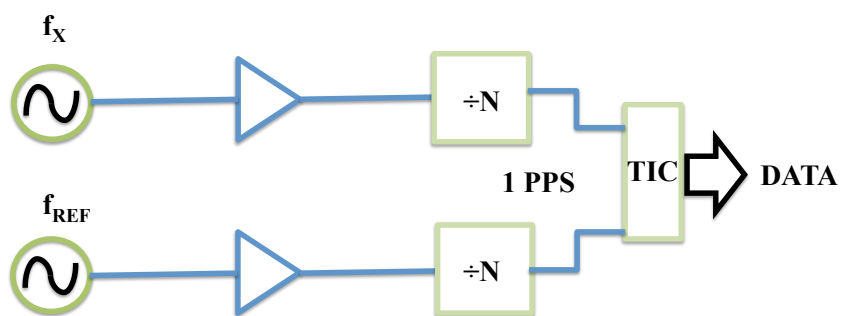


Figure 3.4: Schematic of a time interval counter method.

This method is limited in signal-to-noise ratio due of the wide bandwidth required to measure the fast rise time of the signal.

3.2.3.2 Heterodyne Method

One of the common methods used for measuring small fluctuations is the heterodyne or beat frequency measurement technique, shown in Figure 3.5. As illustrated, a frequency generated from the oscillator under test is down converted to a value that can be measured by the period counter.

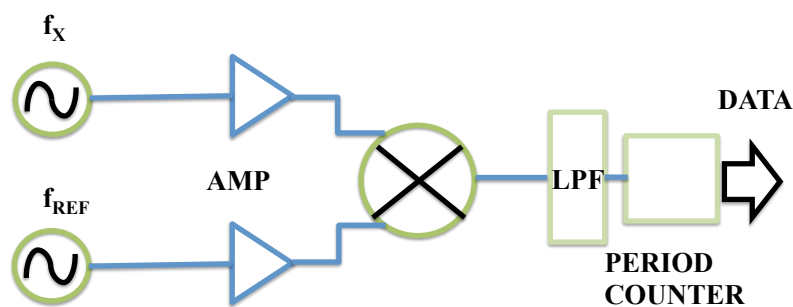


Figure 3.5: Heterodyne block diagram.

The down conversion is achieved by frequency mixing the oscillator signal with an appropriate reference signal. The resultant mixing product passes through a low pass filter (LPF) allowing the resulting output, called the difference or beat frequency (f_b) to be detected by the counter (Vanier & Tétu, 1978, p. 247-291). Any frequency harmonics following the mixer is suppressed by the LPF. The fractional frequency is then evaluated by dividing the beat frequency f_b by the nominal carrier frequency f_0 (Howe, 2005, p. 1706-1720).

3.2.3.3 Phase Lock Loop (PLL) Method

The schematic of the phase lock loop (PLL), which most commercial frequency stability and phase noise measurement systems are based, is shown in Figure 3.6.

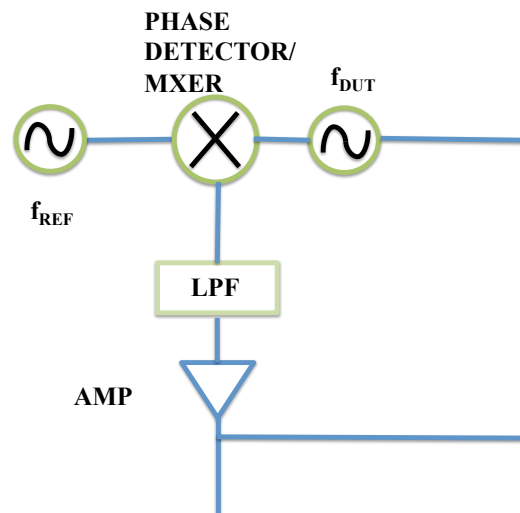


Figure 3.6: Phase lock loop (PLL) block diagram.

A sine wave from the oscillator under test is directed into the radio frequency (RF) port of a frequency mixer whilst a reference signal, 90 degrees out of phase, is coupled into the local oscillator (LO) port. Since the two signals are in quadrature, the output of the mixer has a nominal average voltage of zero. The frequency mixer converts the phase differences, $\Delta\phi$, between the two sine waves into a voltage before returning the resultant error signal to the input port of the oscillator under test. As a result the reference oscillator is said to be phase locked to the signal generator under test (Gardner, 1979, p. 8-21; Howe, 2005, p. 1706-1720; Rubiola, 2009, p. 31-32).

3.2.4 Converting between frequency stability and phase noise

The spectra of most noise processes can be mathematically modelled by a power law function, as illustrated in Figure 3.7. Conversion between the time and frequency domain is made possible by estimations based on the power law spectral model for the noise processes or by numerical integration of the fundamental relationship between phase noise and frequency stability (Riley, 2008, p. 73). The diagram illustratively represents the relationship between phase noise and frequency stability. Dawkins, Mcferran & Luiten (2007, p. 918-925) and Sullivan, Allan, Howe & Walls (1990, p. TN-164) showed that it is possible to calculate the Allan variance from the corresponding phase noise power spectral density spectrum. However, is not always possible to calculate the phase noise from the associated Allan variance data, since both the white and flicker phase noise are dependent on the observation time τ . Generally, the conversion from $\sigma_y^2(\tau)$ to $S_y(f)$ is not error free (Greenhall, 1998, p. 623-627). Nonetheless, the power law model is still valid and the conversion from phase noise is possible (Marra, 2013, p.16).

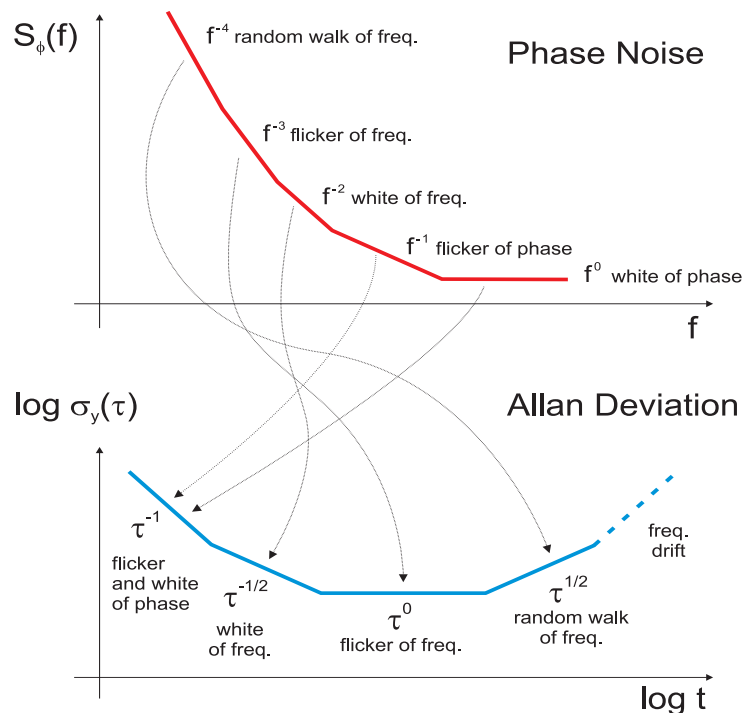


Figure 3.7: Relationship between phase noise and frequency stability (Marra, 2013, p. 17).

3.2.5 Timing jitter

Timing signals are needed as it ensures a coherent and synchronized transfer of data between two locations. Ideally, timing signal has static oscillation periods and duty cycles that never fluctuate over time. However, a real timing signal has small variations in phase, frequency, period and duty cycle (IDT, 2014, p. 1-17). These variations are referred to as jitter and is mathematically expressed as:

$$T_{rms} = \frac{1}{2\pi f_0} \sqrt{\int_{f_l}^{f_h} S_{\phi}(f) df} \quad (3.7)$$

where f_l and f_h are the lower and upper bandwidth limits, respectively. S_{ϕ} and f_0 is the double sided phase noise and nominal frequency, respectively (Marra, 2013, p. 20). It is often preferred to express the phase fluctuations of an oscillator as an averaged timing jitter rather than a power spectral density distribution.

This chapter discussed various qualities of the disseminated signal such as accuracy and stability. The different techniques for measuring the phase noise and frequency stability were also highlighted. The following chapter reviews the various techniques for time and frequency transfer across fibre networks. Furthermore, a brief description of the existing telescope dissemination systems is given.

CHAPTER 4

TECHNIQUES FOR TIME AND FREQUENCY TRANSFER OVER OPTICAL FIBRE AND A REVIEW OF EXISTING TELESCOPE DISSEMINATION SYSTEMS

Recent advancements and developments made in optical frequency standards promoted research activities on the dissemination of ultra-stable time and frequency signals across fibre links. This chapter features numerous frequency transfer and time synchronization strategies via optical fibre, which have been proposed and demonstrated in the literature. The techniques described in this chapter are based on three fundamental design strategies that have been recently studied:

- microwave transfer by intensity modulation of an optical carrier;
- direct transfer of an optical carrier; and
- microwave and optical frequency transfer with a frequency comb.

The frequency reference dissemination and synchronization schemes described in this chapter employ a round-trip principle to suppress the environmentally induced fibre phase noise (Marra, 2013, p. 29).

4.1 Basic approach of a round-trip phase noise compensation system

The rationale behind a fibre induced phase noise compensation method is to measure the round-trip phase fluctuations along the dissemination link at the transmission location, followed by the subtraction of the phase noise of the disseminated signal at the transmission site. As a result, the phase noise within the feedback loop can be compensated (Wang et al., 2012a, p. 1-4).

In this approach, an ultra-stable signal with an initial phase $\phi_i(t)$ propagates along an optical fibre from the transmitting site to the receiver at the end. The phase stability of the transmitted signal remains susceptible to polarization fluctuations along the fibre link. By means of an optical circulator or reflector, part of the signal is returned to the transmitting location where the phase, $2\phi_i(t)$, is compared to that of the original signal before being injected into the fibre. Depending on the actuator and correction strategy

employed, a $-2\phi(t)$ phase correction is applied to the disseminated signal in order to suppress the noise at the transmission site (Marra, 2013, p. 29).

4.2 Microwave time and frequency dissemination of an intensity modulated optical carrier signal

For microwave time and frequency transfer systems, the basic idea is to disseminate a stable amplitude modulated microwave signal emitted by a free running laser from the transmission end to the remote site. Modulation can be enforced by either using an external amplitude modulator such as a Mach-Zender Modulator (MZM) or by employing directly modulated laser sources (see Chapter 5). A photodiode located at the receiver end can be used to recover the intensity modulated microwave signal.

Daussy et al., (2005, p. 203904-1-203904-4) demonstrated a microwave frequency transfer along a 86 km round-trip optical fibre link in which a two stage correction system was employed. The first stage of the compensation scheme corrects for any fibre induced perturbations on the transferred RF reference signal from the transmission site (SYRTE) to the remote site (LPL). Here, compensation is achieved by detecting the phase error value before applying an equivalent correction along the one-way transmission path. This is done by shifting the phase of a 100 MHz signal in the opposite direction in order to get a 100 MHz signal at the receiver end (Daussy et al., 2005, p. 203904-1-203904-4).

The second compensation mechanism applied at the remote site acts directly on the optical fibre transmission link. Phase correction is realized by comparing the phase of the transmitted 100 MHz and the modulated 100 MHz after a single round-trip in the second fibre. At the input of the second fibre, a mechanical stress is applied to a 15 m optical fibre wrapped around a cylindrical piezoelectric actuator. This process corrects for all fast phase fluctuation occurring along the fibre while heating a 1 km optical fibre spool compensates for slow phase variations. Stabilities of 8×10^{-15} at 1 s and 10^{-17} for one day were reported (Daussy et al., 2005, p. 203904-1-203904-4).

In another interesting microwave frequency dissemination system across a 80 km urban telecommunication fibre network, Wang et al., (2012a, p. 1-4) reported on

stabilities of $7 \times 10^{-15} / 1 \text{ s}$ and $4.5 \times 10^{-19} / 10^5 \text{ s}$. In this scheme, a voltage controlled crystal oscillator (VCXO) is used to compensate for the phase noise incurred during transmission (Wang et al., 2012a, p. 1-4). The VCXO is further used to modulate the intensity of a 1547 nm, single mode laser source. In addition to the VCXO, this scheme used three more microwave signal generators phase locked to a cesium atomic clock. Together with a series of frequency mixing operations, the additional microwave signal generators are used to generate a DC error feedback signal to control the phase of VCXO. Another interesting feature demonstrated by Wang et al., (2012a, p. 1-4) is the transfer of stable timing signals between the local and remote sites using a time delay compensation technique. In the experiment, a timing signal generated by a synthesized clock generator is used to intensity modulate a 1547 nm single mode laser. After the completion of a single round-trip, a time interval counter was used to measure the accumulated time delay along the two-way fibre path. Using an iterative computer algorithm, together with a controlled delay unit, a time delay correction was applied. Transmission delay stabilities within 50 ps were demonstrated (Wang et al., 2012a, p. 1-4). A similar approach was demonstrated and reported by Wang et al., (2012b, p. 1-5).

Furthermore, Ye et al., (2003, p. 1459-1467) developed a stabilized optical fibre dissemination system for the distribution of microwave signals. In this experiment a 30 mW DFB laser carrier was intensity modulated with the RF frequencies up to 12 GHz and transferred to the end user site via optical fibre. Subsequently, the transmitted signal was returned to the local site, thereby completing the round-trip. An error signal was generated in order to regulate the fibre induced group delay and phase noise along the transmission link. The compensation was achieved with the use of a temperature-compensated fibre reel. Stability in the order of 10^{-14} at 1 second was reported along a 16 km buried fibre link (Ye et al., 2003, p. 1459-1467).

Lopez et al., (2008, p. 35-41) developed an ultra-stable microwave dissemination system across an 86 km urban fibre network in which a fractional frequency stability of $5 \times 10^{-15}/\text{s}$ and $2 \times 10^{-18}/\text{one day}$ integration times were reported (Lopez et al., 2008, p. 35-41). This work uses a 1 GHz microwave frequency to modulate a 1550 nm directly modulated DFB laser. After the optical waveform is transmitted along the fibre and detected at the remote end, the resultant electrical signal was used for

frequency synthesis. The 900 MHz synthesized coherent RF signal was then used to modulate a second DFB laser located at the remote end which transmits a signal back towards the local end. At the remote end, a frequency mixing operation was established in order to generate an error signal for feedback control of two optical delay lines. A propagation delay fluctuation of 1 ps over a few days was recorded when the compensation system was activated (Lopez et al., 2008, p. 35-41).

The fibre phase noise accumulated during the transmission was actively cancelled by developing a compensation system using a dual mixing technique with a voltage-controlled crystal oscillator (Fujieda, Kumagai, Gotoh & Hosokawa, 2009, p. 1223-1228). A 100 MHz signal generated by a VCXO was frequency multiplied and up-converted to a 1 GHz microwave signal where it was used to modulate the amplitude of a 1550 nm DFB laser. The intensity modulated optical signal was transmitted along single mode fibre from the local to the remote location. Once received at the remote site, the optical signal was amplified using an erbium doped fibre amplifier (EDFA), where parts of the microwave signal were used to intensity modulate the laser. The optical signal is transmitted back to the local site through the same optical fibre. The active phase noise compensation was realized by using a two-stage frequency mixing process. The sum of two independently generated error signals was used to tune the VCXO. By applying the active compensation system, a frequency stability of 1×10^{-17} was measured for an averaging time of 60 000 s (Fujieda, Kumagai, Gotoh & Hosokawa, 2009, p. 1223-1228).

4.3 Direct transfer of an optical carrier

This dissemination technique uses a single optical carrier directly transferred from the locate site to a user situated at a remote location. In frequency dissemination experiments adopting this approach, acousto-optic modulators are placed at the transmission site of the fibre link. As a result, environmentally induced phase fluctuations of the transmitted optical carrier will be corrected in real time. The contrasting feature of this technique, in relation to other methods, is that there is no phase stabilization along the optical transmission link. The Doppler induced frequency shift experienced by the optical carrier signal is eliminated whilst the optical path length changes over time (Marra, 2013, p. 32).

Jiang et al., (2008, p. 2029-2035) transferred the frequency of an ultra-stable laser across 86 km of urban optical fibre and reported frequency stabilities of 1.5×10^{-16} at 1 s and 10^{-19} at 500 s over the transmission link. Since the signal emitted by the cavity stabilized fibre laser was required for phase noise measurements and compensation and also for frequency dissemination, an optical coupler was used to split the ultra-stable laser light into two parts. As seen in the experimental procedure (Jiang et al., 2008, p. 2029-2035), the first optical path facilitates the fibre stability measurement and phase noise compensation, while the second arm is connected to the transmission link. This dissemination scheme features two acousto-optic modulators (AOM). AOM1 was located at the local site with frequency $f_1 \approx 40$ MHz, while AOM2 was placed at the remote end with frequency $f_2 \approx 70$ MHz (Jiang et al., 2008, p. 2029-2035). Both AOM's provide distinct frequency shifts as per the desired requirements. By using a series of optical circulators, the disseminated signal was returned to the local site. Compensation was achieved by phase locking the beat note at $2f_1+f_2$ to a stable frequency synthesizer using AOM1. Furthermore, a phase lock loop (PLL) was integrated into the system in order to apply the necessary correction, $\theta_c = -\theta_p$ to the frequency of AOM1. Consequently, the fibre-induced phase noise at the remote end of the optical link is actively cancelled. Polarization controllers were used for optimizing the beat-note signal amplitudes (Jiang et al., 2008, p. 2029-2035).

Schediwy et al., (2013, p. 2893-2896) demonstrated a technique for the simultaneous distribution of accurate frequency signals to several remote locations on a branching optical fibre network. The technique corrects for variation in the optical fibre length at the output of the transmission link rather than at the input, as in conventional dissemination methods. In their approach, an optical frequency is distributed from the signal source along a fibre link to a remote location. At the receiver site the optical signal passes through an AOM that applies a frequency shift onto the laser light. Part of the frequency shifted optical signal is returned back to the source end using a Faraday mirror. Before arriving at the transmission end a second shift is applied as the signal passes a second time through the AOM. A second Faraday mirror stationed at the source end is used to reflect the signal back to the remote end. The signal now experiences a third frequency shift as it propagates a third time along the optical fibre. The photodiode placed at the remote site detects the mixing product between signals

which experienced the first and third frequency shift along the transmission link (Schediwy et al., 2013, p. 2893-2896). Thereafter the resultant output was bandpass filtered at a central frequency twice the frequency imparted by the AOM. After lowpass filtering, an error signal was produced in order to modulate the frequency of its AOM drive signal. As a result, the servo loop is closed thereby stabilizing the optical length of the transmission link. With the stabilization system engaged, frequency stabilities of 1.1×10^{-17} at 1 s and 6.2×10^{-18} at 1 s were measured for remote sites A and B, respectively (Schediwy et al., 2013, p. 2893-2896).

A long-distance ultra-stable optical frequency dissemination technique across 146 km underground fibre between Braunschweig and Hanover was demonstrated (Grosche et al., 2009, p. 2270-2272). The interferometric compensation system is made up of two 73 km concatenated fibre links. Grosche et al., (2009, p. 2270-2272) treated the entire optical transmission link as one arm of a Michelson interferometer, which is phase-stabilized to a reference arm. By means of a round-trip transmission scheme, an error correction signal was generated in order to control the phase and frequency of an AOM located at the local site. A second AOM placed at the remote site was used to differentiate between the signals reflected by the Faraday mirror and spurious reflections along the fibre. The optical source is made up of a 1542 nm fibre laser phase locked to a 657 nm cavity stabilized optical clock laser. The clock laser forms part of a cesium neutral atom frequency standard located at Braunschweig. Using an active stabilization system, a fractional stability of 3×10^{-15} at 1 s was reported (Grosche et al., 2009, p. 2270-2272).

Fujieda et al., (2011, p. 16498-16507) demonstrated an all-optical dissemination system with frequency stabilities of 2×10^{-15} at 1 s and 4×10^{-18} at 1000 s across a 90 km fibre network. The optical carrier dissemination scheme uses a fibre interferometric configuration to compensate for any phase noise accumulated along the transmission link. In addition, the polarization of the transmitted signal was maintained using an active polarization control system. In the experiment a 1550 nm optical signal was disseminated along the round-trip fibre network made possible by two optical circulators. An AOM located at the local site was driven by a 100 MHz voltage controlled oscillator (VCO) while a second AOM placed at the remote site was driven by a 55 MHz phase locked oscillator. The AOM situated at the remote end

was used to differentiate the returned signal from reflections originating at connection or splice points. The frequency of the optical signal that completed the round-trip, which passed both AOM's, was shifted twice by -90 MHz. A 90 MHz beat signal was down converted by a factor of 50 to 1.8 MHz using a direct digital synthesizer. Using a frequency mixer, the divided signal is mixed with a 1.8 MHz stable reference associated to a hydrogen maser. The resultant mixing product was amplified, filtered, and used to adjust the phase of the VCO thereby compensating the fibre-induced noise (Fujieda et al., 2011, p. 16498-16507).

An optical frequency at 1.542 μm was coherently disseminated across a 120 km telecom fibre network between Tsukuba and Tokyo, where a fractional frequency stability of 8×10^{-16} at 1 s along the one-way transmission path was reported (Musha, Hong, Nakagawa & Ueda, 2008a, p. 16459-16466). A 10 mW optical signal emitted by a DFB laser was split using an optical coupler. The less intense part of the divided signal served as the reference while the high power component passed through a piezo-driven fibre stretcher and an AOM before being disseminated across the optical path. Once at the remote end, an external-cavity laser diode was phase locked to the transmitted signal with an offset frequency of 40 MHz and subsequently returned to the local site. At the local site the AOM applied a 2 x 55 MHz shift on the frequency of the round-trip signal. In order to obtain the optical phase signal, a digital phase-frequency discriminator (DPFD) assumed the role of a frequency mixer. The error signal generated by the DPFD was used to control a piezo-driven fibre stretcher, thereby suppressing all fibre induced phase fluctuations along the round-trip. Using a lowpass filter, the lower frequency band of the error signal was applied to a second direct digital synthesizer (DDS) via an analog-to-digital converter (ADC). Subsequently, the driving frequency of the AOM was tuned causing the dynamic range of the phase actuator to be lengthened (Musha, Hong, Nakagawa & Ueda, 2008a, p. 16459-16466).

4.4 Microwave and optical frequency transfer with a frequency comb

Frequency or microwave comb generators are commercially available devices that produce an equally spaced, sharp line frequency spectrum. Optical frequency comb generators have been constructed by injecting a continuous, monochromatic light

wave into a lasing cavity that includes an electro-optic modulator (Kourogi, Nakagawa & Ohtsu, 1993, p. 2693-2701; Ye & Cundiff, 2005, p. 19). Simultaneous distribution of microwave and optical frequencies across fibre networks is realized by disseminating a stable optical frequency comb. At the receiver end a photodiode can be used to extract a series of microwave frequency harmonics alternatively, the optical modes can be directly utilized (Marra, 2013, p. 34).

In a paper published by Marra et al., (2011, p. 511-513), an ultra stable microwave frequency was disseminated along 86 km deployed fibre by transmitting a 30 nm wide optical frequency comb. A pulse train consisting of 150 fs long optical pulses was emitted from a 1560 nm mode-locked fibre laser. Before transmission, the optical pulses were launched into a 90:10 splitter where 10% of the divided light was used as a reference signal whereas the remaining 90% of the pulse trains were disseminated along the JANET-Aurora fibre network. An optical circulator located at the transmission end was used to distinguish between the signals disseminated along the fibre network from that returned after the round-trip. Optical losses along the fibre network were compensated for using an erbium doped optical amplifier and a second circulator placed at the receiver end (Marra et al., 2011, p. 511-513). The phase comparison measurements between the returned and reference signals was accomplished using a microwave mixer together with a frequency divider. To compensate for all fibre path length variations, an error signal was generated during the mixing process. The resultant error signal was used for feedback control of the actuator consisting of two cascaded fibre stretchers and a 300 m thermally controlled spool of fibre. A frequency stability of 4×10^{-17} after 1600 s was recorded at the remote site (Marra et al., 2011, p. 511-513).

Experiments based on the distribution of stable microwave signals using a frequency comb consisting of a 1550 nm mode-locked erbium fibre laser reported the emission of sub picosecond optical pulses (Hou, Li, Liu, Zhao & Zhang, 2011, p. 506-511). In the experiment, the mode-locked fibre laser was phase locked to a stable rubidium source where the optical output was split into two separate paths. A DDS was incorporated into the dissemination scheme and utilized as an electronic phase shifter. By adopting a frequency multiplying technique, an error signal was produced by mixing the amplified round-trip and reference signals. Thereafter, the error signal was

applied to the DDS phase shifter thereby compensating the phase variations along the fibre. When the active phase compensation was applied frequency stabilities of 8×10^{-10} at 1 s and 8×10^{-11} at 1000 s were reported. The transmission path was made up of an 80 km fibre link joining the local and remote sites (Hou et al., 2011, p. 506-511).

To study the instability of the distribution of optical frequency standards, the output of a 1550 nm mode-locked laser was divided (Holman, Jones, Hudson & Ye, 2004, p. 1554-1556). One part of the beam was used at the local site while the other portion was transmitted to the remote site along a 6.9 km round-trip network. Upon transmission the eighth harmonic of the individual optical signals was detected using a photodiode and mixed. The signal detected at the local end was frequency shifted by 10 kHz with a single sideband generator. A fast Fourier transform (FFT) was applied to the mixing output for frequency domain analysis at the base band region. A frequency stability of 3×10^{-14} at 1 s along the 6.9 km fibre was measured (Holman, Jones, Hudson & Ye, 2004, p. 1554-1556).

Gollapalli & Duan (2010, p. 904-910) experimentally demonstrated the atmospheric transfer of microwave timing signals using a femtosecond frequency comb in free space as opposed to optical fibre. The microwave signals were transferred over a 60 m free space optical transmission path achieving a transfer stability of parts in 10^{-12} at 1 s and approximately 1×10^{-15} at 500 s.

4.5 Comparative summary of existing time and frequency dissemination schemes

Sections 4.2, 4.3 and 4.4 give some insight into the different approaches for realizing stable and accurate dissemination of clock signals across optical fibre networks. The aim of this section is to provide a summary of numerous time and frequency distribution systems developed by various research groups. Many comprehensive studies into the phase fluctuations in both buried and aerial fibre have been undertaken throughout the years. A successful phase noise compensator must also respond rapidly enough to track the phase changes along the fibre link. Some illustrative examples of implementations of these phase noise compensation strategies from the literature are briefly summarized in Table 4.1.

Table 4.1: A summary of various successful phase noise compensation schemes.

Reference	Fibre Length	$\sigma_y(1s)$	$\sigma_y(100s)$	$\sigma_y(1000s)$	Laser Source	Wavelength	Clock Source
Predehl et al., 2012	920 km	5×10^{-15}	$\approx 10^{-18}$	$\approx 10^{-19}$	DFB	1542 nm	unspecified
Marra et al., 2012	7.7 km	4×10^{-17}	$\approx 10^{-17}$	$\approx 10^{-18}$	Er doped MLL	1.56 μm	H-maser
Lopez et al., 2008	86 km	5×10^{-15}	$\approx 10^{-16}$	$\approx 10^{-17}$	DFB	1550 nm	unspecified
Wang et al., 2012c	80 km	1.3×10^{-14}	$\approx 10^{-16}$	$\approx 10^{-16}$	DFB	unspecified	Cs clock
Clivati et al., 2017	550 km	unspecified	unspecified	unspecified	unspecified	1.5 μm	H-maser
Slivczynski et al., 2011	60 km	$\approx 10^{-14}$	$\approx 10^{-15}$	$\approx 10^{-15}$	DFB	unspecified	SMB100A
Gollapalli et al., 2010	Free space	$\approx 10^{-12}$	$\approx 10^{-14}$	unspecified	Precision Photonics FFL-1560	1560 nm	unspecified
Musha et al., 2008a	120 km	8×10^{-16}	unspecified	unspecified	DFB	1542 nm	H-maser
Foreman et al., 2007	32 km	$\approx 10^{-17}$	$\approx 10^{-18}$	$\approx 10^{-18}$	unspecified	1064 nm	unspecified
Wang et al., 2015	50 km	3.7×10^{-14}	$\approx 10^{-15}$	$\approx 10^{-15}$	Diode laser	1547.72 nm	H-maser
Bercy et al., 2014	100 km	7×10^{-18}	$\approx 10^{-20}$	$\approx 10^{-21}$	unspecified	1.5 μm	unspecified
McCool et al., 2008	28.8/110.8km	1×10^{-12}	$\approx 10^{-13}$	$\approx 10^{-14}$	unspecified	1550.31 nm	H-maser
Wilcox et al., 2009	2.2 km	$\approx 10^{-14}$	$\approx 10^{-16}$	$\approx 10^{-17}$	unspecified	1560 nm	Rb clock
Musha et al., 2008b	110 km	1.5×10^{-15}	unspecified	unspecified	f-DFB	1543 nm	unspecified
Li et al., 2017	1100 km	7.7×10^{-13}	$\approx 10^{-14}$	$\approx 10^{-16}$	DFB	1556.55/1550.12nm	SMB100A
Sato et al., 2000	unspecified	$\approx 10^{-14}$	$\approx 10^{-16}$	7.5×10^{-17}	Diode laser	1.3/1.5 μm	H-maser

The time and frequency dissemination techniques discussed in this chapter allows for the transfer of stable signal across optical fibre or in some cases through free space. However, the preferred design strategy adopted for realizing the transfer of stable signals across a transmission medium depends on factors such as application, requirements, costs, project specification and reproducibility. The chapter that follows introduces different components used for implementing highly stable time and frequency dissemination schemes within optical fibre networks.

CHAPTER 5

IMPLEMENTATION OF TIME AND FREQUENCY SYSTEMS OVER OPTICAL FIBRE NETWORKS

The following chapter provides a theoretical summary of the diverse technologies that can be integrated into optical fibre based time and frequency distribution systems. A sound understanding of the various optical communication components is required before developing a fibre based timing network. This chapter begins by discussing the application of vertical cavity surface emitting laser (VCSEL) and distributed feedback (DFB) laser sources in time and frequency optical networks. The chapter further examines the different frequency standards commercially available. A brief review of optical fibre impairments, such as signal attenuation, chromatic dispersion (CD) and polarization mode dispersion (PMD) is provided. Finally, a brief theoretical review of wavelength conversion and the associated conversion techniques is given.

5.1 Optical transmitters

In a typical optical fibre communication system, an optical transmitter converts the input electrical signal into an output optical signal for transmission along the fibre. The transmitters generally comprise of an optical source, a signal modulator and a transmission channel coupler. Optical sources may include light-emitting diodes (LED) or semiconductor lasers. By modulating the optical carrier wave, an optical signal is then generated. Semiconductor optical laser sources such as VCSEL or DFB lasers can be directly modulated by changing the injection current, however external modulating techniques are occasionally employed (Agrawal, 2012, p. 17).

5.1.1 Vertical cavity surface emitting laser (VCSEL)

Vertical cavity surface emitting lasers (VCSELs) are low cost semiconductor optical sources offering high bandwidth with single mode lasing operation within the O and C band. Unlike conventional laser sources, VCSELs emit light perpendicular to the planes of its active region (Gibbon et al., 2010, p. 41-45; Michalzik, 2012, p. 19-22). Figure 5.1 illustrates the typical layout structure of a VCSEL. The inner cavity contains the amplifying layers surrounded by two distributed Bragg reflector (DBR)

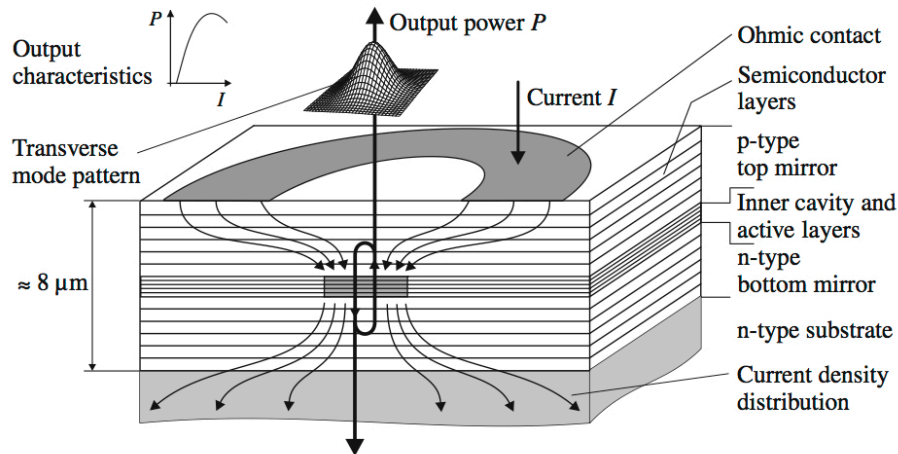


Figure 5.1: Schematic layer structure of a VCSEL (Michalzik, 2012, p. 22).

mirrors which provide optical feedback within the active gain region. Because the VCSEL emits light orthogonal to the active layer region, amplification occurs during a specific period of the cavity round-trip. The inner active region of the VCSEL can be minimized, resulting in single mode operation at the preferred lasing wavelength. The short cavity length eliminates the production of longitudinal modes associated with Fabry-Pérot cavities (Kipnoo, 2015, p. 20; Kim, 2010, p. 69-70).

The success of the VCSEL emerges from a collection of distinctive properties. The VCSEL requires low threshold currents, therefore reducing the optical power consumption to the milliwatt region. These currents are used to drive VCSEL during the lasing operation. Furthermore, the VCSEL exhibits outstanding digital modulation performance at 40 Gbps data rates. VCSELs have exceptional beam quality since they emit a circular beam with a small divergence angle. Generally, VCSELs are considered to be low cost laser sources in comparison to DFB lasers due to its modest manufacturing costs (Michalzik, 2012, p. 20). Chromatic dispersion and frequency chirping are the major flaws experienced by the VCSEL during direct modulation operation. However, there are several methods available to restrict and minimize these effects. These techniques include injection locking and filter offsetting to narrow the spectrum (Gibbon et al., 2011, p. 41-45; Harder, Vahala & Yariv, 1983, p. 328-330; Koch & Linke, 1986, p. 613-616).

5.1.2 Distributed feedback (DFB) laser

Distributed feedback (DFB) lasers are directly modulated, high-power optical sources that form part of the semiconductor laser group. The lasing cavity has a corrugated architecture thereby permitting the emission and oscillation of distinct wavelengths only. As a result, the DFB laser generates a narrow linewidth, optical signal making it ideal for Dense Wavelength Division Multiplexing (DWDM) transmission systems (Massa, 2000, p. 324). DFB lasers have relatively high threshold currents, compared to VCSELs. Li et al. (2014, p. 4059-4064) experimentally examined the operational behaviour of DFB lasers and reported lasing thresholds of 16 mA at 25° C and 22 mA at 45° C (Li et al., 2014, p. 4063). DFB lasers are better suited for long-haul transmission due to its narrow linewidth property. The optical output wavelength of a DFB laser can be tuned by varying the internal cavity temperature.

The optimal method in which to lase a directly modulated laser, such as the DFB or VCSEL, is to apply a bias current at the midpoint of the linear region along the transfer curve, as shown in experimental results in Figure 5.2. The ideal bias point is typically located midway between the lasing threshold and the rollover current levels.

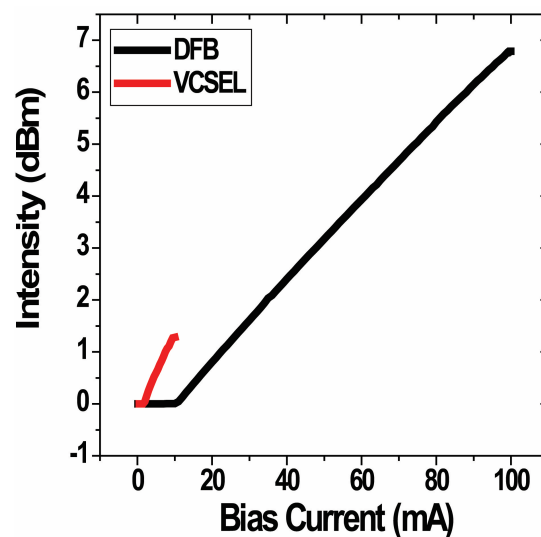


Figure 5.2: Typical transfer curves showing the optical output power of a DFB and VCSEL as a function of bias.

5.2 Atomic clocks

Atoms and molecules have distinctive resonance features, absorbing and emitting photons at a stable and precise frequency. As atomic clocks become more precise and accurate, the timekeeping fraternity has desired ultra-stable timing systems to assist with synchronization (Behrendt & Fodero, 2006, p. 17-19).

5.2.1 Cesium (Cs)

Cesium (Cs) atomic clocks or standards are best preferred for long-term stability applications. Cs clocks utilize state selection magnets to deflect the Cs atoms of particular atomic levels by various amounts, as opposed to the optical pumping mechanism occurring within the rubidium source. As the Cs atoms pass through the strong diverging magnetic field, they get deflected. This deflection is dependent on the energy state of the Cs atoms and its magnetic moment induced by the force applied as a result of the magnetic field (Essen & Parry, 1955, p. 280-282; Lewis, 1991, p. 927-935). Based on their magnetic moments, the atoms located in the $F=3$ hyperfine levels of the Cs^{133} ground state are physically detached from those in the $F=4$ level. Any interactions with microwave signals at 9191631770 Hz stimulates the transition of Cs atoms from the $F=3$ hyperfine level to the $F=4$ level. Improved performance of the Cs standards resulted in the definition of the SI second, described in terms of the splitting of the Cs^{133} atom. It is given as the duration of 9,191,631,770 periods of radiation associated with the transition between the hyperfine levels of the ground state of the Cs atom (BIPM, 2014, p. 113). The use of Cs atomic clocks is advantageous due to its extreme accuracy, long-term stability and reproducibility. Typical Allan variance performance specification of high-end commercial Cs atomic clocks is illustratively shown in Figure 5.3 (Tavella, 2008, p. S183-S192).

5.2.2 Rubidium (Rb)

The rubidium (Rb) atomic clock is characteristically known for being compact and is based on the resonance of the free Rb atom situated between energy levels. As is the case with hydrogen, the ground state of Rb^{87} is divided into two hyperfine levels. These hyperfine levels are further divided into Zeeman sublevels, each described by quantum number m_F . The resonance occurs within the microwave region of the electromagnetic spectrum and the distance between the discrete quantum levels is a result of the electron nuclear hyperfine interaction (Camparo, 2007, p. 33-39; Major,

1998, p. 161). The internal operational mechanism of the Rb clock is similar to the Cs atomic source, with the difference lying in the state selection process. State selection and detection within the Rb clock is achieved by optical pumping. The Rb clock system is made up of a Rb⁸⁷ discharge lamp, a Rb⁸⁵ vapor filter cell and a resonance cell consisting of a Rb⁸⁷ vapor, including a buffer gas (Camparo, 2007, p. 33-39). The accuracy provided by the Rb atomic clock is similar to the Cs standard, with an operational expectancy of approximately five times that of Cs.

5.2.3 Hydrogen (H)-Maser

The development of hydrogen (H)-masers in recent years has been steered towards building smaller and more compact devices, while maintaining its frequency stability. Typical H-masers are large and weighty devices. In addition to several other components, H-masers contain a microwave cavity for maser oscillation, a vacuum pumping system and a hydrogen source. Traditional H-maser atomic clocks operating in the active mode were oscillating at 1.42 GHz. However, passive design configurations have shown a reduction in the drift performance for periods greater than ten days (Howe & Walls, 1983, p. 218-223; Ito et al., 2003, 85-94). The most significant characteristic of the H-maser is its exceptionally high short-term stability, relative to the Cs and Rb standards. As a result of this unique quality, the H-maser is therefore better suited for very long baseline interferometers (VLBIs) applications.

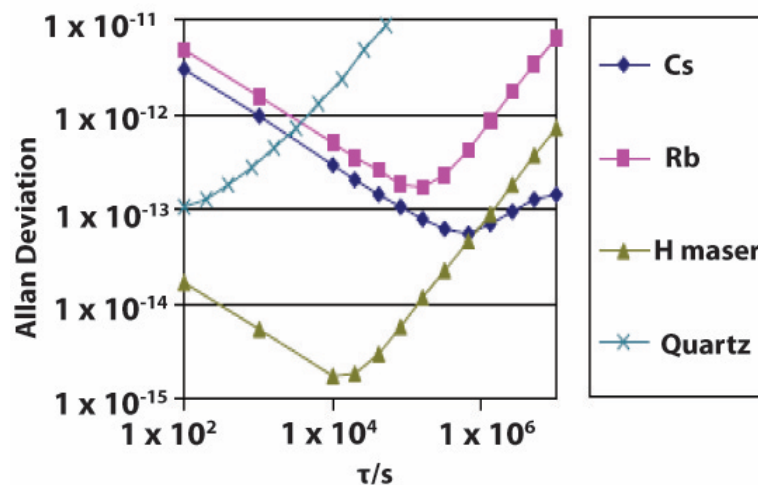


Figure 5.3: Allan variance plots of various high performance atomic clocks (Tavella, 2008, p. S183-S192).

Typical Allan variance curves for Cs, Rb, H-maser and Quartz high performance atomic clocks are illustratively shown in Figure 5.3 (Tavella, 2008, p. S183-S192).

5.3 Optical fibre signal impairments

The function of an optical fibre communication link is to disseminate the data from a transmitter to a receiver without distorting and corrupting it. Almost all lightwave telecommunication systems use optical fibre as a transmission medium because of their high data capacity, low optical attenuation properties and high resistance to electromagnetic interference. As the telecommunication systems evolved to higher bit rates and transmission distances increase, linear and nonlinear effects experienced by optical signals propagating along fibre become the limiting factors. Nonlinearities stemming from the high optical power includes self-phase modulation (SPM), cross-phase modulation (XPM), four-wave mixing (FWM), stimulated Raman scattering (SRS) and stimulated Brillouin scattering (SBS). However, linear effects include fibre properties such as attenuation and chromatic dispersion (CD) (Agrawal, 2007, p. 13-18; Agrawal, 2012, p. 50-57). Generally, optical fibres are categorized according to their refractive index distribution within the core. As a result of this refractive index distribution, optical fibres are divided into two groups, step index fibre and graded index fibre. Furthermore, these fibres can either be single mode fibres (SMF) or multimode fibres (MMF).

5.3.1 Attenuation

One of the limiting factors that degrade the quality of the optical signal during propagation is attenuation. The transmitted power of the signal along fibre is mathematically given as,

$$P_0 = P_i e^{(-\alpha L)} \quad (5.1)$$

where P and P_0 are the optical output and input powers respectively, α is the attenuation coefficient and L is the length of the fibre. Traditionally, the attenuation coefficient is given by Equation 5.2,

$$\alpha \left(\frac{dB}{km} \right) = -\frac{10}{L} \text{Log}_{10} \left(\frac{P_0}{P_i} \right) \quad (5.2)$$

and is expressed in units of dB/km (Agrawal, 2012, p. 55). Optical attenuation stems from fibre related intrinsic and extrinsic effects. Intrinsic losses include mechanisms, such as material absorption and Rayleigh scattering within the fibre core region. However, extrinsic loss mechanisms include bending-losses, core/cladding losses, splice and connector losses.

5.3.2 Polarization mode dispersion (PMD)

Collectively, birefringence and modal dispersion are the two effects responsible for polarization mode dispersion (PMD) within the optical fibre. Apart from chromatic dispersion, PMD is another source of pulse broadening within the optical fibre, arising from the difference in the group velocities of the two orthogonal polarization eigenmodes (Keiser, 2000, p. 113-115; Rashleigh, 1983, p. 312-331). Generally, polarization refers to the orientation of an electromagnetic wave during propagation

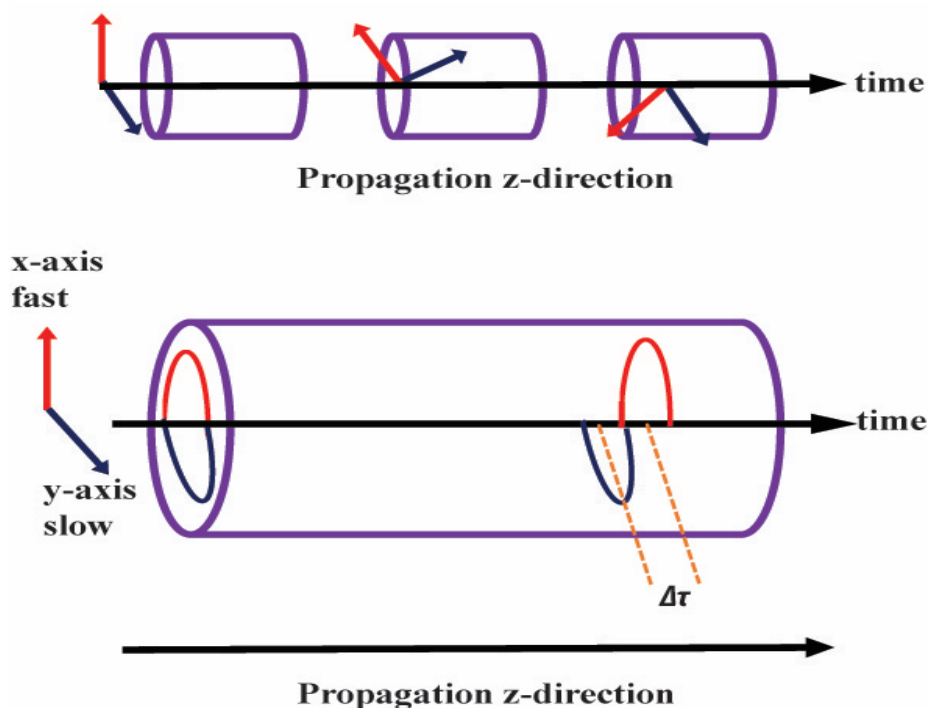


Figure 5.4: Illustrative description of PMD effects in optical fibre and the birefringent axis at different fibre sections.

within a medium. The transverse electric field has one of its orthogonal modes arbitrary polarized along the x-axis, whereas the remaining independent mode is polarized along the y-axis.

For an ideal fibre displaying perfect circular symmetry, its refractive index profile will be uniform throughout. Hence, the two polarization modes will remain unchanged and propagate with equal velocities ($v_x = v_y$) along the optical fibre. Similarly, the two polarization mode are considered to be degenerate, having equal propagation constants ($k_x = k_y$) (Keiser, 2000, p. 113-115; Rashleigh, 1983, p. 312-331).

In reality, optical fibre contains inherent imperfections that perturb the perfect rotational symmetry. Noncircular core, non-uniformity of refractive index profiles, fibre bending and irregular lateral stresses collectively contributes to the imperfections within the fibre. The difference in the effective refractive index profile along the length of the fibre is referred to as birefringence, mathematically expressed as $B_f = n_y - n_x$ (Keiser, 2000, p. 113-115; Rashleigh, 1983, p. 312-331). Consequently, the orthogonal polarization eigenmodes propagate at different velocities with respect to each other, resulting in a differential time delay, $\Delta\tau$, between the modes. An illustration is shown in Figure 5.4. The differential time delay is also referred to as the differential group delay (DGD). Since the birefringence varies along the optical fibre, it is possible to represent the length of fibre as a concatenated series of birefringent segments separated by mode coupling sites. An illustration of this phenomenon can be seen in Figure 5.4. Mode coupling refers to the exchange or coupling of energy between modes of neighbouring birefringent sections. Mode coupling sections arise due to variations of the fibre diameter, structural imperfection, fibre bending and changes in the refractive index profile along the fibre length. In single mode fibre, coupling lengths may be anywhere between 5 m to 15 m (Hutter, B. Gisin & N. Gisin, 1999, pp. 1843-1848). There are numerous excellent review articles on PMD in the literary world (Gordon & Kogelnik, 2000, p. 4541-4550; Heismann, 1998, p. 51-79; Poole & Nagel, 1997, p. 114-161).

5.3.3 Chromatic dispersion (CD)

A modulated optical signal propagating along a fibre consists of an infinite number of spectral components with an associated frequency, ω . The individual spectral components propagate independently to each other with distinct group velocities, v_g ,



Figure 5.5: Chromatic dispersion effects in an optical fibre.

therefore resulting in the propagation group delays, τ_g . The group velocity is mathematically expressed as:

$$v_g = \left(\frac{d\beta}{d\omega} \right)^{-1} = \frac{c}{n_g} \quad (5.3)$$

where β refers to the propagation constant and n_g to the group refractive index (Agrawal, 2002, p. 38; Kazovsky et al, 2011, p. 47; Keiser, 2000, p. 107). Equation 5.3 mathematically illustrates the frequency and refractive index dependence on the group velocity. Consequently, the individual spectral components propagate at different group velocities, thereby causing the optical pulse to spread and broaden over time, as seen in Figure 5.5. This mechanism of pulse dispersion is referred to as chromatic dispersion.

The overall broadening experienced by the propagating pulse due to the chromatic dispersion along the optical fibre is defined as (Agrawal, 2002, p. 38; Keiser, 2000, p. 107),

$$\Delta\tau = l \frac{d^2\beta}{d\omega^2} \Delta\omega \quad (5.4)$$

where l is the fibre length and $d^2\beta/d\omega^2$ is a second order derivative of the propagation constant. Since

$$\Delta\omega = \left(-\frac{2\pi c}{\lambda^2} \right) \Delta\lambda \quad (5.5)$$

the chromatic dispersion coefficient or dispersion parameter is mathematically expressed as,

$$D = \frac{1}{l} \frac{\Delta\tau}{\Delta\lambda} = \frac{d}{d\lambda} \left(\frac{1}{v_g} \right) = -\frac{2\pi c}{\lambda^2} \beta_2 \quad (5.6)$$

and is given in units of ps/(nm.km) (Agrawal, 2002, p. 38; Kazovsky et al., 2011, p. 49; Keiser, 2000, p. 107). Chromatic dispersion can be written as $D = D_M + D_W$, where D_M and D_W refer to material and waveguide dispersion, respectively (Agrawal, 2002, p. 41; Bogatyrev et al., 1991, p. 561). Material dispersion arises because the refractive index of silica changes with optical wavelength or frequency. Waveguide dispersion occurs due to the wavelength dependence of the core diameter as well as the refractive index difference (Agrawal, 2002, p. 38-42).

For optimal transmission performance, together with effective phase noise compensation, the correct selection of optical and electrical components and implementation techniques is crucial towards the development of an active time and frequency dissemination system. Low power and cost effective wavelength tunable optical sources such as DFB and VCSELs, both operating at 1310 nm and 1550 nm, have been described. DFB lasers are better suited for long distance transmission compared to VCSELs due to its optical power and chirping properties. However, VCSELs are more favourable for DWDM systems due to its wavelength tunability property and cost trade-off. Furthermore, signal impairments associated with an optical fibre such as attenuation, PMD and CD have been explained.

5.4 Theoretical overview of optical wavelength conversion

Research into wavelength conversion technology intensified due to the growing need to control several optical channels in complex and intelligent optical network systems. It was realized that wavelength switching within a composite network creates conflict when transmitters situated at different nodes transmit signals of identical wavelength to the same destination. The only way to overcome this drawback was to shift optical channels to different wavelengths, hence creating the need for wavelength conversion technology. The function of a wavelength converter is to convert data on an incident optical carrier signal λ_i onto a new output wavelength λ_c , as seen in Figure 5.6. All-optical wavelength converters are set to become crucial components in broadband networks and can be used to prevent wavelength blocking of forward signals, simplicity wavelength control and regenerate data (Kaur, Singh & Utreja, 2013, p.

338-344; Lavrova, Rau & Blumenthal, 2002, p. 712-717). Equally as important, wavelength conversion technology facilitates the idea of decentralized network management of the various wavelength routes within the network (Durhuus, Mikkelsen, Joergensen, Danielsen & Stubkjaer, 1996, p. 942-954; Sato, 1994, p. 919-926; Sato, Okamoto & Hadama, 1994, p. 159-170). Wavelength conversion itself can be performed in either the electrical or the optical domain. Several techniques have been developed and proposed to achieve wavelength conversion. Apart from the conventional opto-electronic converter, the most widely studied configurations are the all-optical wavelength conversion techniques utilizing semiconducting devices such as semiconductor optical amplifiers (SOAs) together with four wave mixing (FWM), cross-phase (XPM) or cross-gain modulation (XGM) (Danielsen et al., 1997, p. 94-95). Another all-optical technique using a laser-to-laser configuration for achieving wavelength switching is the laser converter method (Stubkjaer K.E. et al., 1997, p.103-117).



Figure 5.6: Wavelength converter functionality (Ramamurthy & Mukherjee, 1998, p. 1061- 1073).

5.4.1: Opto-electronic converters

A clear-cut and simple technique to achieve wavelength conversion is by using an opto-electro-optic converter. Such a system consists of a transmitting optical source, a detector followed by another laser that retransmits the incoming signal on the new wavelength (Kaur, Singh & Utreja, 2013, p. 338-344). In this method, the incident optical beam, λ_i , is first detected and translated to the electrical domain using a photodetector (PD). Thereafter the electrical signal is used to drive the input of a tunable laser tuned to the desired new lasing wavelength, λ_c , as seen in Figure 5.7.

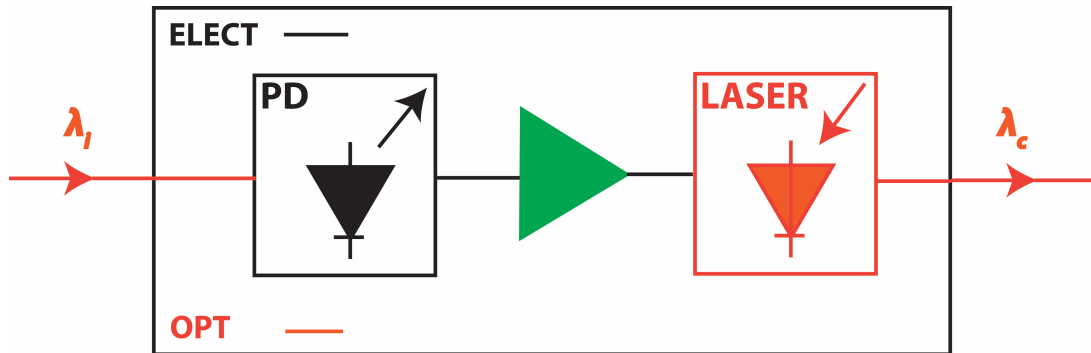


Figure 5.7: Schematic of an opto-electronic wavelength converter (Kaur, Singh & Utreja, 2013, p. 338-344).

5.4.2: Four-wave mixing (FWM) wavelength converter

Another method for achieving wavelength conversion is exploiting four-wave mixing (FWM) in an optical fibre (Raghunathan, Claps, Dimitropoulos & Jalali, 2004, p. 34-36). FWM wavelength conversion occurs when a pump wave, λ_p , is injected into a SOA together with a signal wave, λ_s , as illustrated in Figure 5.8.

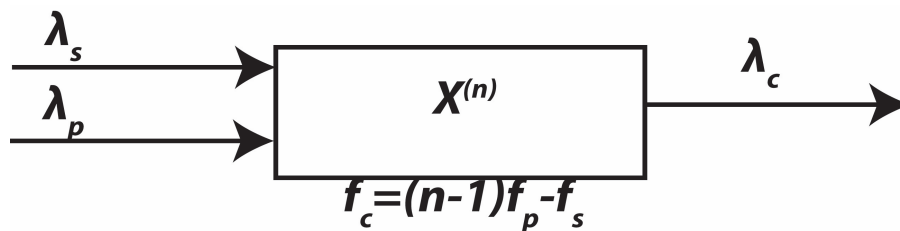


Figure 5.8: Four wave mixing wavelength converter (Ramamurthy & Mukherjee, 1998, p. 1061- 1073).

A new converted wavelength, $1/\lambda_c = 2/\lambda_p - 1/\lambda_s$, is generated through the third-order nonlinear susceptibility $\chi^{(3)}$ (Gao et al, 2010, p. 195-200; Mohammed & Radman, 2017, p. 1-5).

5.4.3: Cross gain modulation (XGM) SOA wavelength converter

An additional approach for the realization of wavelength conversion is by cross gain modulation (XGM) in a SOA. The principle is illustrated in Figure 5.9, an amplitude modulated incident wave, λ_s , modulates the gain in the SOA due to gain saturation. A continuous wave (CW), λ_c , tuned to the desired output optical wavelength is then modulated by the gain variation within the SOA, thereby carrying the exact

information as the intensity modulated input signal. The injected input and the CW signals can either be co-directional or counter-directional. The resultant output of the XGM SOA technique yields an inverted and converted signal, λ_c , with reference to the input signal (Durhuus et al., 1996, p. 942-954).



Figure 5.9: SOA cross gain modulation wavelength converter (Ramamurthy & Mukherjee, 1998, p. 1061- 1073).

5.4.4: Cross phase modulation (XPM) SOA wavelength converter

In a cross phase modulation (XPM) wavelength converter the refractive index of the SOA is dependent on the carrier density in its active region (Ramamurthy & Mukherjee, 1998, p. 1061- 1073). An incident signal depletes the carrier density and modulates the refractive index of the SOA, resulting in phase modulation of a CW signal, λ_c , coupled into the converter (Durhuus et al., 1996, p. 942-954; Lacey, Pendock & Tucker, 1996, p.125-126.). The SOA can be incorporated into an interferometric configuration such that a converted amplitude modulated signal, λ_c , is produced at the output, as shown in Figure 5.10.

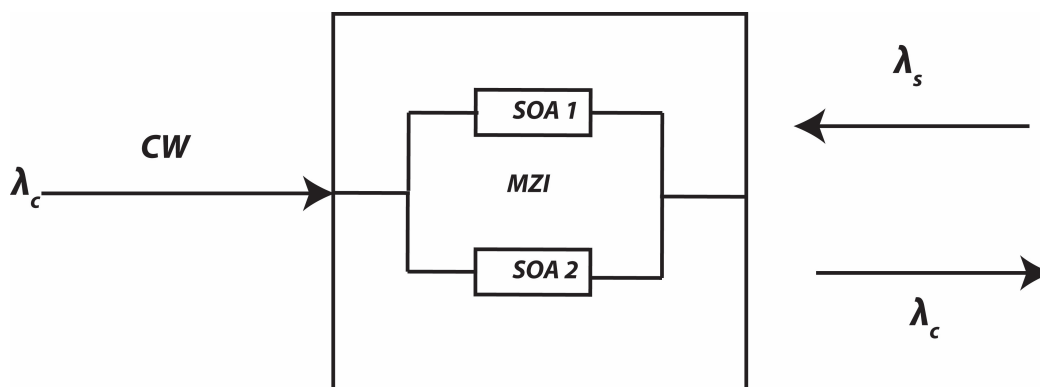


Figure 5.10: Wavelength converter based on cross phase modulation (Ramamurthy & Mukherjee, 1998, p. 1061- 1073).

5.4.5: Laser converters

In this all-optical wavelength conversion approach, an intensity modulated incident beam, λ_p , emitted from the master or probe laser is injected into the cavity of the tunable or slave laser. Moreover, the modulated input signal from the master laser is

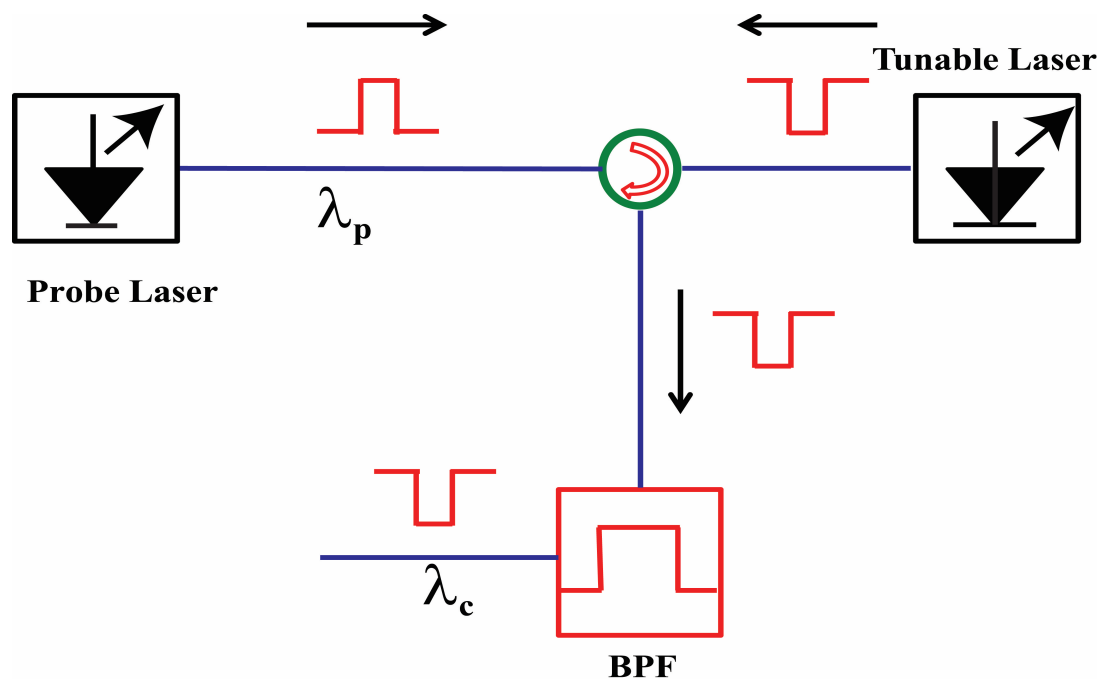


Figure 5.11: Schematic of a wavelength conversion setup using gain suppression (Lavrova et al., 2002, p. 712-717; (Wassin, Isoe, Gamatham, Leitch & Gibbon, 2017, p. 101290G-1-101290G-12).

injected directly into the side mode of the slave laser, as illustrated in Figure 5.11. During this process, the side mode is optically stimulated, thereby vibrating within the gain medium (Boiyo et al., 2016a, p. 17-20). Consequently, the dominant primary mode of the tunable or slave laser is suppressed whilst the injected side mode is amplified or switched on. As a result, the data carried by the injected probe wavelength is then inverted and converted to the new lasing wavelength, λ_c (Boiyo et al., 2016a, p. 17-20; Boiyo et al., 2016b, p. 30-35; Chang, Chrostowski, Chang-Hasnain & Chow, 2002, p. 1635-1637; Lavrova et al., 2002, p. 712-717).

The next chapter presents the first experimental results of a highly accurate PPS-timing system used for optical fibre latency measurements.

CHAPTER 6

EXPERIMENTAL DEMONSTRATION OF A PPS-TIMING SYSTEM USED FOR OPTICAL FIBRE LATENCY MEASUREMENTS WITHIN NEXT GENERATION TELESCOPE ARRAY DATA TRANSPORT NETWORK

Latency or time delay induced by the optical fibre due to its refractive index properties and external environmental conditions cannot be eradicated (Dong, Wang, Gao, Guo & Wang, 2016, p. 1368-1375). Synchronization and timing in telescope fibre networks is an essential requirement as it ensures phase coherence within the antenna array (Epstein, Olsson & Rotman, 2016, p. 482-486; Wang et al., 2012, p. 1-5). Optical fibre based time delay measurements are crucial for such applications. Conventional latency measurements were achieved using optical time domain reflectometers (OTDR) or time interval counters (TIC). However, they have unfavourable properties such as existing dead zones and low accuracy. This chapter presents a novel technique for measuring the propagation time delay along the optical fibre using precise and accurate pulse per second (PPS) signals. The approach was based on all-optical wavelength conversion using a C-band vertical-cavity surface-emitting laser (VCSEL). Further in this chapter an all-optical VCSEL wavelength conversion in the 1550 nm transmission region is experimentally demonstrated. Thereafter, the chapter will focus on the presentation of the experimental design and operation of the PPS-timing latency measurement system, followed by the related propagation delay results.

6.1 Experimental design and implementation of the highly accurate PPS-timing system for optical fibre latency measurements

This section presents and describes the all-optical approach used for accurately measuring the latency times of the propagating signal along the fibre under test (FUT). All-optical wavelength conversion was achieved and demonstrated using the technique described in Chapter 5.4.5. The experimental schematic of the PPS-timing, latency measurement system, shown in Figure 6.1, uses two low attenuation C-band optical transmitting sources.

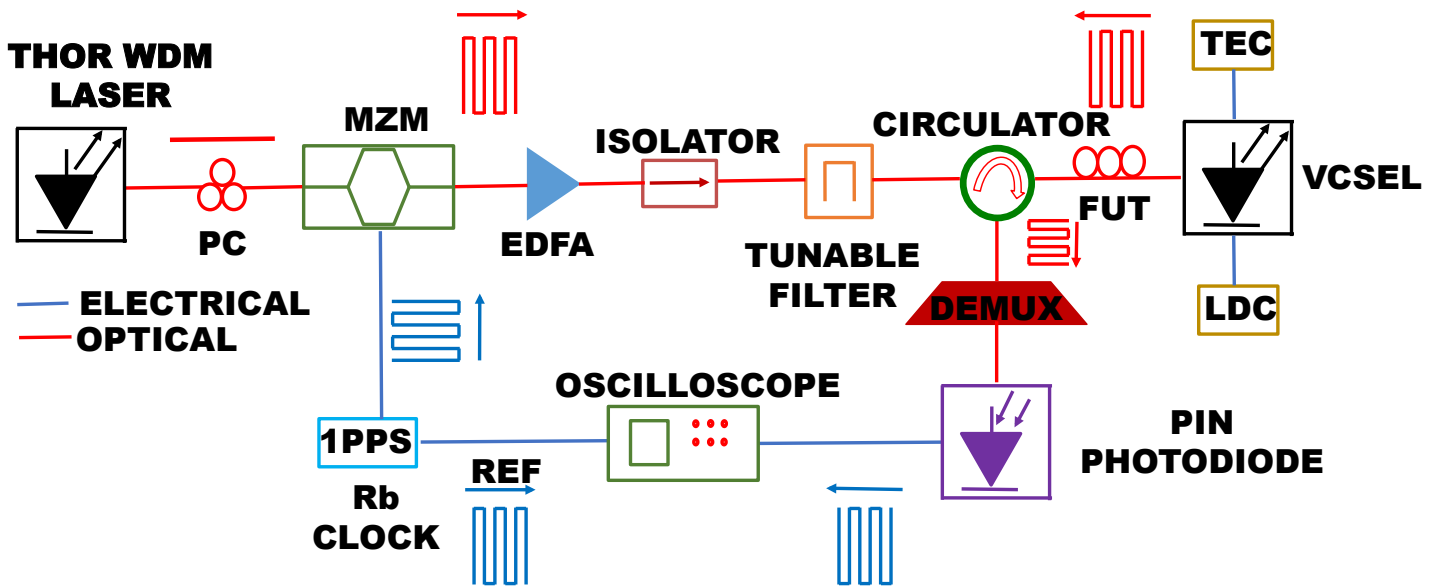


Figure 6.1: Experimental demonstration of the highly accurate PPS-timing latency measurement system.

The key element of the VCSEL's laser cavity, used for all-optical conversion is its wavelength tunability property. The rationale behind the optical latency measurement system is to detect the round-trip propagation time delay between an accurate and stable reference PPS signal and that of the resultant transmitted signal along a fibre. The experimentally measured, two-way time delay was halved in order to determine the transmission times for one-way propagation. In the experimental setup shown in Figure 6.1, a tunable distributed feedback (DFB) optical source embedded within a Thorlabs PRO8 DWDM chassis located at the transmission end represents the master laser, while a 1550 nm, 10 Gbps VCSEL situated at the receiver end signifies the slave laser. Since this approach discussed in this text is based on all-optical wavelength conversion, described in Chapter 5.4.5, it is critical to appropriately choose a master laser such that its primary mode aligns with the secondary mode of the slave laser. Collectively, the DFB lasers contained within the Thorlabs PRO8 DWDM chassis is tunable from 1550.12 nm to 1554.13 nm.

In the latency experiment, a 1551.70 nm unmodulated optical signal with an output power of 5.27 dBm emitted from the ThorLabs DFB tunable laser source was polarization controlled and coupled into a Mach Zehnder Modulator (MZM). The MZM was intentionally biased at $2 V_{pp}$. Since the MZM is polarization sensitive, a three-paddle (quarter-wave plate, half-wave plate, quarter-wave plate) manual fibre

polarization controller (PC) was used to adjust the polarization states of the injected optical signal. The MZM was driven by an electrical PPS signal generated by a highly stable rubidium (Rb) clock with a specified jitter of less than 1 ns. The injected 5 V_{pp} PPS signal was attenuated using a series of electrical attenuators, collectively producing 9 dBm attenuation. Subsequently, the resultant 2 V_{pp} PPS signal guarantees a point on the MZM transfer curve such that the modulated output optical signal is maximized, thereby ensuring an optimized link performance. An erbium doped fibre amplifier (EDFA) was used to amplify the power of the incoming optical PPS beam from the master DFB tunable laser source so as to achieve sufficient power for gain saturation within the lasing cavity of the slave VCSEL. An optical isolator with a 2.1 dB insertion loss was used to suppress and prevent any back reflections to the EDFA. Furthermore, a 0.3 nm full width half maximum (FWHM) tunable optical filter was placed before a passive circulator as to subdue any noise generated from the EDFA and also any undesired wavelengths introduced by the DFB laser source. The optical PPS signal was subsequently transmitted along the fibre link and injected into the side mode of the VCSEL lasing cavity, as illustrated in Figure 6.1. The 1550 nm VCSEL slave laser was purposely biased at 7.85 mA, ensuring a primary lasing wavelength of 1553.30 nm with an optical output power of – 3.64 dBm and a side mode at 1551.70 nm, as seen in Figure 6.3 (b).

The slave VCSEL was biased above its mid-point biasing levels using a laser diode controller (LDC), while the temperature was maintained at 25° C with a thermo electric cooler (TEC). During the side mode injection process two events occur, the first being the all-optical modulation of a VCSEL and the second being wavelength conversion. Wavelength conversion and inversion within the VCSEL is realized as a direct result of the high-powered PPS optical signal being injected into its secondary mode. The incoming transmitted beam is up-converted from 1551.70 nm to 1553.30 nm. Furthermore, the dominant lasing mode within the VCSEL cavity was suppressed while the side mode was stimulated and amplified resulting in inversion. The converted and inverted optical signal was subsequently returned to the transmitting site via a second circulator. Thereafter the new lasing mode of the slave VCSEL was filtered using a 100 GHz channel WDM demultiplexer. The converted and inverted PPS optical signal emanating from within the lasing cavity of the slave

VCSEL was detected using a PIN photodiode with an optical sensitivity of -19 dBm. The resultant signal was subsequently compared to a reference electrical PPS signal as seen in Figure 6.1. The optical fibre latency measurement was realized using a dual channel 2 GSa/s Agilent sampling oscilloscope, as shown in the experimental procedure.

6.2 Optical fibre latency measurements

The results presented in this section was presented and published at the 2017 Photonic West conference (Wassin, Isoe, Gamatham, Leitch & Gibbon, 2017, p. 101290G-1-101290G-12). The experimental demonstration of the PPS latency measurement system is shown in Figure 6.1. The VCSEL utilized in this PPS-timing experiment was operated with a temperature stabilizer or a TEC. A VCSEL is a single-mode semiconductor laser diode with a typical side-mode suppression ratio (SMSR) of 35 dB (Raycan, 2015). In order to validate the operational performance of the VCSEL, the unmodulated static and dynamic characteristics are presented.

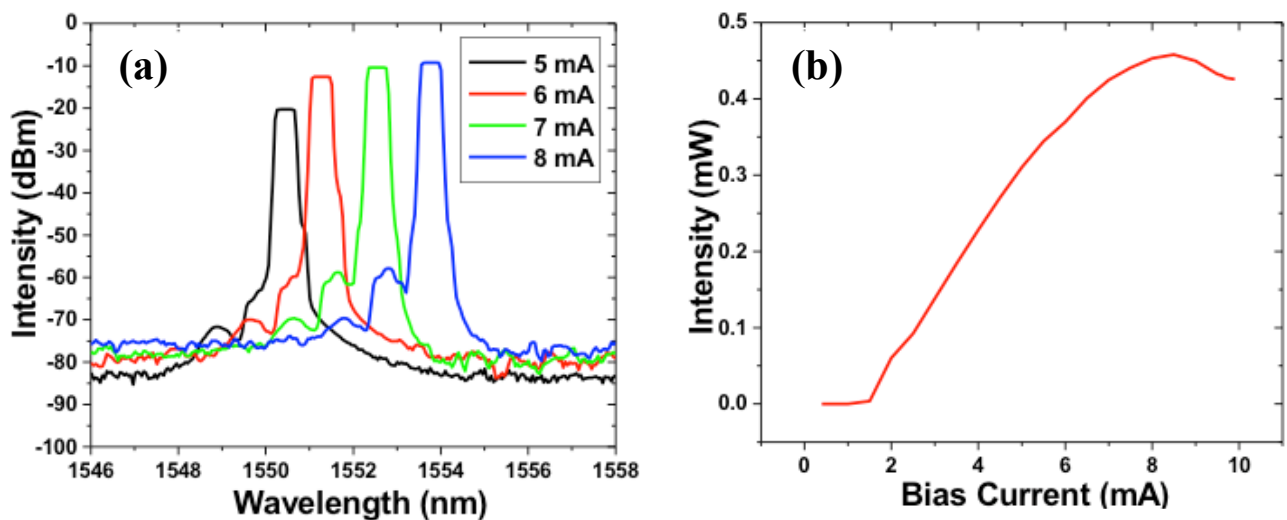


Figure 6.2: Experimental characterization of the unmodulated 1550 nm VCSEL. (a) wavelength response with changing bias and (b) optical output power as a function of bias current.

The wavelength tunability and biasing characteristics of 10 Gbps, 1550 nm slave VCSEL is experimentally demonstrated and presented in Figure 6.2. The graph shows the emission wavelength spectrum tuned from 1550.50 nm to 1554.0 nm, while increasing the bias current from 5 mA to 8 mA. This result clearly shows a shift in the entire spectrum towards a higher wavelength region as the bias current is increased. It

is further evident from Figure 6.2 (a) that a wavelength tunability of 3.5 nm was achieved, equating to a 437.5 GHz bandwidth within the DWDM ITU grid. This result suggests that a VCSEL based DWDM network can be built with approximately eight data transmission channels with a 50 GHz grid spacing. This characteristic makes the VCSEL an attractive technology for data aggregation within telescope optical fibre networks. Figure 6.2 (b) illustratively shows the VCSEL output power measured with varying bias current. Here, the bias current was increased from 0.4 mA to 9.9 mA. As shown in Figure 6.2 (b), the threshold bias point is seen to be approximately 1.5 mA with a roll-over current of 8.5 mA, however a maximum bias current rating of 4 mA is specified in the datasheet (Raycan, 2015). For the results presented in this section, the VCSEL was biased at 7.85 mA, providing an optical output power of -4.50 dBm. It is best practice to bias the VCSEL above the threshold current, preferably at the midpoint of the linear region, along the transfer function curve so as to enable optimum transmission performance.

Figure 6.3 shows the discrete wavelength spectra for the ThorLab DFB and VCSEL laser sources, as measured with an optical spectrum analyzer (OSA). Figure 6.3 (a) illustrates the primary lasing mode of the ThorLab DFB laser source at 1551.70 nm with an optical output power of 5.27 dBm. Furthermore, the dominant and side modes of the slave VCSEL are shown in Figure 6.3 (b). An inter-modal spacing of 1.6 nm or 200 GHz between the dominant and side mode was achieved by biasing the VCSEL

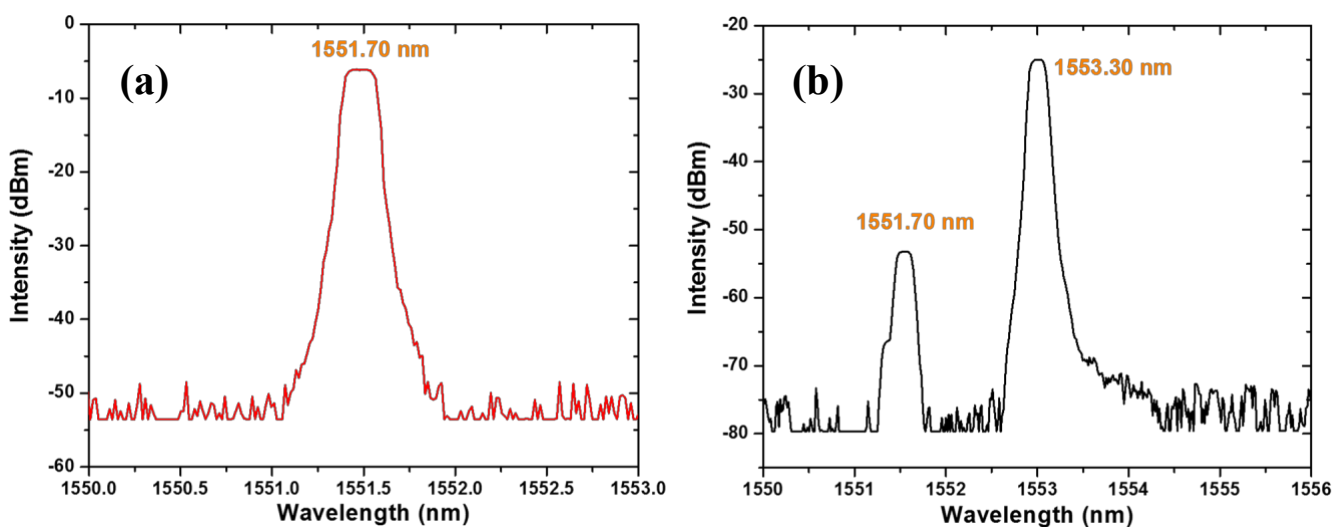


Figure 6.3: Experimentally measured lasing modes of the ThorLabs DFB laser source and VCSEL, respectively. (a) dominant lasing mode of the master ThorLabs DFB laser and (b) dominant and side modes of the slave VCSEL.

at 7.85 mA. The dominant mode is seen to be at 1553.30 nm and side mode at 1551.70 nm. Figure 6.4 illustratively shows the relative propagation delay between the normalized transmitted, wavelength converted and inverted PPS pulse (black line), and the reference electrical PPS pulse (red line). The optical fibre latency results were captured on a 2 GSa/s Agilent sampling oscilloscope. Wavelength conversion, together with data inversion within the 1550 nm transmission window, was achieved after injecting an incoming 12 dBm optical PPS signal from the ThorLabs DFB

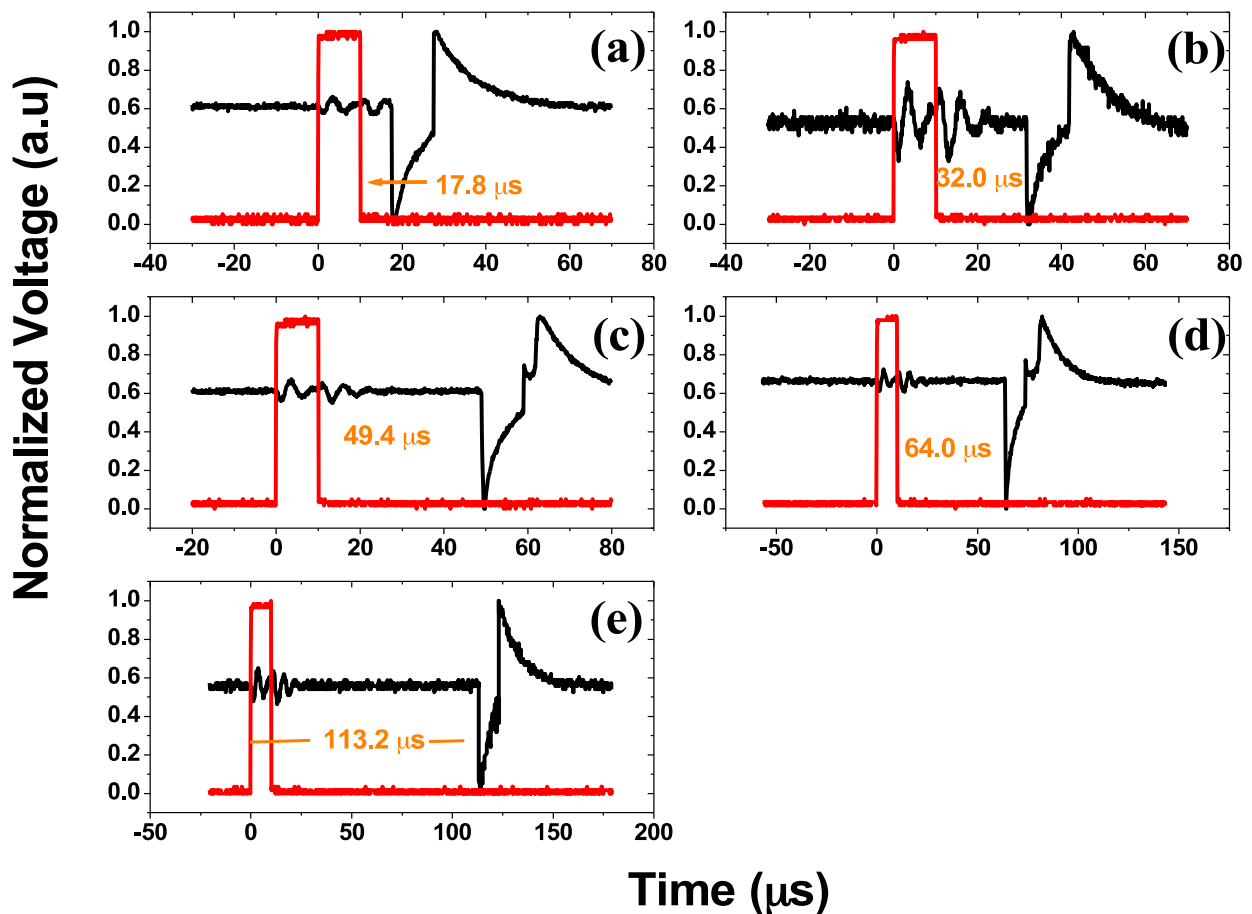


Figure 6.4: Experimental demonstration of optical fibre latency measurements of a transmitted wavelength converted signal along a 3.4 km, (b) 6.4 km, (c) 9.8 km, (d) 12.8 km and (e) 22 km round trip PPS-timing system.

master laser tuned at 1551.70 nm into the wavelength-matched side mode of the slave laser VCSEL at 1551.70 nm. As a result of the high power optical injection, the dominant mode of the VCSEL at 1553.30 nm is suppressed whilst the secondary mode at 1551.70 nm is stimulated and amplified. Subsequently, bit inversion occurs from the 1-level to the 0-level and from the 0-level to the 1-level.

During this process the transmission wavelength is redshifted from 1551.70 nm to 1553.30 nm. A similar result was reported by Boiyo (2017, p. 66-68) in which wavelength conversion was achieved by directly injecting an incoming optical beam into the side mode of a slave VCSEL. Boiyo (2017, p. 66-68) observed a 59.4 dB modal gain after injecting a 10 dB incident beam into the side mode of the slave VCSEL, while suppressing the dominant mode from -28.5 dBm to -40.1 dBm yielding a 11.6 dB extinction ratio. Boiyo (2017, p. 66-68) further reported on an experimentally measured 16 dB extinction ratio following a 15 dBm optical injection into the side mode of the slave VCSEL. After successful wavelength conversion, the transmitted PPS clock signal was translated onto the new carrier wavelength. In Figure 6.4, the inverted PPS signal (black line) lasing at the new 1553.30 nm wavelength is attributed to the high injection power of 12 dBm into the VCSEL side mode. The optical fibre latency measurements are summarized in Table 6.1. The

Table 6.1: Summarized latency results.

Experimental Round Trip Time Delay (μ s)	G.652 Round Trip Transmission Distance (km)	One Way Time Delay (μ s)	G.652 One Way Transmission Distance (km)
17.8	3.4	8.9	1.7
32.0	6.4	16	3.2
49.4	9.8	24.7	4.9
64.0	12.8	32	6.4
113.2	22	56.6	11

transmission delays incurred along the one-way optical dissemination link were obtained by halving the experimentally measured round-trip propagation times. The time delays experimentally measured along the respective fibres are attributed to the material dispersion properties of the optical fibre. From the results given in Figure 6.4 and in Table 6.1 shows that we were able to successfully modulate the slave VCSEL at the remote end without the use of any electrical modulation techniques and

simultaneously accurately measure the fibre latency times. Whitten (1980, p. 2355–2357) reported that the transit time of a light signal along an optical fibre depends on the transmission wavelength and the length of the fibre. Furthermore, the refractive index properties of the optical fibre contribute to propagation delay experienced by the PPS signal due to the dispersion characteristics. Figure 6.5 shows the linear relationship between the optical fibre latency and fibre length. The equation given in Figure 6.5 mathematically describes the linear relationship between the optical transmission time and the fibre length. By inverting the gradient given in the equation,

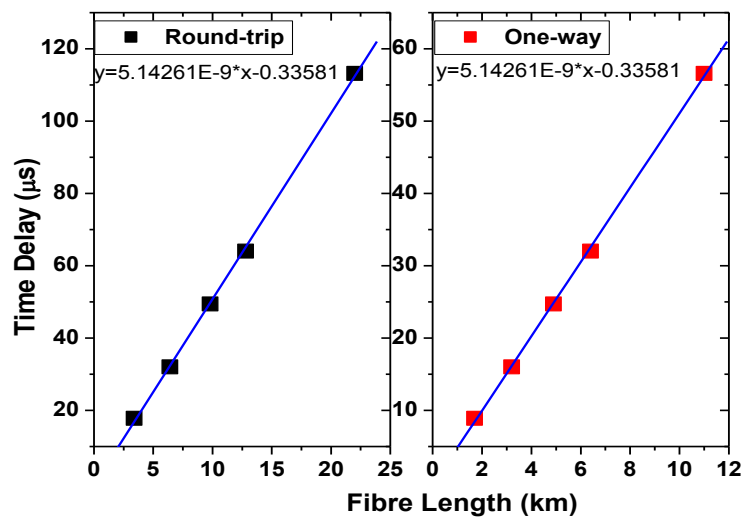


Figure 6.5: Linear relationship between time delay and fibre length for round-trip and one-way transmission.

the velocity of the transmitted PPS signal along the optical fibre was determined. The velocity of the optical PPS signal was found to be 1.944×10^8 m/s, in comparison to the theoretically calculated value of 2.0×10^8 m/s. Furthermore, a 2.8% measurement error was found between the theoretical and experimental values. This implies that the PPS-timing system described in Figure 6.1 demonstrates a high degree of accuracy in measuring the transmission times of the PPS signal along the optical fibre. It is to be remarked that the due to its accuracy and simple measurement procedure, the proposed latency system described in Figure 6.1 may find wide application in next generation astronomical telescope arrays such as the SKA.

6.3: Summary of results

This chapter provides a novel experimental demonstration for measuring the fibre latency based on all-optical wavelength conversion and data inversion within a 1550 nm transmission window using two optical sources and a stable Rb clock. After presenting the experimental demonstration of the all-optical PPS-timing latency systems in Section 6.1, the associated results were provided in Section 6.2. The inter-modal spacing of the VCSEL used in this experiment was experimentally found to be 1.6 nm. As a result of a high power 12 dBm incoming beam injected into the side mode of the slave VCSEL data inversion occurred at the new lasing 1553.30 nm wavelength. As a result of the wavelength conversion technique described in Section 6.2, it was realized that the new 1553.30 nm transmission wavelength could be reused in a DWDM telecommunication network. Furthermore, it was found that the optical latency increased with increasing fibre length. The results presented in Section 6.2 suggest that the PPS latency system is extremely accurate and has particular application in timing measurements. The 200 GHz channel spacing between the dominant and side modes generated within the VCSEL lasing cavity fits into the ITU-T flex-grid system, therefore making the PPS-timing experiment discussed in Section 6.2 applicable for flexible spectrum technology (ITU, 2012, p. 1-7). The benefits of the fibre PPS latency measurement system described in this work are as follows, system complexity and costs are reduced due to the fact that there are no additional electro-optic modulators included into the setup. We experimentally demonstrated the all-optical modulation of the slave VCSEL situated at the remote site. The technique described has a picosecond resolution with a dynamic range of approximately 50 km, with high accuracy and no dead zones. The accuracy displayed by the latency system presented in this chapter is attributed to the stable PPS signal generated by the Rb clock.

CHAPTER 7

PHASE STABILIZATION COMPENSATOR: DESIGN ANALYSIS AND ACTUATOR CONTROL

This chapter outlines the design and operational aspects of a fast switching phase correction system specifically developed for the dissemination of ultra stable and highly accurate clock signals across optical fibre. A simulative study was done in order to show the fibre path length dependence on temperature. This chapter further investigates the possibility of using a VCSEL as an actuator for fibre induced phase noise mitigation. Furthermore, the tunability property of the VCSEL was also investigated.

7.1 Variation of fibre length due to temperature fluctuations

The transmission of high-precision optical frequency signals along fibre networks is becoming extremely common. However, temperature fluctuations and vibrations amount to undesirable optical path length variations. As a result, the phase of disseminated optical signal becomes corrupted. As discussed in Chapter 2, phase coherence is an essential requirement for timing and synchronization for telescope arrays such as the SKA (Muller, Peters & Braxmaier, 2006, p. 401-408; Schilizzi, 2013, p. 10).

The phase variation experienced by the propagating optical signal along the fibre due to temperature fluctuations is mathematically expressed as,

$$\Delta\delta = \frac{\Delta L \times 360^\circ}{\lambda} \quad (7.1)$$

where λ is the transmission wavelength. The change in optical fibre path length, ΔL , seen in Equation 7.1 is given as,

$$\Delta L = L \cdot k \cdot \Delta T \quad (7.2)$$

where L is the fibre length, k is the thermal coefficient of delay and ΔT is the change in temperature (Calhoun, Sydnor & Diener, 2002, p. 1-11).

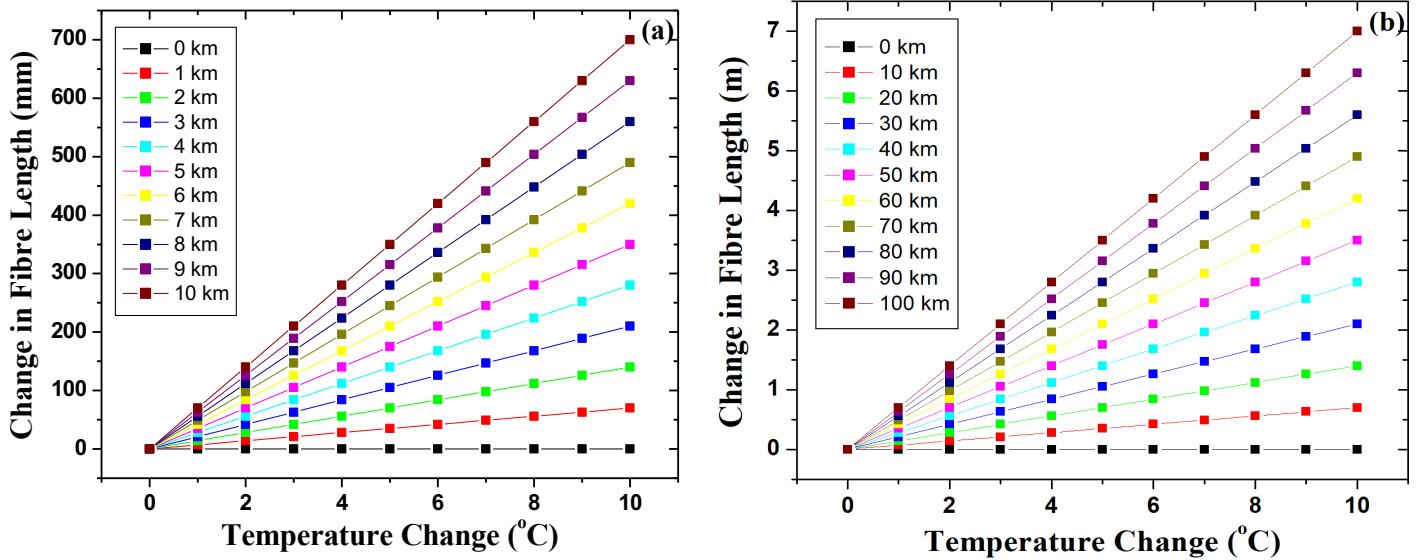


Figure 7.1: Simulated illustration of the rate of change of an optical fibre path length with respect to changing temperature.

A crucial component within a phase noise compensation system intended for time and frequency dissemination is the actuator. An actuator is a device that is used to correct for any fibre induced phase perturbation along the transmission link. Fibre stretcher type actuators modify small sections of the optical path length whereas acousto-optic modulators or phase shifters are inserted within the dissemination link to alter the phase of the transmitted signal.

When designing a stable frequency dissemination system or selecting an actuator for a specific application, such as phase correction, various factors and parameters should be considered. These design parameters may include cost, scalability, geometrical factors, actuator range, stability requirements, drive current, modulation frequency and size. With the assistance of optimization algorithms, computer based modeling techniques can be used with the design or selection process (Gomis-Bellmunt & Campanile, 2010, p. 29-78). Before selecting the phase correction actuator intended for the time and frequency dissemination system described in this work, a series of algorithms were used to model certain events occurring along the optical fibre.

Equation 7.2 was used to model the change in optical fibre path length as a function of temperature variation. The intermediate results of this simulation are shown in Figures 7.1 (a) and (b). The results illustrated in Figures 7.1 (a) and (b) represent the optical fibre path length expansion for transmission distances of 0 km to 10 km and

10 km to 100 km, respectively. The thermal coefficient of delay, k , for optical fibre used in this simulation is $7 \text{ ppm}^\circ\text{C}$ (Calhoun, Sydnor & Diener, 2002, p. 1-11). The intermediate results illustrated in Figure 7.1 suggest that a 2 km deployed fibre experiences a 28 mm optical fibre path length adjustment, whereas a 20 km fibre link experiences a 280 mm change in optical fibre path length, assuming a 2°C temperature change. The physical environmental conditions should be taken into consideration when designing the SKA synchronization and timing system since active phase compensation may be needed for a fibre length as short as 1 km buried approximately 1 m below the surface. At this relatively short path length, a 5°C temperature fluctuation can yield a 35 mm change in the optical transmissions length, as shown in Figure 7.1.

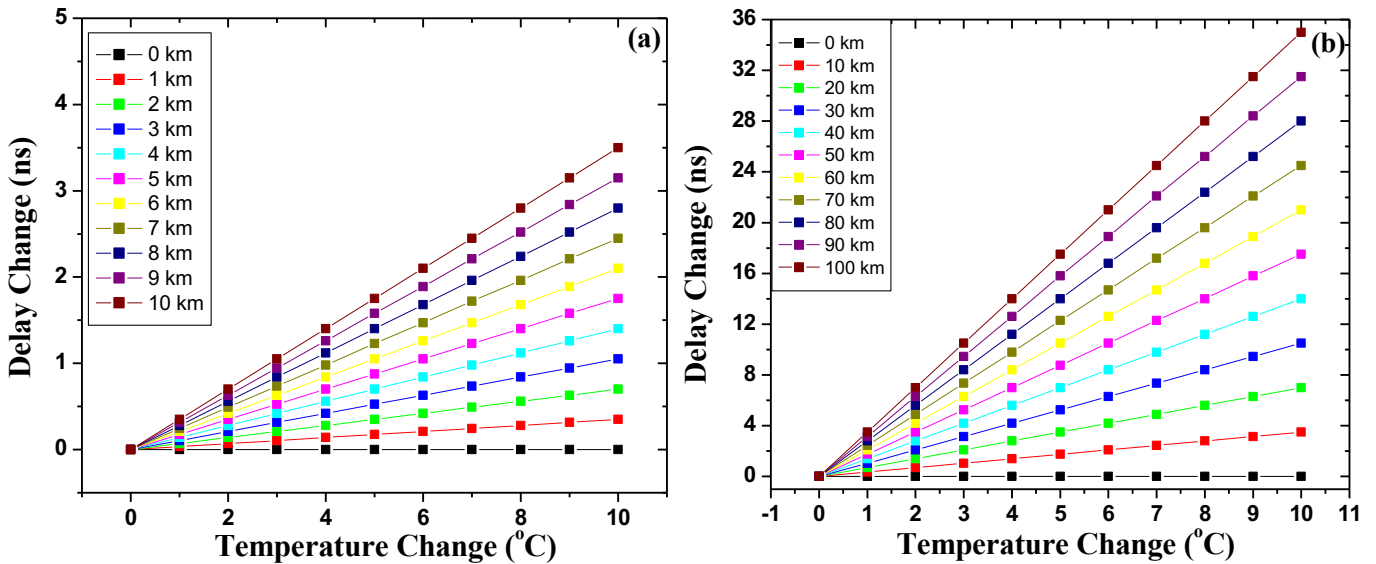


Figure 7.2: Simulated relationship between temperature change and signal propagation delay along single mode fibre.

Collectively, Figures 7.2, 7.3 and 7.4 presents the effect of temperature fluctuation and transmission path length change on propagation delay along the optical fibre.

$$\tau = \frac{\Delta L \times n}{c} \quad (7.3)$$

Equation 7.3 was used to model the time delay as a function of length variation along the transmission path, as seen in Figures 7.3 and 7.4. In Equation 7.3, c is the speed of light and the refractive index, n is 1.5 for single mode fibre.

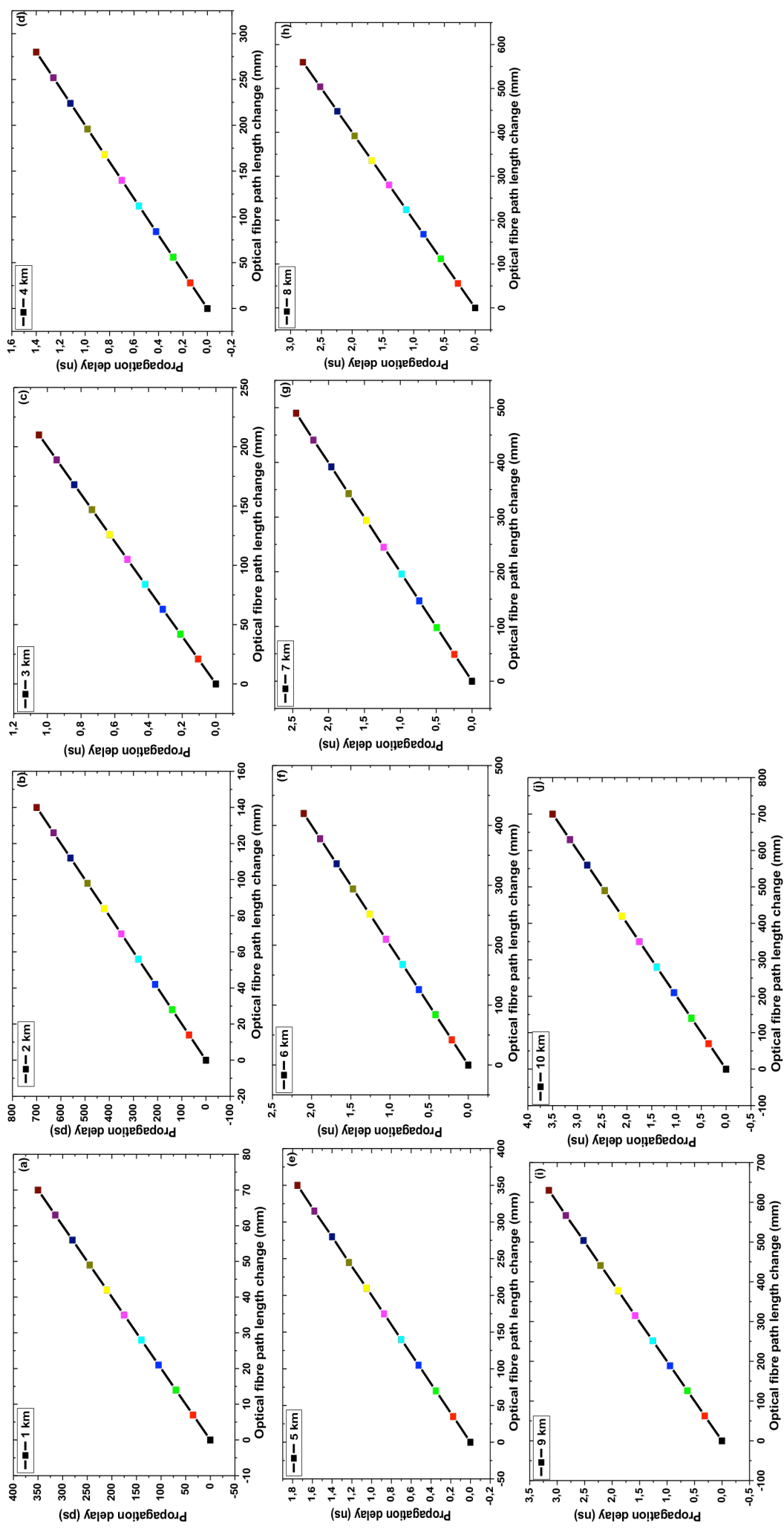


Figure 7.3: Simulated results showing the linear relationship between optical fibre elongation and transmission time delay. The transmission length considered ranges from 1 km to 10 km. The change in optical fibre path length used in this illustration was computed using Equation 7.2, as seen in Figure 7.1.

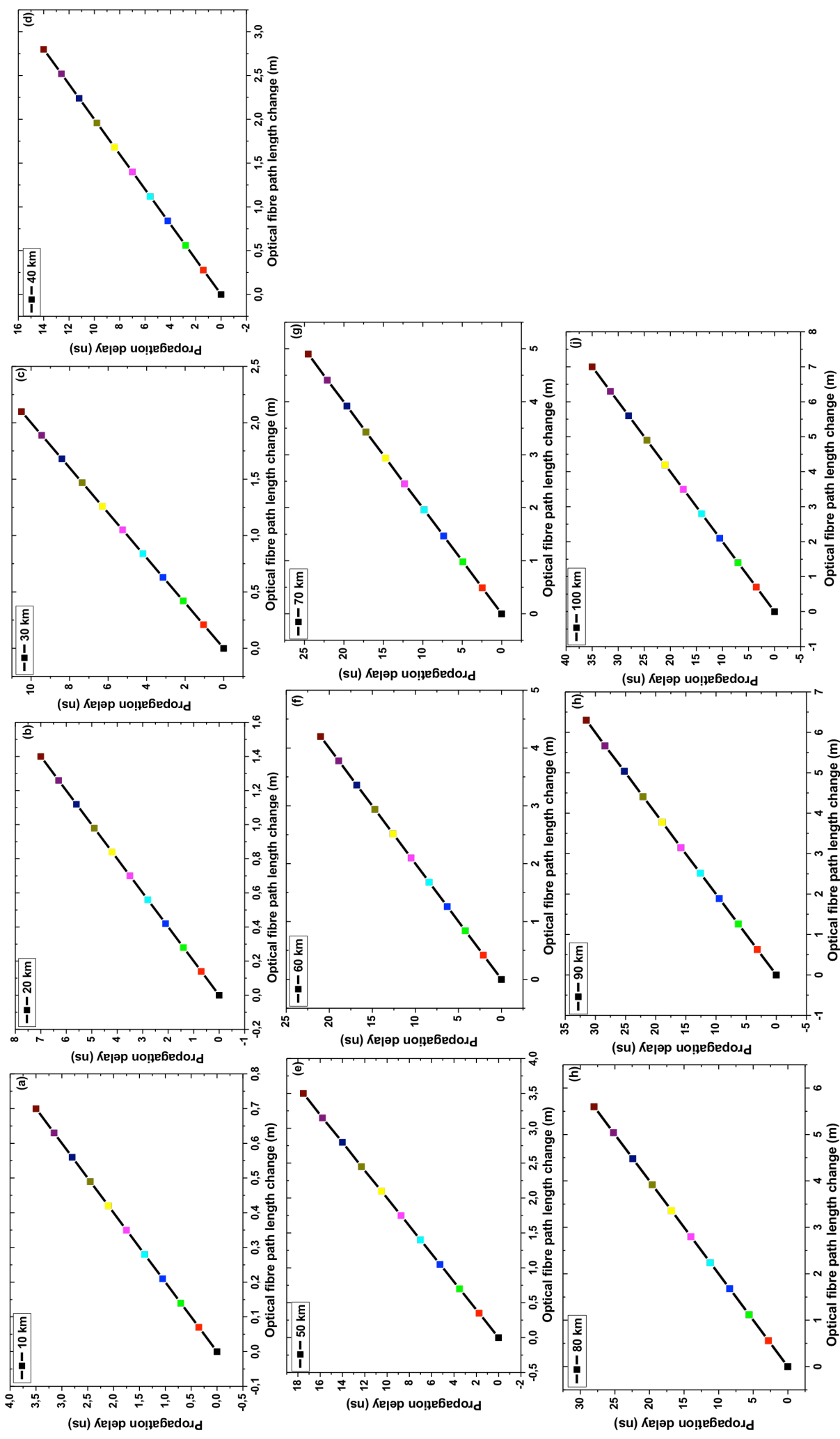


Figure 7.4: Simulated results showing the linear relationship between optical fibre elongation and transmission time delay. The transmission length considered ranges from 10 km to 100 km. The change in optical fibre path lengths used in this illustration was computed using Equation 7.2, as seen in Figure 7.1.

From the simulated results illustrated in Figure 7.3, a 70 mm optical path length change induced by a 5 °C temperature fluctuation along a 2 km fibre corresponds to a 350 ps time delay experienced by the propagating signal. The illustrative results presented in Figures 7.2, 7.3 and 7.4 are useful as it provides a baseline when selecting an actuator with the appropriate phase correction range. For example, approximately ten fibre stretcher type actuators, each with a typical stretch range of 0.14 mm to 6.40 mm (Optiphase), will be required to correct for a 350 ps propagation time delay induced by a 70 mm optical path length change.

The simulative results presented in this section were closely considered and referred to during the development of the VCSEL-based synchronization and timing system described in this study.

7.2 Experimental and simulated demonstration of a 1550 nm VCSEL-actuator tunability range

This section investigates the VCSEL-actuator range based on the intermediate results displayed in Section 7.1. The emission wavelength tunability and biasing characteristic of the 1550 nm VCSEL is illustrated in Figure 7.5. The experimental result in Figure 7.5 (a) represents the wavelength tunability characteristic of the VCSEL. The emission wavelength was adjusted from 1548.67 nm to 1554.06 nm by increasing the bias current from 2 mA to 9 mA. This result shows that by varying biasing current of the VCSEL from 2 mA to 9 mA the entire spectrum is shifted towards higher wavelength region. It further suggests that a wavelength tunability of 5.4 nm was achieved, corresponding to a 437.5 GHz bandwidth. This result is extremely encouraging as it suggests that the proposed VCSEL actuator has the ability to apply a phase correction across a 5.4 nm wavelength bandwidth. However, CD plays an equally important role as well. The output power of the VCSEL emission wavelength was measured as a function varying bias current. The bias current was increased from 0 mA to 9 mA with a threshold current of approximately 1 mA, as seen in the insert in Figure 7.5 (b).

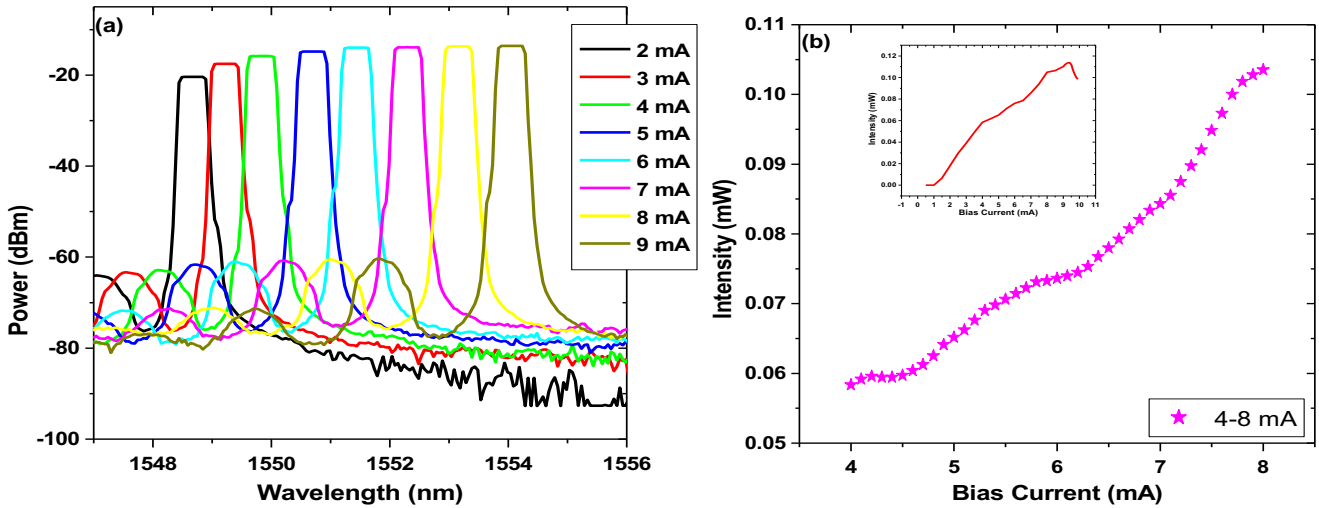


Figure 7.5: Experimental demonstration showing the (a) wavelength tunability property and (b) biasing characteristic of the VCSEL. The insert in (b) shows the transfer curve with varying bias from 0 mA to 9.8 mA.

A maximum threshold current rating of 4 mA is specified for the VCSEL. Figure 7.5 (b) shows the bias characteristic curve from 4 mA to 8 mA. Collectively, the results illustrated in Figure 7.5 were used in modelling the VCSEL phase correction factor. The idea behind the phase correction technique using a VCSEL as an actuator is based on fundamental physics concepts related to optical fibre transmission theory as

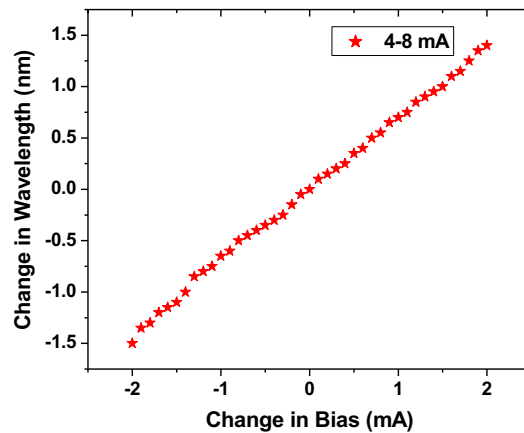


Figure 7.6: Experimental demonstration of the change in emission wavelength as a function of varying VCSEL bias current.

well as the property of the VCSEL laser source. The approach adopted in the time and frequency system presented in this work makes use of the inherent chromatic dispersion properties of the fibre together with the wavelength tunability property of the VCSEL seen in Figure 7.5 (a).

Figure 7.6 experimentally shows the relationship between the change in VCSEL bias current and emission wavelength. Consider the bias characterization curve given in Figure 7.5 (b). The ideal operational bias point of the VCSEL is between the threshold and rollover currents, along the linear region as shown in Figure 7.5 (b). For demonstrational purposes, a 6 mA bias point was selected. When operating a VCSEL at this bias value, a + 0.1 mA change in the bias current corresponds to a 0.1 nm wavelength shift, whereas a + 2 mA bias change results in a 1.4 nm wavelength shift, as seen in Figure 7.6. Conversely, a – 0.1 mA change in the bias current corresponds to a 0.05 nm wavelength shift whereas a – 2 mA bias change results in a 1.5 nm wavelength shift. Here the shift, is towards the shorter wavelength region. The plus sign signifies a bias change in the positive x direction while the minus sign denotes a shift in bias towards the negative x direction. Figure 7.6 further suggests that the VCSEL has an approximate 4 nm tunability range around the 6 mA bias point. Figure 7.7 illustratively shows how the wavelength of a 1550 nm VCSEL is red-shifted during modulation, as the bias current is increased.

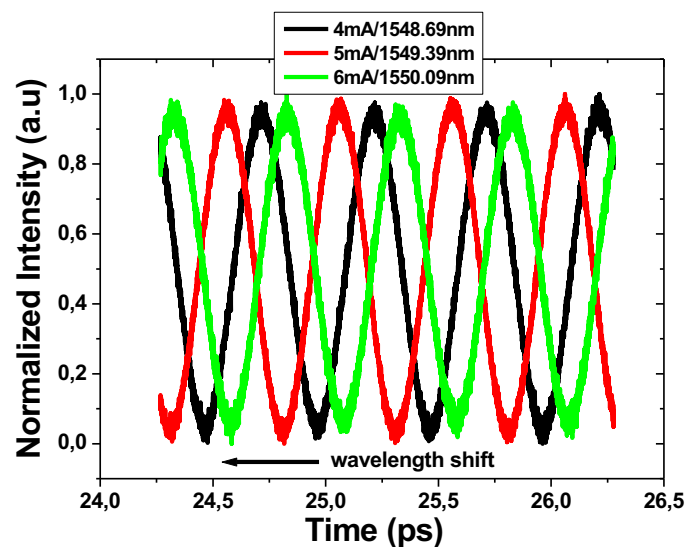


Figure 7.7: Experimental illustration of the VCSEL wavelength shift as a function of bias current.

The shifting of the clock signal along the optical fibre as seen in Figure 7.7 is a result of the inherent chromatic dispersion properties of the fibre. Collectively, Figures 7.6 and 7.7 clearly illustrate the VCSEL's ability to apply a forward or backward phase error correction with respect to varying bias current. Equation 7.4 (Tratnik, Lemut,

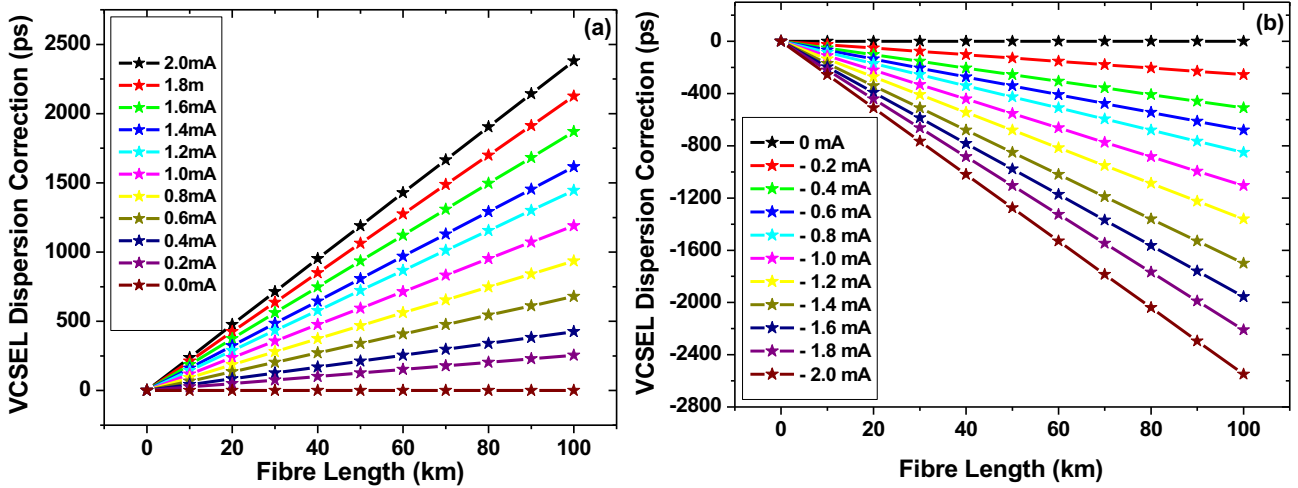


Figure 7.8: Simulated VCSEL dispersion correction factor as a function of fibre length. (a) represents the VCSEL phase correction for forward bias shift and (b) illustrates VCSEL phase correction for backward bias shift.

Dragonja, Batagelj & Vidmar, 2013, p. 162-165) together with Figures 7.5 and 7.6 was used to model the VCSEL dispersion correction factor along a single mode fibre.

$$\Delta\tau = L \cdot D \cdot \Delta\lambda \quad (7.4)$$

$D = 17$ ps/nm·km for standard single mode fibre. The simulated results illustratively shown in Figure 7.7, represent the VCSEL dispersion correction factor as a function of optical fibre path length. The findings in Figure 7.8 suggest, that for a 100 km optical fibre transmission link, the VCSEL is able to apply a 2380 ps or 2.38 ns phase correction. This corresponds to a 1.40 nm wavelength shift towards the longer wavelength region, as seen in Figure 7.8 (a). Furthermore Figure 7.8 (b) infers that the VCSEL actuator can apply a -2550 ps or -2.55 ns (backwards) phase error correction along a 100 km fibre link, corresponding to a 1.50 nm shift towards the shorter wavelengths region. The experimental and simulated results shown in Figures 7.6 and 7.8 suggest that the VCSEL described in Figure 7.5 has a total actuator range of approximately 5000 ps or 5 ns. This result further implies that the VCSEL is capable or better suited to applying compensation for any changes along optical fibre lengths ranging from 1 km to 10 km, as seen in both Figures 7.3 and 7.8.

7.3 Optical clock tone stability optimization

A key requirement for the SKA is that the entire synthesis array remains phase coherent during an astronomical measurement. Therefore, the maximum tolerable rms phase drift of a clock signal is 11° , which corresponds to a 2 % degradation in the

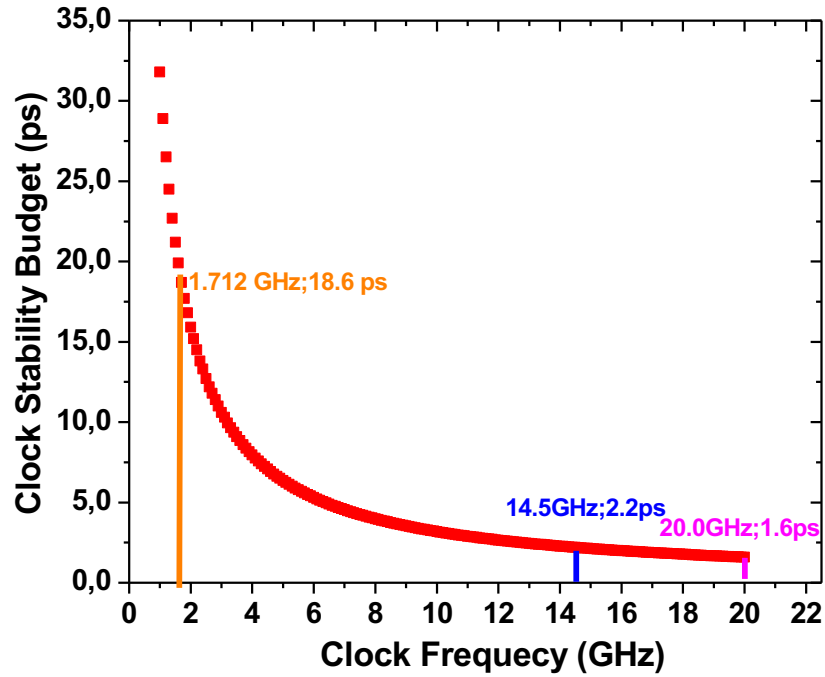


Figure 7.9: (a) illustrates the maximum allowable clock instability as function of observation frequency. (b) VCSEL dispersion correction factor.

telescope sensitivity (Schilizzi, 2013, p. 25). The requirement established for the phase stability of the disseminated frequency reference or local clock signal is closely associated to the telescopic observation frequency (Dewdney, 2011, p. 63).

The 11° phase error condition referred to in the above paragraph together with Equation 7.5 was used to compute the result shown in Figure 7.9.

$$\tau = \frac{\phi}{360^\circ \times f} \quad (7.5)$$

Figure 7.9 shows the modelled, maximum clock stability requirements as a function of observational frequency. For the desired SKA observational frequencies of 1.712 GHz, 14.5 GHz and 20 GHz stringent clock stability requirements of 18.6 ps, 2.2 ps and 1.6 ps are needed, respectively. This implies that for astronomical observations within the SKA mid frequency band, the maximum allowable phase error will be 18.6 ps at 1.712 GHz. Furthermore, for astronomical observations in the high frequency band a 1.6 ps maximum phase drift at 20 GHz will be allowed. From the computational results given in Figures 7.8 and 7.9 it is evident that the VCSEL

characterized in Figure 7.5 is capable of applying the necessary phase correction in order to maintain the stringent phase stability requirements.

7.4 Summary

This chapter provides a detailed analysis of the design and control aspects of a fast phase switching 10 Gbps VCSEL actuator. Section 7.1 investigates the change in optical fibre path length as a function of temperature fluctuation. The results given in Figures 7.1 to 7.4 shows that a 2° change in temperature induces a 28 mm and 280 mm change in the optical fibre path length along a 2 km and 20 km transmission distance. The computational results further show that a 70 mm variation in optical fibre path length induces a 350 ps propagation time delay.

In Section 7.2 the bias current of the VCSEL was adjusted in order to experimentally illustrate the tunability property of the VCSEL. Here the results suggest that a + 0.1 mA and + 2 mA change in the bias current corresponds to a 0.1 nm and a 1.4 nm wavelength shift, respectively. The experimental results illustrated in Figures 7.5 and 7.7 form the basis of the approach used to realize phase compensation along the optical fibre using the proposed VCSEL actuator. The experimental and simulated results presented in this section suggest that the VCSEL has a tunability range of approximately 5000 ps or 5 ns. CD plays an important catalytic role during the shifting of the optical signal.

In the final section of this chapter the clock stability budget is discussed. The simulated results illustrated in figure 7.9 highlights the stringent clock tone stability requirement at the respectively SKA observational frequencies. The next chapter presents the experimental results pertaining to how the phase stabilization system within an optical fibre network will be implemented.

CHAPTER 8

IMPLEMENTATION OF THE PHASE STABILIZATION COMPENSATOR

In Chapter 7, a series of equations were used to model various aspects pertaining to the design and use of a VCSEL phase correction actuator. The results illustrated in Chapter 7, provides the basis for the discussion presented in this chapter. This chapter presents preliminary experimental results performed on the VCSEL phase actuator built into the time and frequency dissemination system. This chapter begins with a brief presentation of an interesting feature of the VCSEL phase correction actuator built into the frequency dissemination system. Sections 8.2 and 8.3 investigate the error signal generated for feedback control of the VCSEL phase correction actuator. Finally, Section 8.4 provides a proof of concept in which a DFB laser acts as a phase compensator along a round-trip time and frequency dissemination system.

8.1 Experimental demonstration of the VCSEL-actuator tunability

The experimental phase shift measurements of a 1310 nm modulated VCSEL along an optical fibre transmission link, as seen on a wide band Infiniium oscilloscope, is

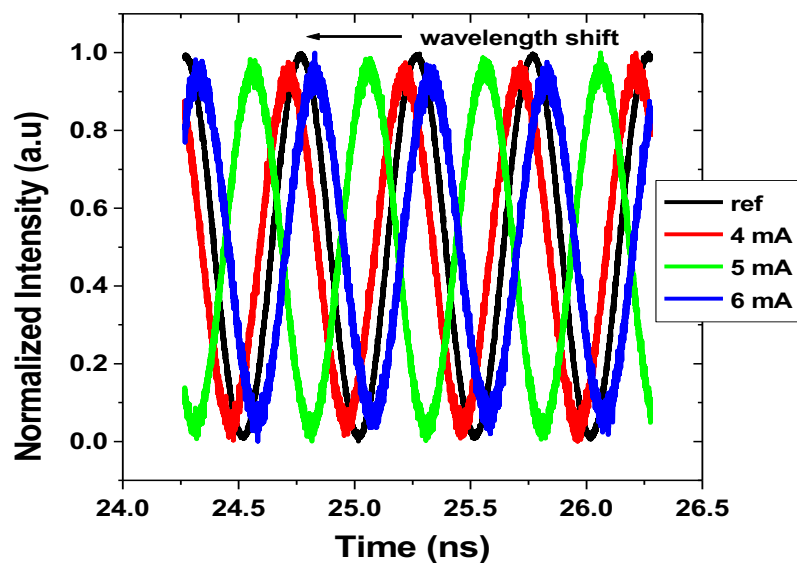


Figure 8.1: Experimental illustration of the phase shift of a sinusoidal modulated 1310 nm VCSEL output signal.

shown in Figure 8.1. A 2 GHz clock signal generated from the R&S SMB 100A was used to modulate the VCSEL laser source. The phase shifts experienced by the transmitted signal were measured as a function of changing bias current relative to a 150 mV reference signal, as seen in Figure 8.1. It is evident that a phase differences of 63.71 ps, 223.0 ps and 453.35 ps were measured with respect to the reference at 4 mA, 5 mA and 6 mA respectively. This corresponds to a phase shift of 45.87° , 160.56° and 326.41° , respectively. It is to be remarked that the bias current was changed by manually controlling a dial on a laser diode controller. Wavelength tuning and chromatic dispersion provokes the shifting phenomenon along the fibre as seen in Figure 8.1. The results presented in Figure 8.1 experimentally confirms that the VCSEL phase compensator will function as required, whereby the necessary phase compensation may be applied by the introduction of a specific feedback voltage into the laser diode controller (Fan, Wu, Lee & Grodzinski, 1994, p. 1409-1410).

8.2 Error signal analysis in the electrical domain

For the first time at NMU, this section presents an all-electrical experimental demonstration of error signal generation using a frequency mixing technique. In a closed loop system, if no input signal is applied the error signal voltage at the output of the frequency mixer will be zero. The two signals referred to in this text are the transmitted and reference signals. Here the frequency mixer assumes the duty of the phase comparator. When two input signals are applied to the frequency mixer within the closed loop system, such as a phase lock loop (PLL), an error signal is subsequently generated. The resultant error signal voltage is proportional to the phase difference between the input signals. After lowpass filtering, the error signal is used for feedback control of the phase of the actuator. The error voltage fluctuates in a manner that reduces the phase difference between the two signals (Morgan, 2003, p. 3). Initially, when the two signals are out of phase, the closed loop system is considered to be out of lock. In such a condition the error signal will pull the transmitted signal towards the reference signal until such time when the loop is locked and the error voltage is reduced (Analog Devices, 2009, p. 1-10; Poole).

8.2.1 Experimental demonstration of a phase error signal generated in the electrical domain

The experimental demonstration for generating and measuring the error voltage as a function incremental phase change is illustrated in the experimental setup shown in

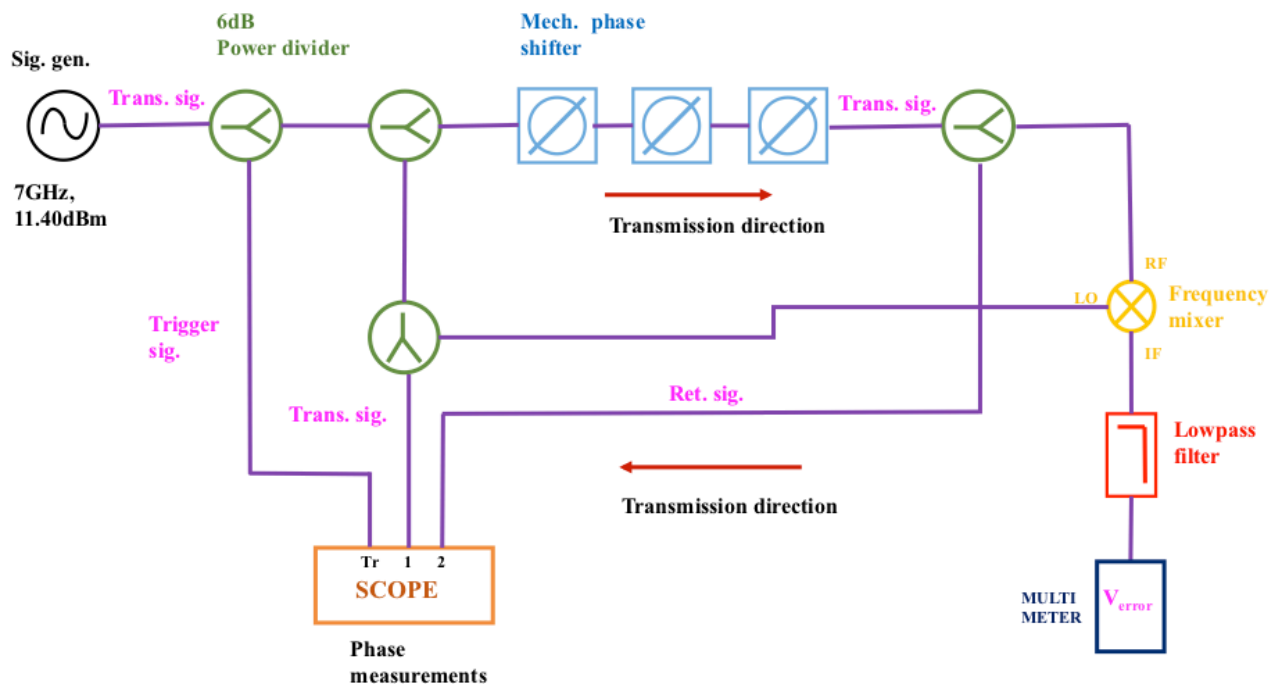


Figure 8.2: Experimental setup of the all-electrical frequency transfer system used for the error signal analysis.

Figure 8.2. At the transmission end, a 7 GHz clock signal with a 11.40 dBm output power was emitted from an R&S SMB 100A signal generator. A series of resistive power dividers, with an insertion loss of 6 dB was used to split the RF signal into two and redirect it along the respective transmission paths. A portion of the divided 7 GHz sinusoidal signal emerging from the first resistive power divider placed directly after the signal generator was used to trigger the Infiniium wide band oscilloscope, enabling the waveform to be displayed on the scope. Three mechanical phase shifters, each with an insertion loss 0.8 dB and a 0.5° per turn per GHz resolution, were used to adjust the phase to the disseminated clock signal. The phase shift was applied by manually turning the phase adjustment screw. It is to be remarked that the mechanical phase shifters were used in order to emulate the fibre induced propagation delay. A resistive power divider located directly after the mechanical phase shifters was used to divide and redirect the shifted RF signal towards the oscilloscope in order to view and measure the phase shift in real time, relative to the un-shifted reference signal, as

seen in Figure 8.2. To generate the error signal, a frequency mixer with a typical conversion loss of 6 dB was used to down convert the two signals. This operation was realized by mixing down the phase shifted and reference RF signals. Thereafter, a lowpass filter (LPF) with a DC-48 MHz frequency bandwidth was used to filter out the baseband error signal. The resultant error signal voltage after the LPF was measured as a function of phase change, using a voltmeter. The analysis of the experimental error signal results will be presented and discussed in the following section.

8.2.2 Error signal results as a function of time delay

Before presenting the experimental error signal results, this section begins by presenting the intermediate mechanical phase shifter and frequency mixer characterization results.

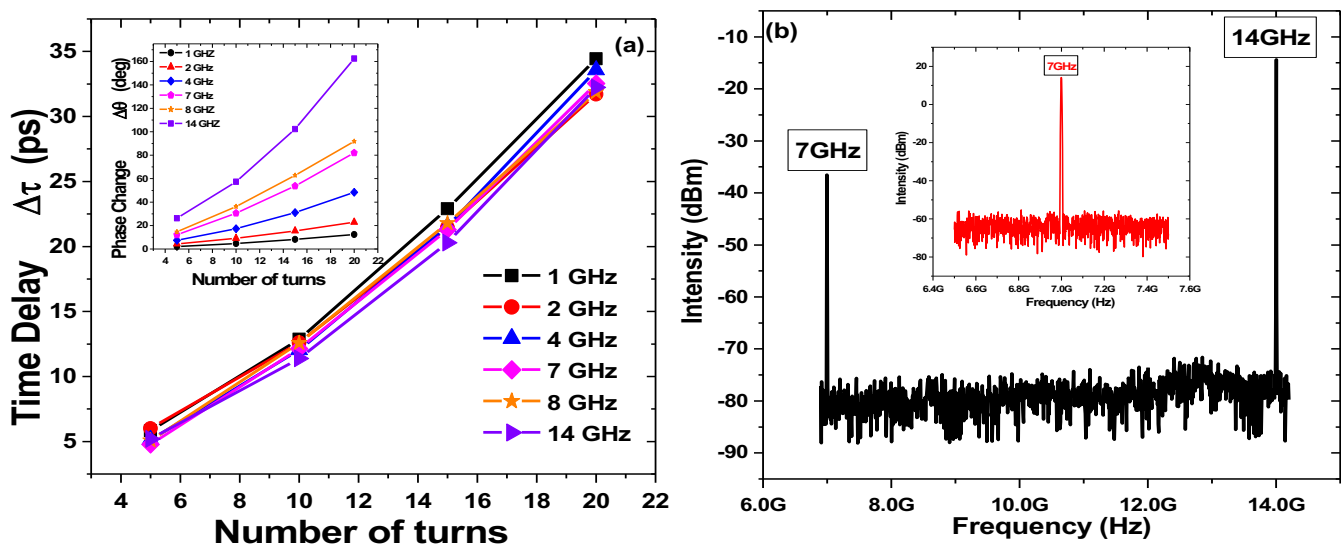


Figure 8.3: (a) experimental incremental phase shift calibration and (b) experimental demonstration of RF mixing process. The insert in Figure 8.3 (a) illustrates the phase change in degrees.

Figure 8.3 (a) shows incremental phase shift versus the number to turn applied to the phase adjustment screw of the Aeroflex Weinschel mechanical phase shifter. The measurements were conducted at 1 GHz, 2 GHz, 4 GHz, 8 GHz and 14 GHz, respectively. The phase, in picoseconds, between a reference and the shifted clock signal was measured using the marker functionality on the Infiniium wide band oscilloscope. With an increase in the number of turns to the phase adjustment screw, a clear shift in the phase of the clock signal was seen. Figure 8.3 (a) further indicates

that the phase shift increases with increasing clock modulation frequency. Figure 8.3 (b) illustratively shows the experimental frequency mixing results. A pair of 7 GHz RF clock signal were mixed resulting in the frequency spectrum given in Figure 8.3 (b). The resultant output frequency generated by the mixer given in Figure 8.3 (b) is mathematically described using Equation 8.1 (Marki, F & Marki, C, 2010, p. 3).

$$f_{out} = f_{in1} \pm f_{in2} \quad (8.1)$$

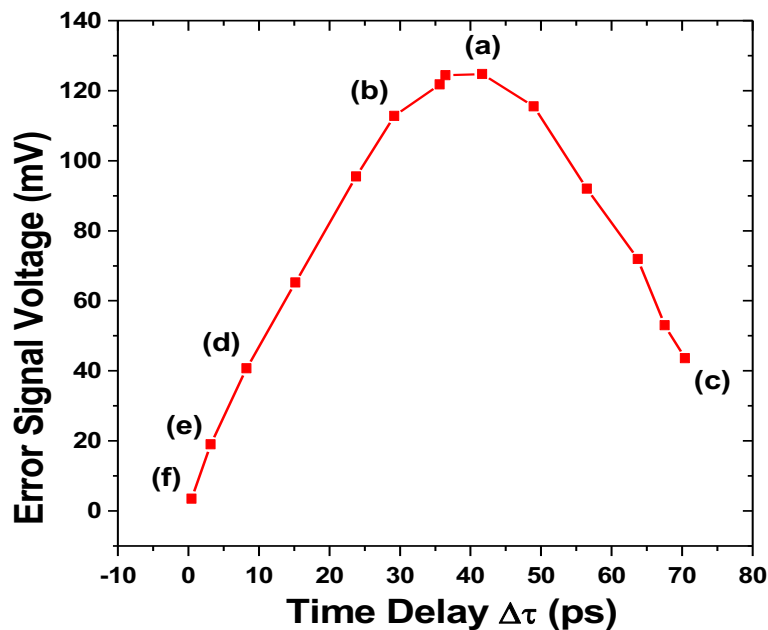


Figure 8.4: Experimental demonstration of the error signal generated as described in figure 8.2.

The output voltage of the error signal generated during the mixing process measured as a function of relative phase shift is presented in Figure 8.4. The error signal voltage was measured using a Fluke multi-meter immediately after the LPF, as seen in Figure 8.2. Furthermore, the applied phase shift results between the shifted (red waveform) signal and reference signal (black waveform) are reported in Figure 8.5. The illustrative results presented in Figures 8.4 and 8.5 shows that error voltages of 124.70 mV and 3.50 mV were measured at applied phase shifts of 41.66 ps and 0.46 ps, respectively. This result further suggests that the error signal generated during the mixing operation is maximized when the phase difference between the shifted and reference signal is 41.66 ps, corresponding to 124.70 mV. Figures 8.4 and 8.5 further reveal that the error voltage tends to zero when the relative phase difference between the shifted (red waveform) and reference (black waveform) is approximately zero.

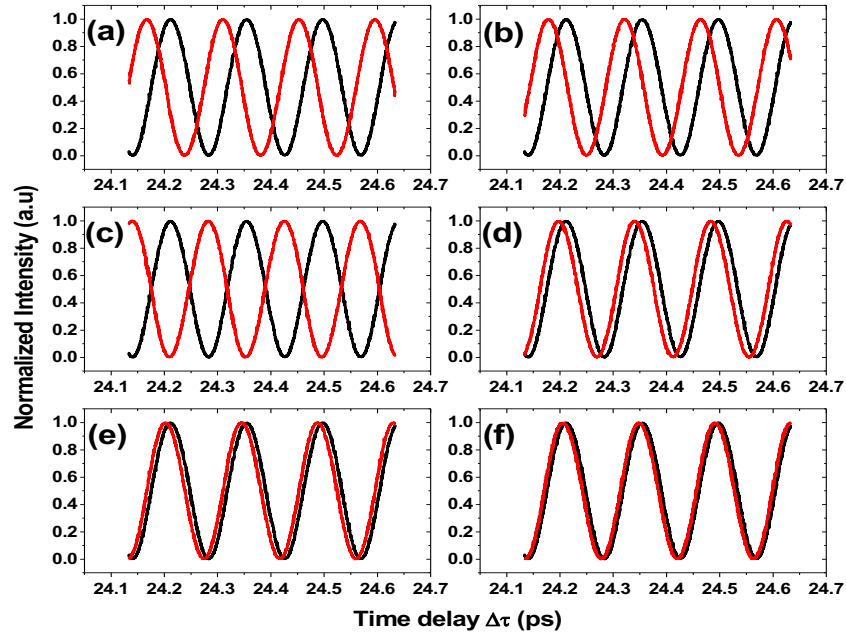


Figure 8.5: Experimental demonstration of the phase shift relative to a reference (black waveform) signal.

This shows that the two signals are now in-phase implying, that the system will be in a locked state. In this section, an error signal calibration curve as a function of phase shift was discussed. The following section further investigates the error signal behaviour. The experimental configuration used to generate the error signal is similar to the setup described in Section 8.2.1 and illustrated Figure 8.2. However, the only notable difference here is the inclusion of the optical transmission components.

8.3 Experimental error signal analysis along a 1310 nm VCSEL optical transmission link

Section 8.3 describes a technique for generating an error signal intended for feedback control along an optical transmission link. For the first time ever at NMU, a 1310 nm VCSEL clock signal was used during the frequency mixing process. The error voltage performance, as a function of changing bias was investigated.

8.3.1 Experimental demonstration of error signal generation used for feedback control of a 1310 nm VCSEL

The optical fibre based dissemination system used for error signal behavioural analysis is shown in Figure 8.6. In the frequency distribution setup given in Figure 8.6, an R&S SMB 100A waveform generator, operating between 100 kHz and

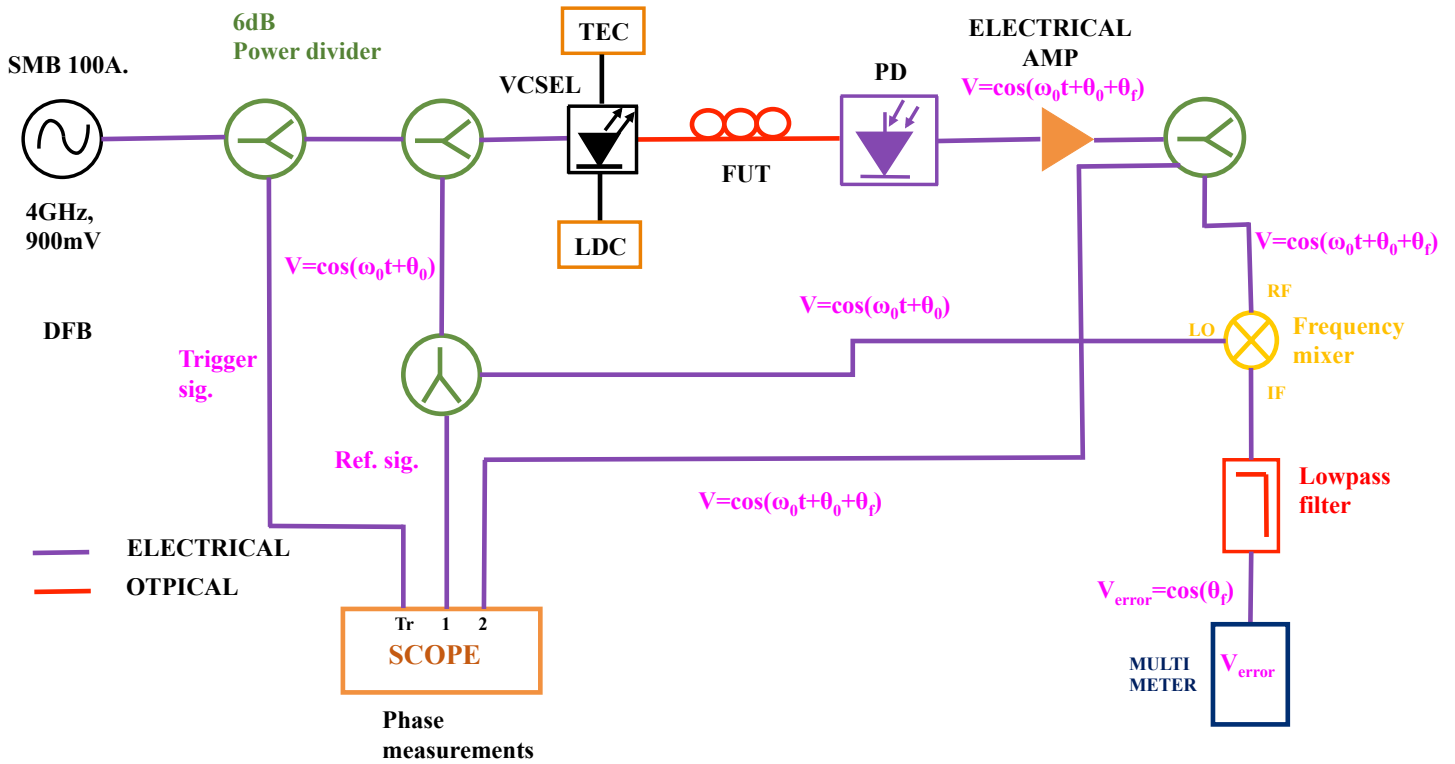


Figure 8.6: Experimental configuration used for error voltage analysis based on an optical fibre frequency dissemination scheme.

20 GHz, was used to generate a 4 GHz clock signal with an output power of 900 mV. A temperature controlled VCSEL with a lasing wavelength of 1306.89 nm at 7 mA, was directly modulated with the 4 GHz RF clock signal using the R&S SMB 100A waveform generator. A series of 6 dB power dividers were used to split and redirect the electrical RF signal as seen in Figure 8.6. The LDC and TEC were used to vary the applied bias current and control the temperature of the VCSEL, respectively. In this experiment, the VCSEL temperature was maintained at 25° C corresponding to a 10 kΩ thermistor resistance setting. The optical clock signal was transported from the transmitter to the receiver via 26 km G.655 single mode fibre. At the receiver end, the power of the resultant electrical signal after the photodiode (PD) was amplified using a wide band electrical amplifier with a typical gain of 27 dB. To generate the error signal, the resultant electrical signal after the PD was mixed with the reference signal and down converted using a frequency mixer together with a LPF, as seen in Figure 8.6. The frequency mixer has a typical conversion loss of 6 dB, while the 50 Ω LPF only allows frequency signals within the DC to 22 MHz range to pass through. The resultant DC error signal voltage, V_{error} , was monitored and measured as a function of bias change using a Fluke multimeter, as illustrated in Figure 8.6. As seen in the

experimental description given in Figure 8.6, the relative phase shift between the stable reference RF signal and the transmitted sinusoidal waveform was measured on the Infiniium oscilloscope with a specified 20 GHz bandwidth in the time domain.

8.3.2 Down converted error signal results

The error voltage measurements as a function of bias current and optical signal phase shift are shown in Figure 8.7 (a) and (b), respectively.

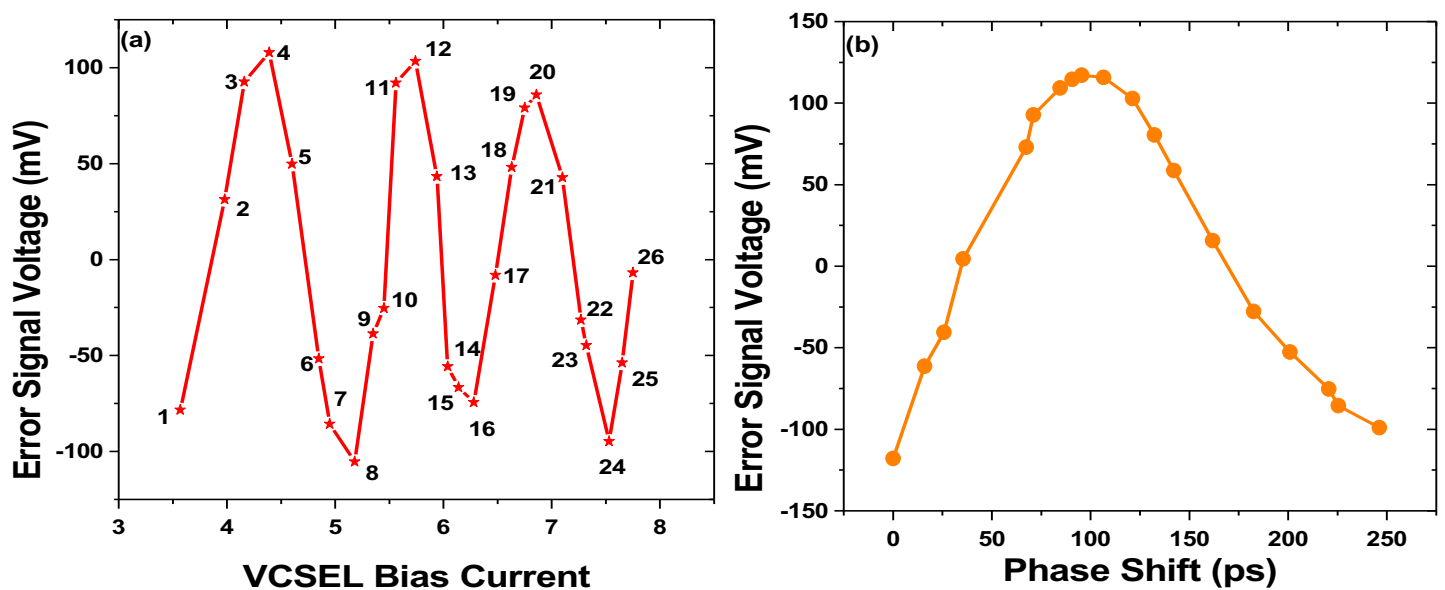


Figure 8.7: Error voltage measurements as a function of (a) varying bias current and (b) phase shift.

The error voltage illustratively shown in Figure 8.7 (a) was measured whilst varying the bias current using a stepwise approach from 3.57 mA to 7.75 mA. The results given in Figure 8.7 (a) was generated by mixing down, $V = \cos(\omega_0 t + \theta_0)$ and $V = \cos(\omega_0 t + \theta_0 + \theta_f)$ to produce the error signal $V_{\text{error}} = \cos(\theta_f)$, as illustrated in Figure 8.6. The error voltage data points numbered 1 to 26 in Figure 8.7 (a) corresponds to the relative phase shift experienced by the transmitted optical RF clock signal along the fibre. The corresponding phase shifts can be seen in Figures 8.8 and 8.9. The phase fluctuations seen in Figures 8.8 and 8.9 were realized by varying the bias current on the LDC and the inherent chromatic dispersion properties of the fibre. As expected, the error signal shown in Figure 8.7 (a), displays the sinusoidal behaviour related to the frequency mixing process. Figure 8.7 (b) presents the error voltage measurements as function phase shift. The results given in Figure 8.7 (a) are best explained using Figures 8.8 and 8.9.

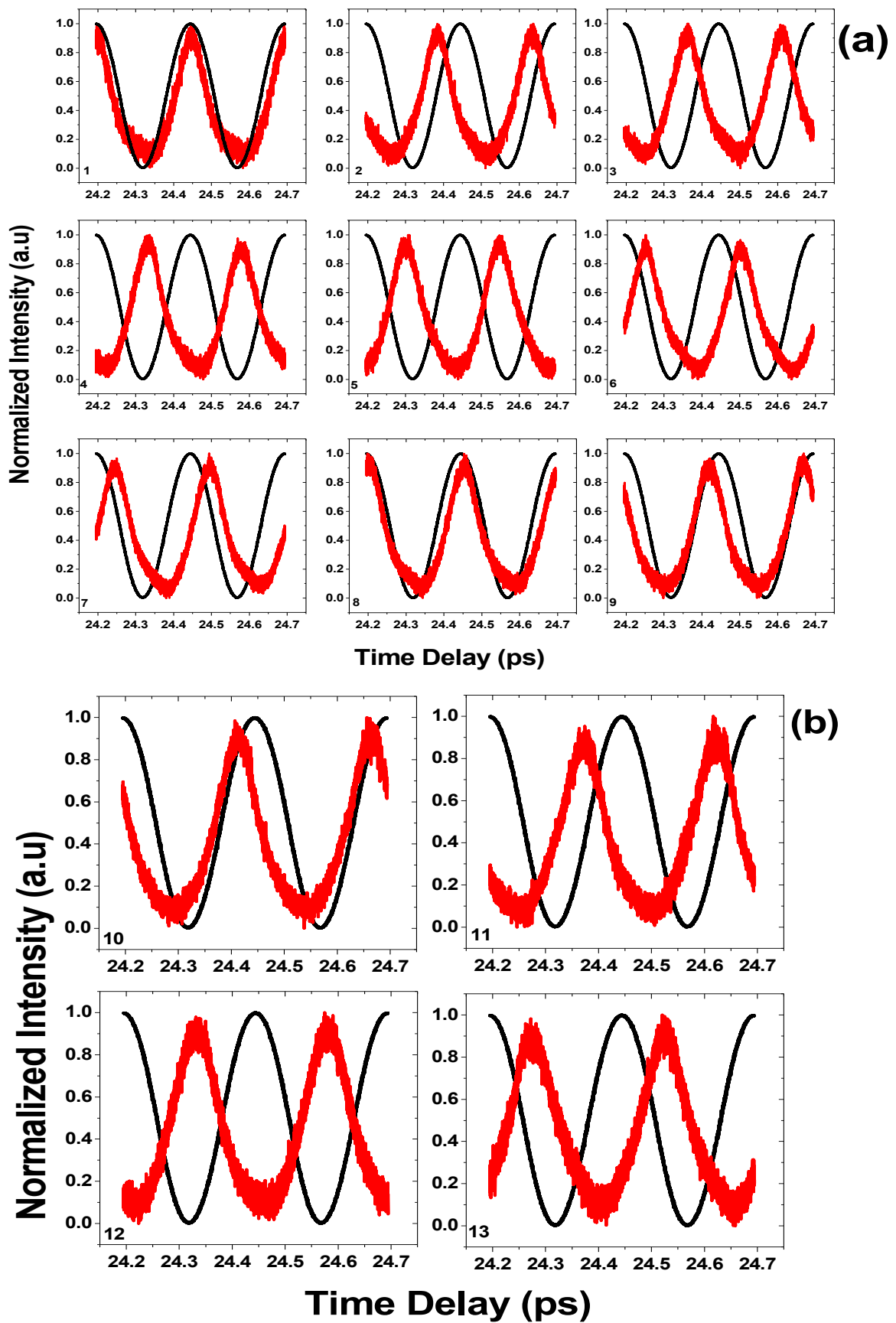


Figure 8.8: Experimental demonstration of the relative phase shift with varying VCSEL bias current.

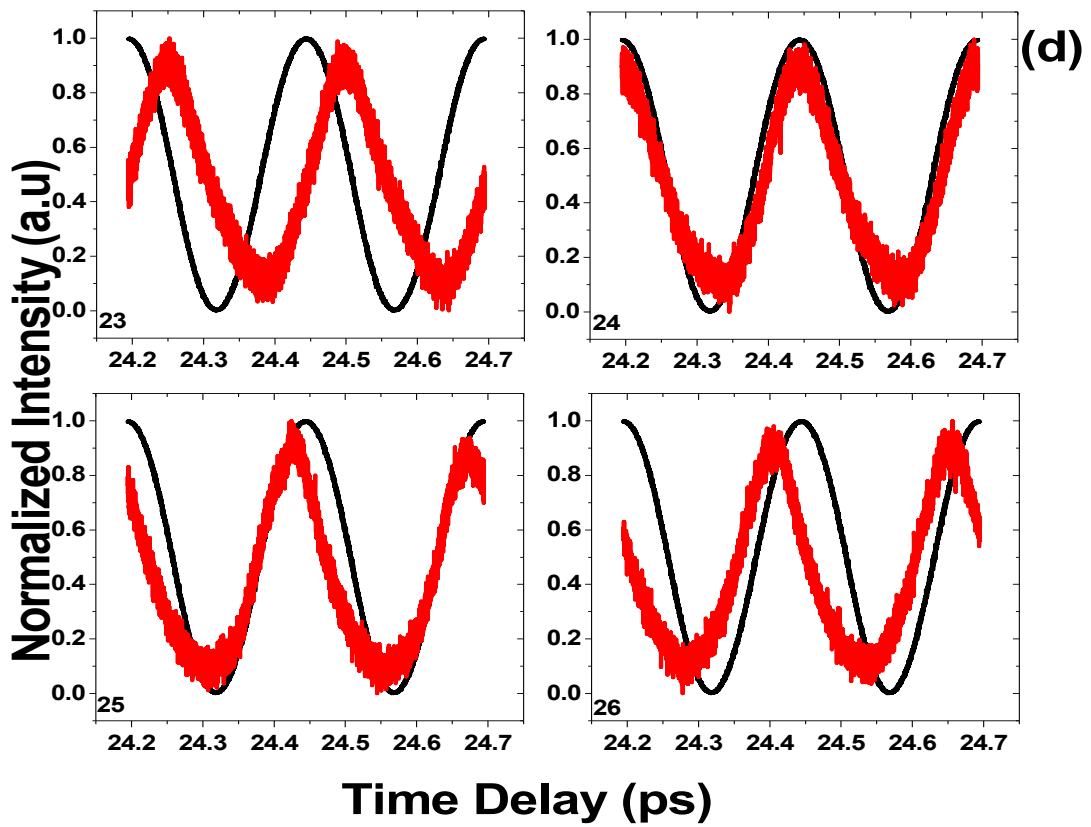
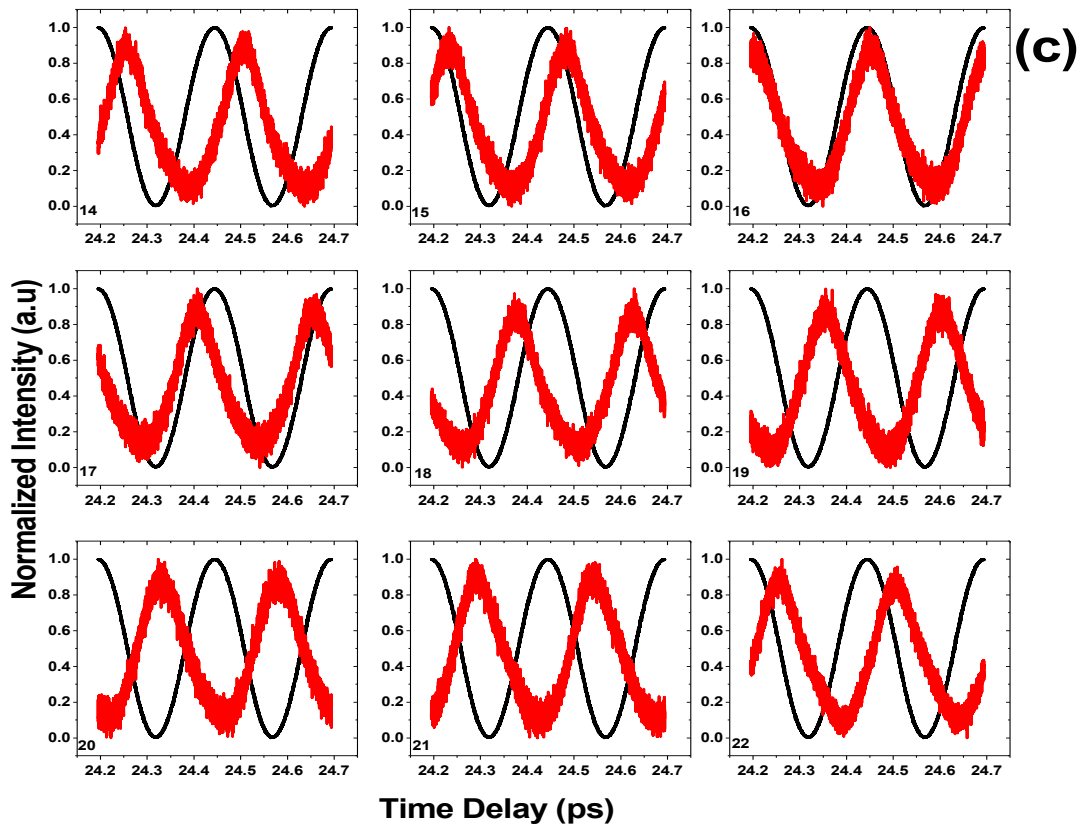


Figure 8.9: Experimental demonstration of the relative phase shift with varying VCSEL bias current.

The error signal appears to be minimized at points 1, 8, 16 and 24, corresponding to -78.3 mV, -105.3 mV, -74.4 mV and -94.7 mV, respectively. These error voltage measurements correspond to the illustrative phase measurements seen in Figures 8.8 (a1, a8), 8.9 (c16) and 8.9 (d24). This result further suggests that the error voltage approaches a minima when the reference and transmitted signals are in phase. For a feedback control system, this result implies that the transmitted clock signal will be locked to the reference sinusoidal waveform at these specific error voltage values. The result in Figure 8.7 (b) illustratively shows that the error signal reaches a minima at -117.9 mV when the measured phase difference between the two signals is 0 ps. Conversely, the results presented in Section 8.3.2 show that the error signal is maximized when the two signals are approximately 180° out of phase, as seen in Figures 8.7, 8.8 and 8.9. From Figure 8.7 (b), it is clear that an error voltage of 117.1 mV was reported corresponding to a measured phase difference of 95.57 ps.

The result presented in this section supports the concept of using the light emitted from a VCSEL laser source as a carrier signal for clock tone transmission along the fibre. It further suggests that the recovered electrical signal can be used to successfully generate an error signal for feedback control of the VCSEL actuator.

8.4 Towards the development of a time and frequency dissemination system using a VCSEL actuator

This section presents a proof of principle towards developing a timing system in which a directly modulated VCSEL is used as an optical source, as well as a phase correction actuator. In the time and frequency dissemination experiment described in this section, the required phase error correction was applied by manually tuning the emission wavelength of a directly modulated DFB laser. There are two reasons why a DFB laser was used instead of a VCSEL source. Firstly, at the time when this experiment was designed and built, there were no 1550 nm VCSELs at hand. Secondly, the DFB laser has similar wavelength tunability characteristics to the VCSEL. The VCSELs wavelength is tuned by adjusting the bias current, whereas for the DFB, a similar result is achieved by tuning the temperature via the thermistor resistance.

8.4.1 Experimental demonstration of a time and frequency distribution using a DFB phase error correction actuator

The schematic of the frequency distribution system based on a round-trip optical fibre

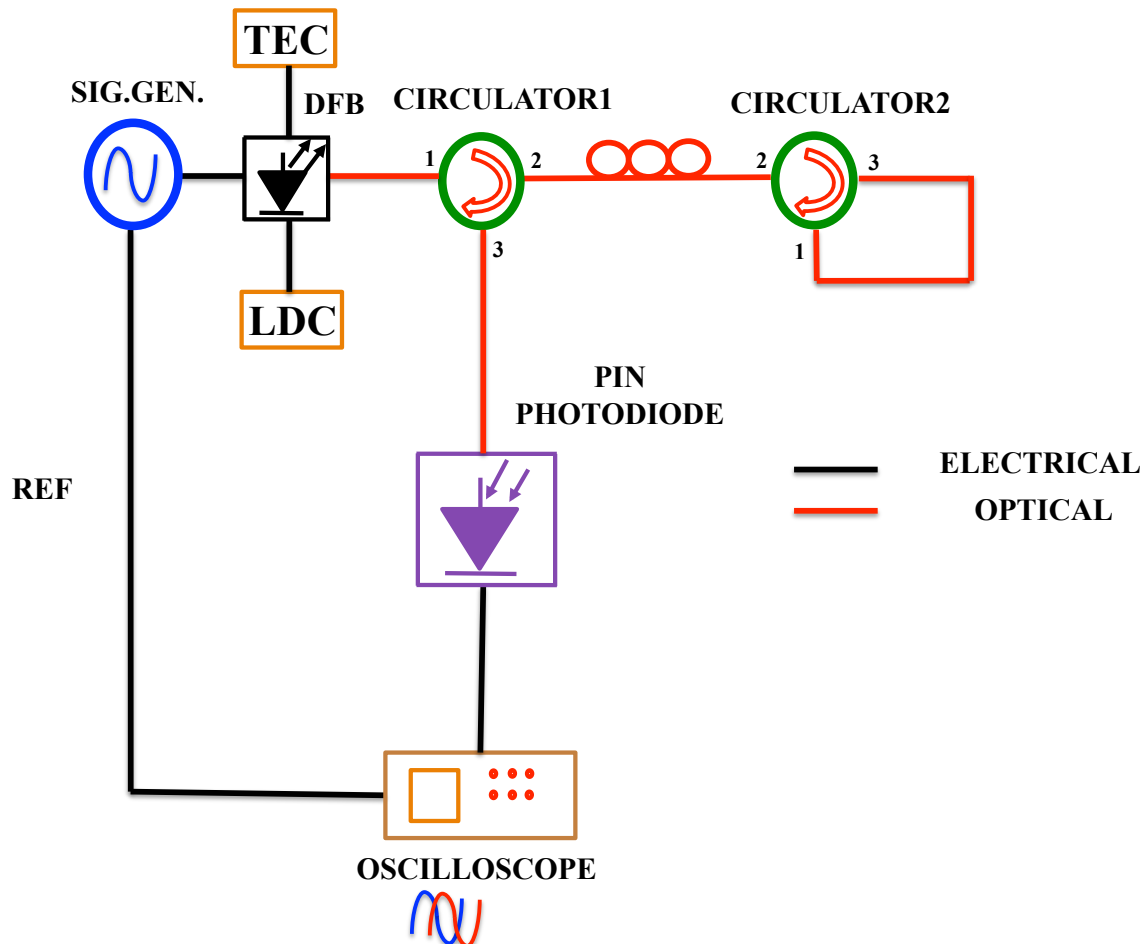


Figure 8.10: Experimental schematic of the frequency dissemination system. DFB: distributed feedback laser, TEC: thermo electric cooler, LDC: laser diode controller, SIG.GEN: signal generator.

transmission link is shown in Figure 8.10. In the experiment, a DFB laser with a peak emission wavelength of 1551.05 nm and a maximum specified output power of 15 mW was directly modulated using a 2 GHz RF clock signal generated by the R&S SMB 100A waveform generator. It was determined that by biasing the laser at the mid-point, the DFB would require 1 V_{pp} input RF clock signal. The 4.40 dBm output clock signal of the DFB laser was injected into optical circulator1 and subsequently transferred along the transmission link towards the receiver end. The LDC and TEC were used to control the bias current as well as the temperature of the DFB, respectively. During the initial lasing, when switching on the DFB, the temperature of

the DFB was set to 25°C at 10.0 kΩ, while the bias current was fixed to 50 mA. To verify the performance and robustness of the DFB-phase correcting actuator, various optical fibre lengths were used. At the receiver end, optical circulator2 was used to forward the clock signal towards the transmission end, thereby completing the round-trip. The returned optical signal was detected using a 10 GHz bandwidth PIN photodiode with an optical sensitivity of -19 dBm. Thereafter, the resultant electrical RF clock signal was captured and subsequently compared to the reference signal using an Agilent Infiniium 86100A wide bandwidth oscilloscope, with a 20 GHz bandwidth in the time domain, as seen in Figure 8.10. Depending on the amount of phase shift measured relative to the reference signal, a forward or backwards phase correction was applied to the emitted optical signal by mechanically adjusting the temperature on the TEC controller. The experimental results will be presented in the following subsection.

8.4.2 Experimental phase compensation results achieved by the DFB actuator

Before presenting the illustrative phase correction results collected along the different optical links, the DFB characterization results will first be presented and briefly

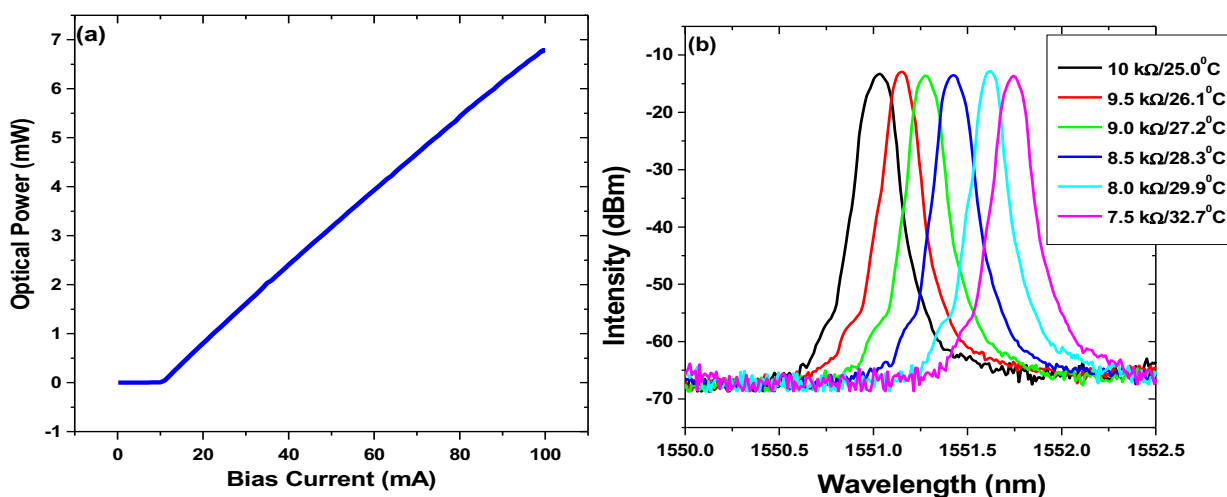


Figure 8.11: (a) Optical output power of an unmodulated DFB laser as function of bias current and the (b) optical spectra of the DFB laser the changing thermistor resistance.

discussed. Figure 8.11 experimentally presents the operational behaviour of a high-speed unmodulated 1550 nm DFB laser source. The unmodulated static characteristic of the DFB laser with changing bias current is shown in Figure 8.11 (a). From Figure 8.11 (a), the lasing threshold is seen to be approximately 10 mA whereas a 94 mA

saturation current was measured. However, a maximum bias current rating of 30 mA was specified in the datasheet. For the results to follow, a DFB bias current of 50 mA was maintained with an optical output power of 4.40 dBm. Furthermore, at this bias current setting, the DFB laser was operated within the linear region of the transfer curve. This allows for a complete swing between the on-off states of the laser when an input RF clock signal is applied. Figure 8.11 (b) shows the optical spectra of the DFB laser at thermistor resistance of 7.5 k Ω , 8 k Ω , 8.5 k Ω , 9 k Ω , 9.5 k Ω and 10 k Ω , respectively, measured at a peak-to-peak bias current (I_{pp}) of 50 mA. This result implies that when varying the thermistor resistance from 7.5 k Ω to 10 k Ω , a 0.81 nm wavelength tunability was achieved corresponding to 101.25 GHz bandwidth within the ITU grid. As seen in Figure 8.11 (b), there is a clear shift in the spectrum towards the shorter wavelength region as the thermistor resistance was increased.

Figure 8.12 illustratively shows the relative phase shift measured before and after compensation was applied along the 22.0 km G.652, 28.4 km G.652, 53 km G.655 and 6.4 km G.652 round-trip fibre links, respectively. The chromatic dispersion coefficients around the 1550 nm transmission wavelength specified for the G.655 single mode fibre is 2 ps/nm.km to 6 ps/nm.km and 17 ps/nm.km for the G.652 single mode fibres (ITU-T, 2009a, p. 13; ITU-T, 2009a, p. 13-16; OFS, 2017, p. 4). Using the in-built maker function of the Infiniium oscilloscope, the phase difference was measured between the rising edges of the resultant electrical clock signal and the reference RF sinusoidal wave. The subsequent phase error correction was then applied based on the experimentally measured phase shift, as seen in Figures 8.12 (b), (d), (f) and (h).

Phase error correction along the respective fibre links were achieved by taking advantage of the inherent chromatic dispersion properties of the optical fibre, as well as the tunability property of the DFB laser. The illustrative results presented in this section are extremely encouraging as it positively confirms the use of a VCSEL as a phase correction actuator due to the wavelength tuning similarities of the two laser sources.

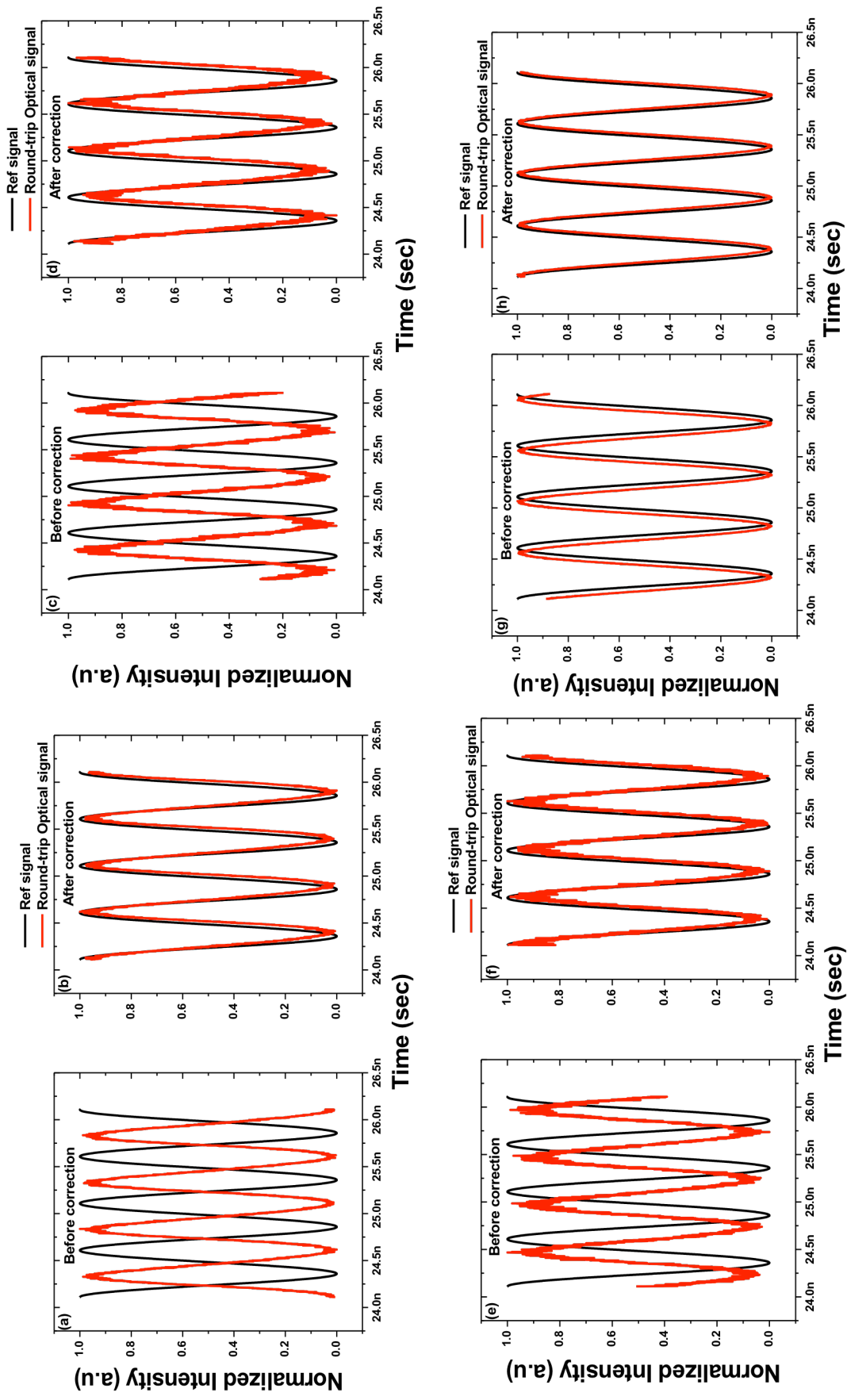


Figure 8.12: Figures (a), (c), (e) and (g) experimentally illustrates the phase shift of the transmitted signal (red waveform) relative to the reference signal (black waveform) along a 22 km, 28.4 km and a 6.4 km round-trip fibre link, respectively. (b), (d), (f) and (g) experimentally shows the phase error correction manually applied by adjusting the thermistor resistance of the TEC.

8.5 Summary

In Section 8.1, the wavelength tunability property of the VCSEL proposed for the frequency dissemination system was briefly discussed. The VCSEL provided a 280.54° phase shift across a 2 mA bias current bandwidth. For the first time ever, an error signal was generated and analysed at the Centre for Broadband Communication. The experiment presented in Section 8.2.1 provided the first error signal voltage versus time delay calibration curve.

Section 8.3 investigated the effect of fluctuating bias current on the error voltage and witnessed the first ever construction of a VCSEL based time and frequency dissemination system. The results presented in this section displayed the error signal sinusoidal behaviour as a result of the frequency mixing operation. Section 8.4 provided a proof of principle for building a timing system incorporating a VCSEL phase correction actuator. In this experiment, a DFB laser was used due to its similar wavelength tunability properties to VCSEL. However, there are trade-offs between DFB and VCSEL laser sources. VCSELs are low power, low chirp, low cost and consume low energy. Conversely, DFB lasers are high-powered devices, have a narrower linewidth, consume greater energy and cost much more than VCSELs. Here, the phase error correction was applied by manually adjusting the thermistor resistance on the TEC. With regards to the SKA, VCSELs could be implemented within the inner core area whilst DFB lasers could be integrated into the spiral arms. The chapter that follows presents, for the first time ever at NMU, the frequency dissemination results with active phase compensation using a fully integrated dither controlled VCSEL phase correction actuator.

CHAPTER 9

TIME AND FREQUENCY TRANSFER ACROSS A 26 KM OPTICAL FIBRE LINK

This chapter contains numerous phase noise compensation related results obtained using the VCSEL based time and frequency dissemination system across a 26 km optical fibre link. The results presented and discussed in this chapter serve to illustrate the novelty of using a VCSEL as a phase correction actuator within a synchronized optical network. The advantage of such a scheme in which a VCSEL is used as an optical source and an actuator is that it reduces the overall system complexity and cost. The work presented in the previous chapter was a build up to the complete frequency transfer system to be demonstrated.

9.1 Design and principle of operation

Frequency stabilization techniques using 850 nm VCSELs was previously demonstrated in which an error signal was generated for the purpose of stability analysis (Miura, Nakajima, Mizutani & Sasaki, 2007, p. 66730T-1; Ohhara, Yoshimi

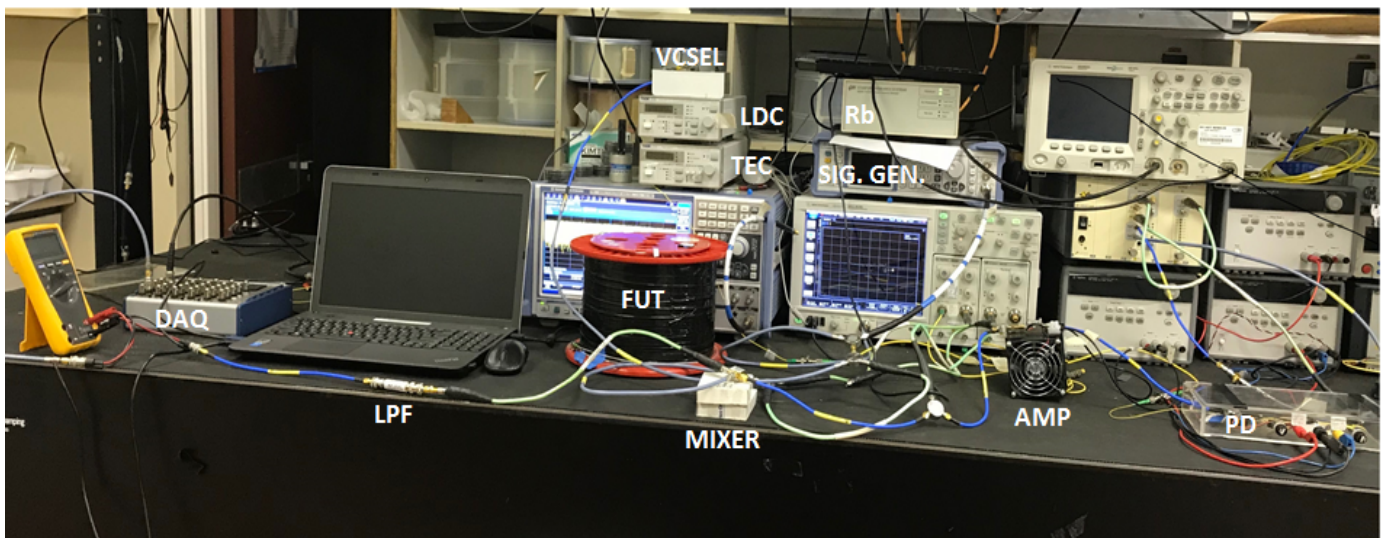


Figure 9.1: Illustrative picture of the time and frequency dissemination system. DAQ is the data acquisition boards, LPF is the lowpass filter, PD is the photodiode, Rb is the rubidium clock, SIG.GEN is the signal generator, FUT is the fibre under test, MIXER is the frequency mixer, LDC and TEC are the laser diode controller and thermoelectric cooler, respectively.

& Sasaki, 2010, p. 759724-1). Furthermore, VCSELs were first proposed for use within the SKA optical network system in 2012 (Kipnoo, Waswa, Leitch & Gibbon, 2012a, p. 523-527; Kipnoo, Kourouma, Waswa, Leitch, & Gibbon, 2012b, p. 483-484).

The frequency dissemination scheme designed and developed by the author at the Centre for Broadband Communication is shown in Figure 9.1. The system was primarily designed to actively compensate for phase noise and shift of the optical signal, in real time, along the fibre transmission link. It will be later shown that the one-way optical fibre time and frequency transfer method based on the newly proposed dither controlled VCSEL phase error correction actuator was able to detect any phase perturbations, apply the necessary correction and lock to the stable reference clock signal in approximately 0.15 sec. The principle describing how the frequency dissemination system compensates for any phase perturbations along the optical fibre is illustratively shown in Figure 9.2.

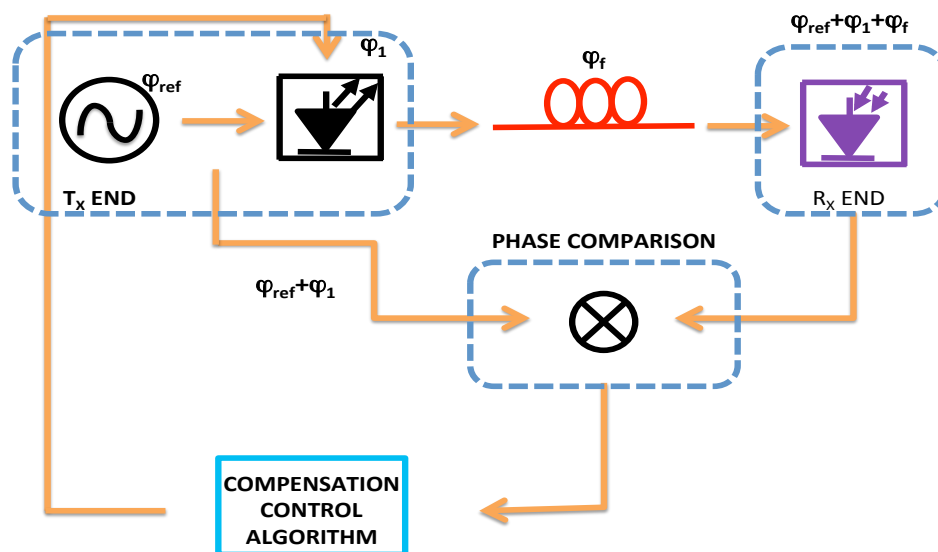


Figure 9.2: Block diagram showing how phase fluctuation compensation is achieved.

The reference clock with an initial phase, φ_{ref} , is used to drive a VCSEL as illustrated in Figure 9.2. The VCSEL introduces a fixed phase shift of φ_1 to the frequency dissemination system. The sinusoidal modulated laser beam is then sent along the fibre link, which in turn induces an additional phase shift, φ_f , in the one-way direction.

$$\varphi_{Total} = \varphi_{ref} + \varphi_1 + \varphi_f \quad (9.1)$$

Equation 9.1 mathematically describes the total phase fluctuation accumulated along the one-way transmission path from the transmitter site to the receiver end. In a round-trip frequency dissemination configuration, the same optical fibre transmission path can be used to determine the induced phase error, φ_f , based on the assumption that the transmitted signal along the forward and returned link are corrupted by the same perturbation. However, the fibre induced phase change along the round-trip link is given as $2\varphi_f$ (Hou, Li, Liu, Zhao & Zhang, 2011, p. 506-511; Narbonne et al., 2006, p. 064701). The phase difference measurement between the disseminated sinusoidal waveform and the stable reference signal is realized by using a frequency mixing technique, as illustrated in Figure 9.2. After mixing down Equations 9.1 and 9.2 as demonstrated in Figure 9.5, an error signal was generated for feedback control of the phase VCSEL optical source.

$$\varphi_{ref} + \varphi_1 \quad (9.2)$$

A specialized RF cable was used to forward the error voltage generated after the frequency mixer to a data acquisition (DAQ) board, illustratively shown in Figure 9.1. Together with a dither-step algorithm, a resultant error voltage was generated at the output of the DAQ board and transmitted to the laser diode controller (LDC). In order to stably disseminate a frequency signal to a receiver location, a phase error correction was applied to the optical signal emitted by the VCSEL. The applied phase error correction must be of such a value that cancels out the one-way phase fluctuations. The following section presents a detailed discussion describing the dither-step algorithm used towards generating the feedback control resultant error voltage.

9.2 The dither-step algorithm

The dither gradient-based technique is possibly one of the oldest optimization algorithms to date. The gradient-based technique has attracted a revived interest among researchers in various branches within the scientific fraternity (Beck, & Teboulle, 2009, p. 42-88). The objective of the phase drift or phase noise compensator is to minimize or negate the fibre induced time delay by regulating the control voltages related to the compensator. The relationship between the actuator control

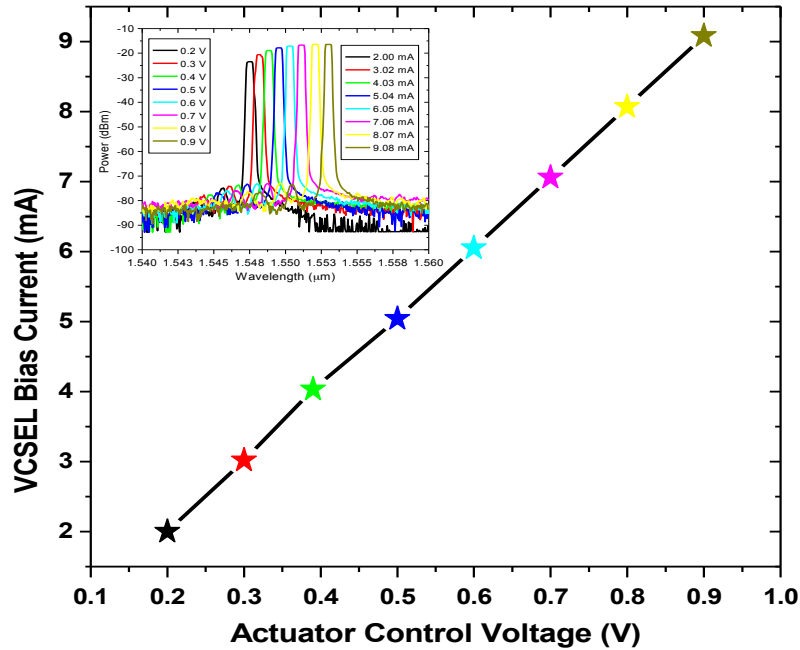


Figure 9.3: Experimental demonstration showing the linear relationship between the actuator control voltage and the VCSEL bias current. The insert illustratively shows the wavelength shift associated to each control voltage value.

voltage and the VCSEL bias current is given in Figure 9.3. There are three general steps involved when controlling the VCSEL phase error correction actuator. The first step is to determine and find the optimum bias point immediately after the VCSEL compensator is switched on. The second process involves the continuous real-time tracking and measuring of the error signal voltage associated to the phase difference between the transmitted and reference signals. The third and most crucial step is to lock the two signals after finding the optimum error voltage associated to a zero degree phase difference between the two respective signals.

During a typical iteration process encoded within the dither gradient-based search algorithm, each control voltage associated with the bias current of the VCSEL phase correction actuator, is initially increased or decreased by a small incremental amount about its voltage corresponding to the optimum operational VCSEL bias point. After each iterative process the generated error voltage is compared to a specific threshold voltage value and any improvements in the error signal is noted. It is to be remarked that the objective for executing the dither gradient-based search algorithm is to minimize the error signal voltage as this value corresponds to a zero degree phase difference between the reference and dissemination signal, as discussed in Chapter

8.3.2. A suitably selected step size is implemented within the code to increase or decrease the control voltage at the output port of the data acquisition board, for which the dithering algorithm yields the smallest negative number in millivolts (mV). This stepping procedure is what initiates the search process for the minimum points of the sinusoidal error signal. For the dissemination experiment described in this work, the speed at which the dithering algorithm finds the appropriate minimum voltage value that ensures the error signal is minimized depends on the step size. The dither step code is sequentially repeated until the error signal voltage is minimized ensuring the reference and transmitted signals are in-phased and locked.

The pseudo-code for the dither gradient-based algorithm implemented within the time and frequency dissemination described in this thesis is as follows,

1. Create a data acquisition session for the NI DAQ boards and initialized the output start voltage that corresponds to the optimum operational bias point for the VCSEL. The initialized start voltage used to control and bias the VCSEL is divided by a factor of ten.
2. Define the VCSEL bias current operational ranges associated to the output voltage that efficiently locates the local minimum of the error signal.
3. Define a series of local minima threshold target values related to the error signal generated during the mixing process.
4. Set the initialized start voltage to new variable called NewDCv.
5. Collect and store the time and error voltage values in an array format.
6. If the VCSEL bias point, associated with a distinct output voltage, falls within a certain voltage operational range then a specific threshold target value is assigned.

```

if (newDCv >= A) && (newDCv < B)
    target = targetAB;
elseif (newDCv >= B) && (newDCv < C)
    target = targetBC;
elseif (newDCv >= C) && (newDCv < D)
    target = targetCD;
elseif (newDCv >= D) && (newDCv < E)
    target = targetDE;

```

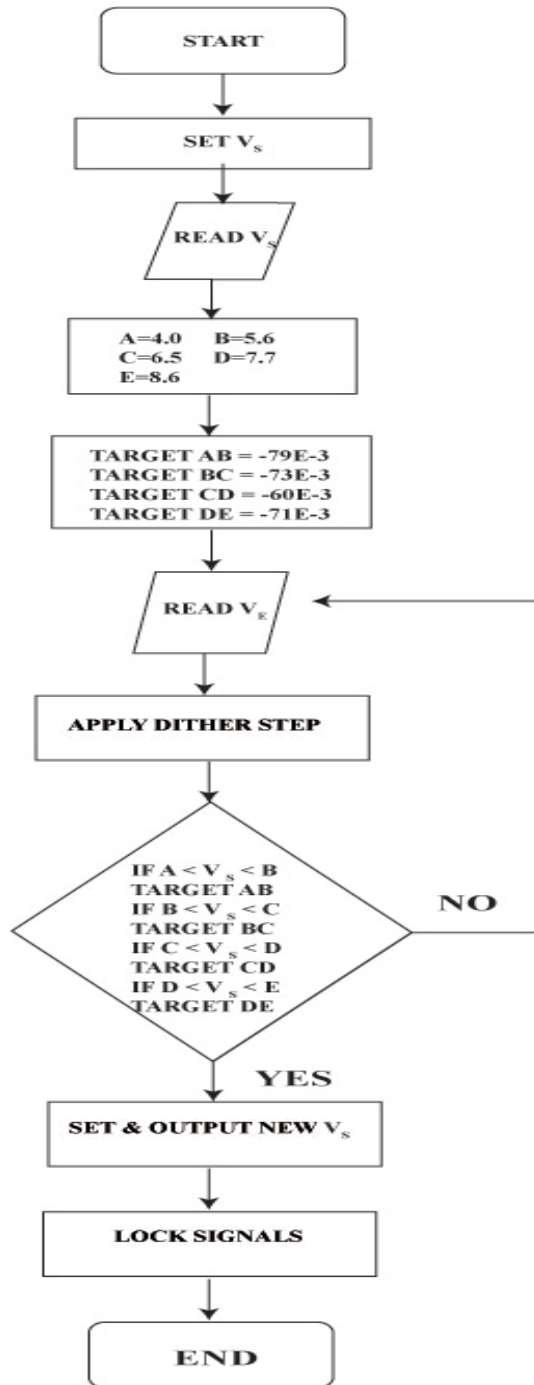


Figure 9.4: Flowchart of the Matlab dither algorithm.

7. By repeating the dither step sequence, the new incoming error voltage at the input port of the data acquisition board is compared to the unique threshold target value. This process is made possible by implementing a while loop.

8. The loop is repeated until a compensated state is found and the signal disseminated along the fibre is phase locked the stable reference sinusoidal waveform.

The flowchart describing the Matlab code is illustratively shown in Figure 9.4. Experimental results for the real time dither controlled phase error compensator are illustratively shown and described in the sections that follow.

9.3 Experimental setup of the VCSEL based time and frequency dissemination scheme

This section presents the experimental configuration describing the precise time and frequency synchronisation system based on a conventional 26 km G.655 optical fibre

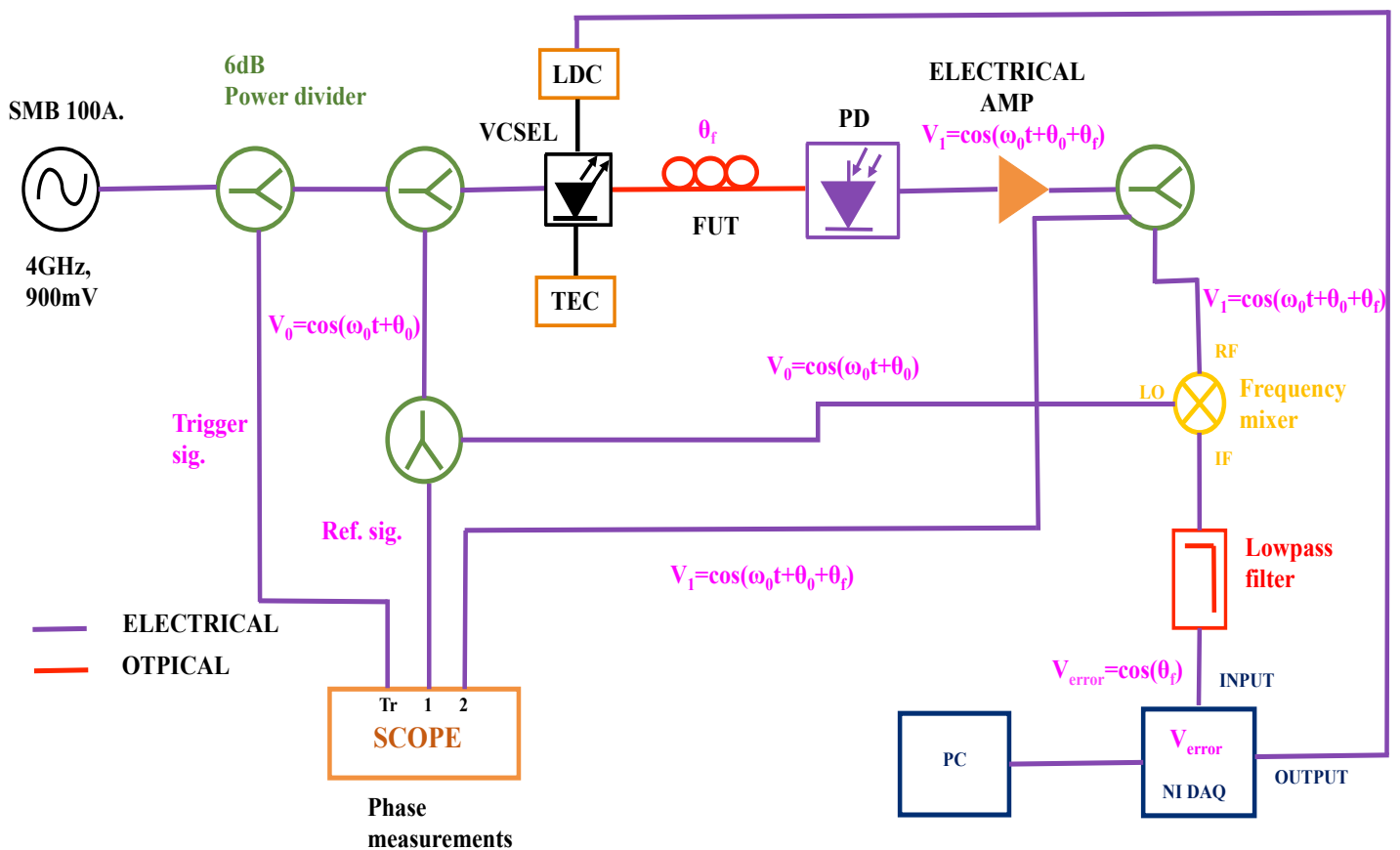


Figure 9.5: Experimental demonstration of the optical fibre time and frequency dissemination system used for phase drift compensation.

dissemination link. In this dissemination setup, the precise frequency and phase of the stable clock at the transmitting site is transferred to the receiver location. As a result,

the frequencies and phases of the two sinusoidal signals are identical. The schematic diagram of the frequency dissemination scheme optimized for time domain signal analysis based on the dither controlled VCSEL phase correction actuator is illustratively shown in Figure 9.5.

In the frequency distribution setup given in Figure 9.5, a 4 GHz electrical clock signal with an output power of 900 mV was phase locked to the VCSEL optical source. The microwave signal was generated using an R&S SMB 100A waveform generator. The high-powered R&S SMB 100A signal generator covers a wide frequency range from 100 kHz and 20 GHz. In the experimental configuration given in Figure 9.5, the 4 GHz reference clock signal was used to directly modulate the amplitude of a 1310 nm temperature controlled VCSEL with a lasing wavelength of 1306.89 nm at 7 mA, as specified in the specification sheet.

The first 6 dB resistive power divider located immediately after the R&S SMB 100A waveform generator was used to split in initial RF signal into two parts, as seen in Figure 9.5. The first half of the RF signal was used as a trigger function, allowing the sinusoidal waveforms to be displayed on the wideband Infiniium oscilloscope. Whereas the second portion of the divided clock signal was used as a reference and also to drive the VCSEL, as seen in Figure 9.5. The resistive power dividers incorporated into the frequency dissemination scheme presented in Figure 9.5 have a typical insertion loss 6 dB between any two ports. An additional three resistive power dividers were used to split and forward the RF signal as shown in the experimental configuration given in Figure 9.5. In this experiment, the VCSEL temperature was maintained at 25°C corresponding to a 10 k Ω thermistor resistance setting on the TEC. The VCSEL was biased above the threshold using the LDC, however, the bias current was initialized and controlled via the LDC using the dither control algorithm. The -3.31 dBm modulated optical signal, whose power is lower than the stimulated Brillouin scattering threshold, was launched into the 26 km G.655 spooled fibre and subsequently disseminated across transmission link from the local site to the receiver site. Upon reaching the receiver end, the modulated clock signal was detected with a standard positive-intrinsic-negative (PIN) photodiode with a typical optical sensitivity of -19 dBm, as specified by the manufacturer. The resultant electrical clock signal

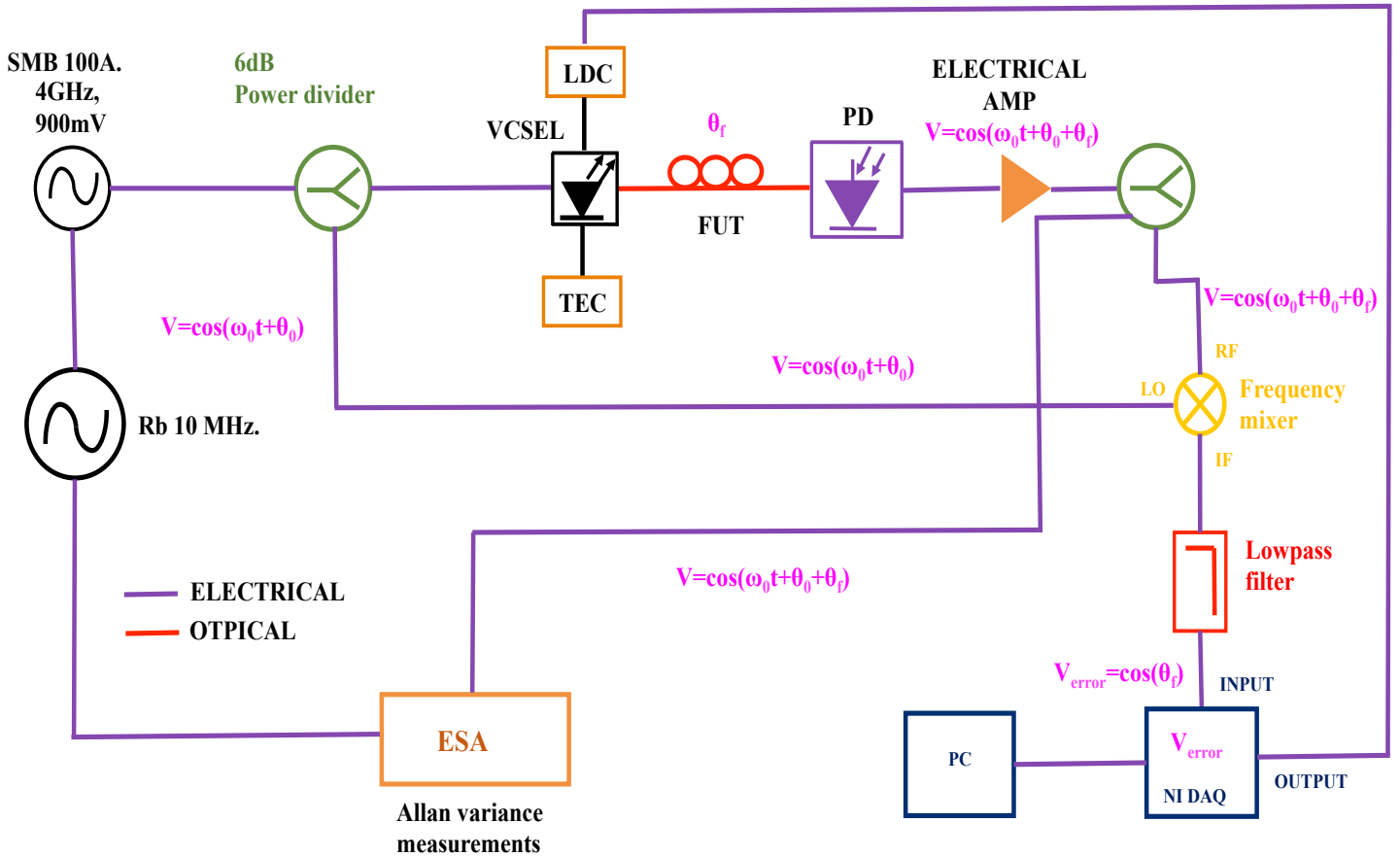


Figure 9.6: Schematic diagram of the optical fibre time and frequency dissemination system optimized for Allan variance analysis

after the photodiode (PD) was amplified using a wideband electrical amplifier with a typical gain of 27 dB, as specified in the data sheet. Through a series of electronic operations occurring after the PD, an error signal V_{error} proportional to the phase difference $\theta_0 + \theta_f$ was generated for feedback control of the VCSEL phase correction actuator. The electronic operations referred to in this text includes the down mixing of the resultant electrical signal, $V_1 = \cos(\omega_0 t + \theta_0 + \theta_f)$, with the reference signal $V_0 = \cos(\omega_0 t + \theta_0)$ and the filtering out of the baseband signal. This operation is illustratively shown in Figure 9.5. The RF mixer used in this experiment has a typical conversion loss of 6 dB, while the 50Ω low pass filter (LPF) only permits frequencies within the DC to 22 MHz range to pass through. A low attenuation speciality RF cable was used to forward the DC error voltage, V_{error} , after the LPF towards the input port of the NI DAQ board, as shown the Figure 9.5. After executing the dither step algorithm described in Section 9.2, the resultant error control voltage was sent to the modulation input or the analog control input port at the rear end of the

LDC. This allows for the optical signal emitted from the VCSEL to be tuned either forward or backward thereby correcting for any phase perturbations occurring along the fibre path. A wide band Infiniium oscilloscope with a specified 20 GHz bandwidth in the time domain was used to monitor the real time relative phase difference between the reference and transmitted signals, as illustrated in experimental setup. Figure 9.6 experimentally illustrates the one-way RF dissemination system specifically optimized for Allan variance evaluation. In this configuration a wide bandwidth electrical spectrum analyser (ESA) with a 0.01 Hz frequency measurement resolution was used to analyse the stability of the disseminated signal in the frequency domain.

9.4 Characterization of the 1310 nm VCSEL phase correction actuator

Before presenting the effectiveness of the dither controlled VCSEL actuator as well as the fractional frequency stability results, this section begins by presenting some VCSEL characterization results. The biasing and emission wavelength tunability properties of the VCSEL is experimentally demonstrated and reported in Figure 9.7.

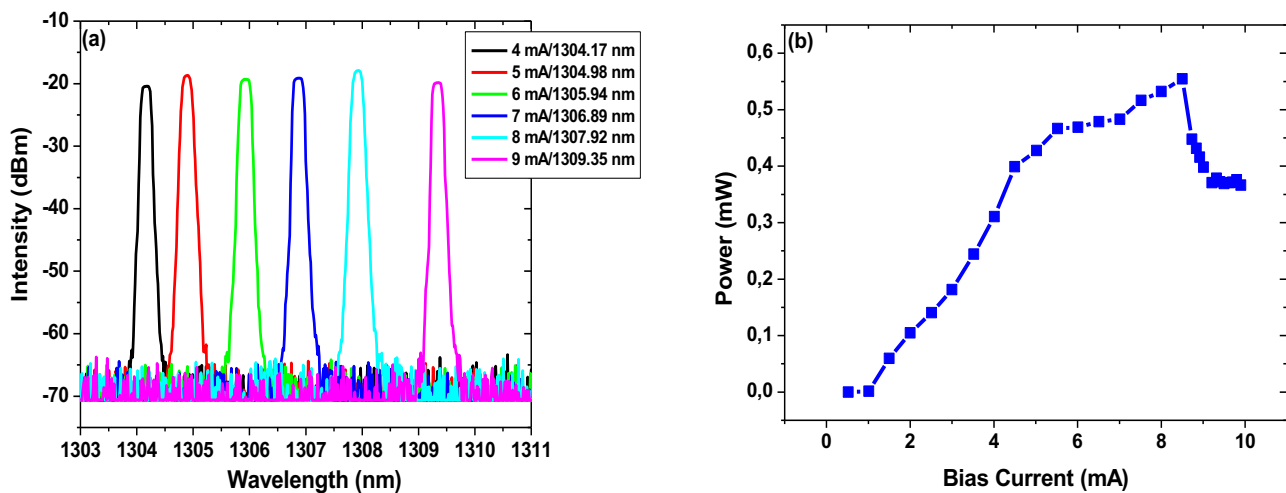


Figure 9.7: Experimental characterization illustrating the (a) optical output power of the VCSEL as a function of varying bias current and (b) optical spectra for different VCSEL bias currents.

Figure 9.7 shows the wavelength tunability property of the 1310 nm VCSEL measured with a 0.06 nm resolution optical spectrum analyser (Agilent Technologies, 2012, p. 2). For the result illustrated in Figure 9.7 (a) the VCSEL was biased above its threshold current to give sufficient output optical power. Figure 9.7 (a) shows that the

emission wavelength was tuned from 1304.17 nm to 1309.35 nm by increasing the bias current from 4 mA to 9 mA. This result suggests that a 5 nm wavelength tunability range was achieved, corresponding to a 625 GHz bandwidth within ITU grid, by varying VCSEL bias current from 4 mA to 9 mA. Figure 9.7 (b) experimentally shows the static characterization of the VCSEL optical output power as a function of bias current. In the result shown in Figure 9.7 (b), the bias current was changed from 0.52 mA to 9.9 mA. Furthermore, the threshold current of the VCSEL was seen to be at 0.99 mA while the saturation current was seen to be at 8.48 mA. However, a maximum bias current rating of 4 mA is specified in the datasheet (Raycan, 2015). Above the 8.48 mA bias point, the output power of the VCSEL was seen to decrease as the bias current was further increased. For the results presented in Sections 9.5 and 9.6, the VCSEL bias current was set and initialized to 5.56 mA using the dither step algorithm, providing an optical output power of -3.31 dBm. This bias point ensures that the VCSEL was biased at the midpoint of the linear region, along the transfer function curve thereby providing the optimum transmission performance.

9.5 Performance evaluation of the dither control VCSEL phase correction actuator

In this section the experimental setup illustratively shown Figure 9.5 together with the dither step algorithm discussed in Section 9.2 was used to evaluate the performance of the dither controlled VCSEL actuator in tracking phase fluctuations of the disseminated RF signal along the fibre. Furthermore, the effectiveness of the dither controlled VCSEL actuator in applying the necessary phase correction is also assessed. The experimental results illustratively showing the real time error signal voltage fluctuation, over a five-hour ($\sim 2 \times 10^4$ second) period are presented in Figure 9.8. For the experimental results presented in Figure 9.8, the acceptable error voltage threshold (black line) selected was -90 mV whereas the VCSEL actuator was optimally biased at 5.56 mA. The threshold value and optimum bias point was assigned an initialized within the dither-step algorithm. The red sinusoidal curve in Figure 9.8 represents the error signal generated when the frequency dissemination system was running freely, without any active compensation.

The error signal under consideration corresponds to the fluctuating phase difference between the stable reference signal and the disseminated signal along the fibre. This

result shows that the error voltage fluctuates in a sinusoidal manner as the relative phase between the reference and the transmitted signal changes in real time. The phase variations referred to in this text can be to the attributed drifting phenomenon of the signal along the fibre link as well as that of the VCSEL in the unlocked state. Figure 9.8 further shows that the error signal fluctuates between -90 mV to 100 mV. It can be seen that the error voltage fluctuates within a ~ 200 mV range around the

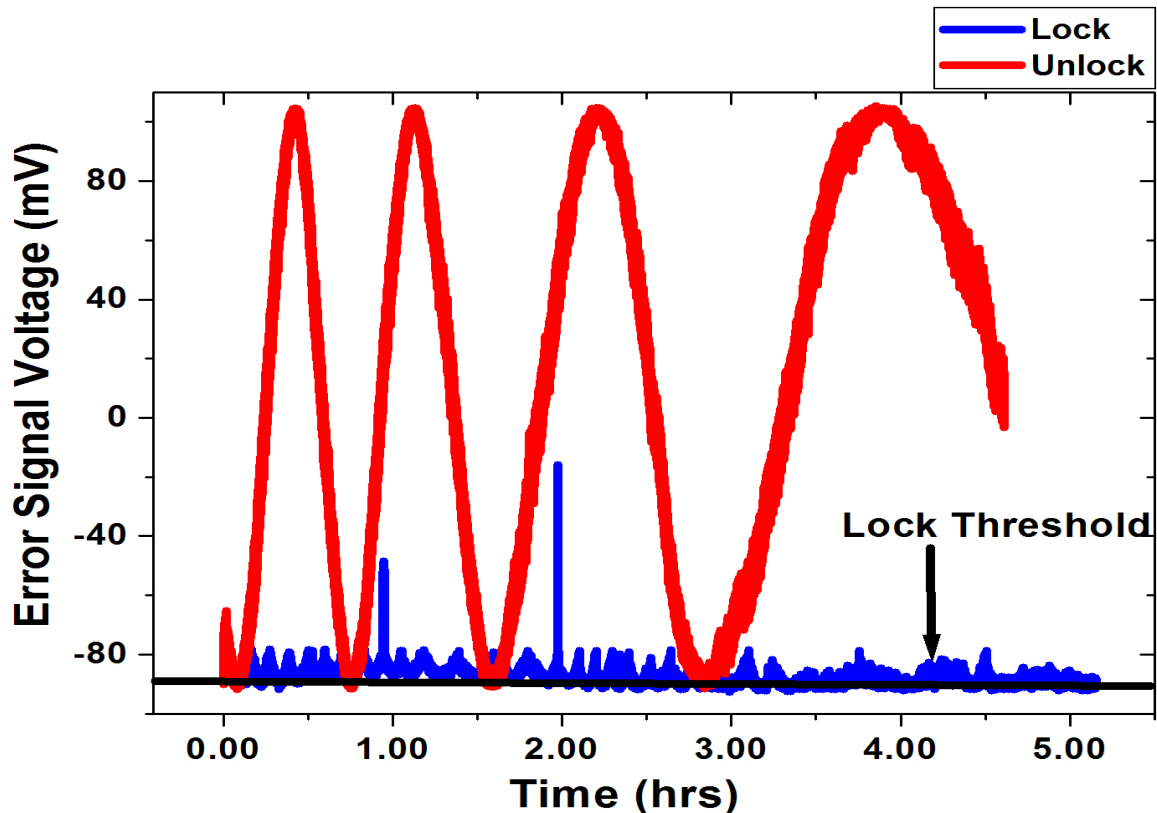


Figure 9.8: Experimental error signal behaviour with and without dither controlled active phase compensation. The red and blue curves represent the error signal performance during the unlocked and lock state, respectively. The black line indicates the acceptable error voltage threshold.

0 mV point as the reference waveform and the distributes signal drifts towards and away from each other, as illustrated and discussed in Chapter 8.3.2.

The blue curve illustratively shown in Figure 9.8 represents the resultant error signal measured after the RF mixer-LPF when the fibre induced phase perturbation was actively compensated. As previously mentioned, the phase correction compensator consists of three distinct processes. The first process is the initialization of the dither controlled VCSEL actuator and to find an optimum operating bias point. The second process involves checking whether the start voltage associated to the optimum bias

point falls with the acceptable voltage operation ranges. The third process establishes the ideal error voltage associated with the best bias point that minimizes the error signal towards the appropriate target threshold. For evaluating the in loop performance of the dither controlled VCSEL phase error compensator, the appropriate voltage operation limits selected was $A=4.1$, $B=5.7$, $C=6.3$, $D=7.5$, $E=8.6$. The corresponding threshold target values chosen were $\text{targetAB} = -88.1$ mV, $\text{targetBC} = -89.3$ mV, $\text{targetCD} = -87.9$ mV, $\text{targetDE} = -88.7$ mV. Both the voltage operation limits and the threshold target values were initialized and set within the dither step algorithm, as described in Section 9.2. The bias point was optimally initialized to 5.56 mA using the dither step algorithm.

It is to be remarked that the error signal denoted by the blue line in Figure 9.8 corresponds to the temporal duration in which the transmitted signal is phase locked to the reference signal over the five-hour time period. This result further shows that the error voltage remains minimized and constant during the entire five-hour period the phase noise compensation system was activated. A -88.5 mV error voltage was experimentally recorded which corresponds to zero phase difference between the transmitted and reference signal, as mention in Chapter 8.3.2. The two spikes seen

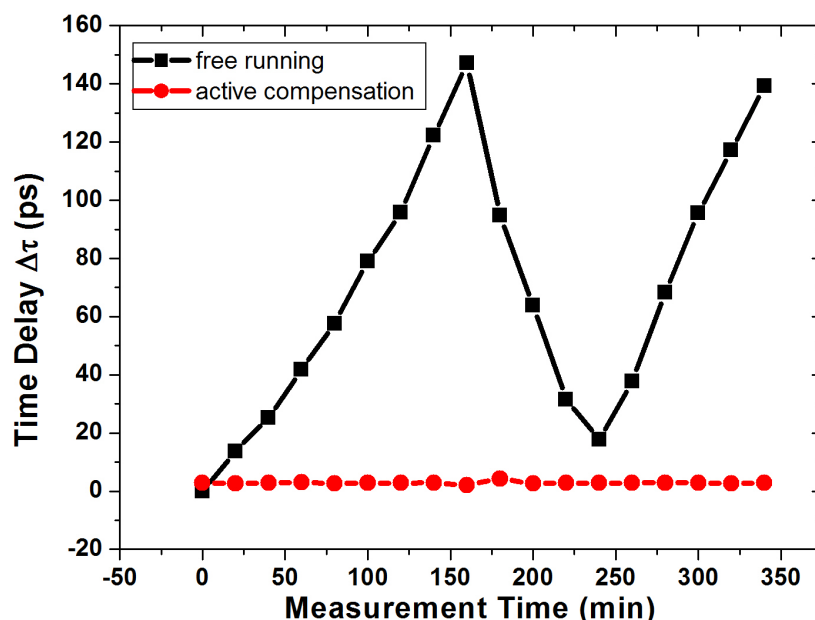


Figure 9.9: Relative time delay fluctuations between the reference and disseminated RF signal for the locked and unlocked state.

along the blue line in Figure 9.8 represent an event where the VCSEL drifted causing a phase change to occur between the two signals. As a result, the error voltage deviates from the acceptable threshold target value. The error voltage generated during this process corresponds to a time delay occurring between the disseminated and reference signals. The iterative loop of dither step algorithm described in Chapter 9.2 was executed and repeated and real time phase compensation is swiftly applied. Figure 9.9 show the experimental time delay between the stable reference signal and the transmitted optical signal along the 26 km G.655 fibre link. The time delay in ps was measured by making use of the marker function of the wideband Infiniium oscilloscope. The black curve in Figure 9.9 shows the time delay fluctuation of the distributed signal relative to the reference signal when the dissemination system was in free running mode over a 350-minute or approximately a five-hour period. This result further shows that the while the frequency dissemination system was in free-running mode, the relative time delay fluctuated away from 0 ps to 157.16 ps as distributed signal drifted from away from the reference. The separation time further changes from 157.16 ps to 31.54 ps and from 31.54 ps to 139.20 ps as the transmitted signal drifted towards and away from the reference signal, as seen in Figure 9.10 (a). The red line displayed in Figure 9.9 represents the time delay fluctuation of distributed signal relative to the reference signal while the phase noise compensation mechanism was activated. While in the closed loop system, the time delay

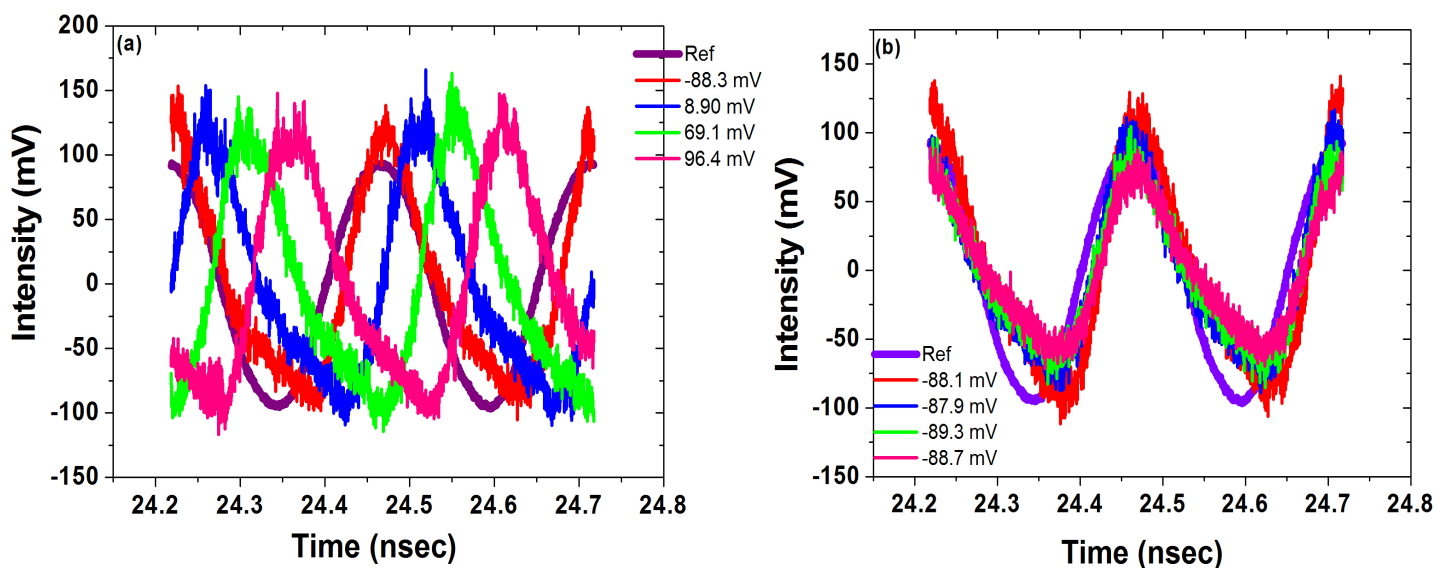


Figure 9.10: Experimental demonstration of the relative phase shift between the disseminated and reference signals during (a) free run and (b) active compensation mode.

fluctuations between the distributed relative and the reference signals were reduced, as seen in Figures 9.9 and 9.10 (b). An average time delay of was 2.84 ps measured while the fibre induced phase error compensator was activated. As mention previously, the experimental results were measured over a 350-minute or approximately five-hour period.

It is to be remarked that the noisy signals seen in Figure 9.10 can be attributed to the noise generated by the electrical amplifier and the resistive power dividers, seen in the experimental setup illustratively shown in Figure 9.5. It is to be noted that the reason for using four resistive power dividers was to capture and monitor the signals in real time on the oscilloscope, as described in Figure 9.5. Furthermore, the dissemination configuration described in Figure 9.5 was developed in order to evaluate the performance of the dither controlled VCSEL phase correction actuator, of which the results are presented in this section.

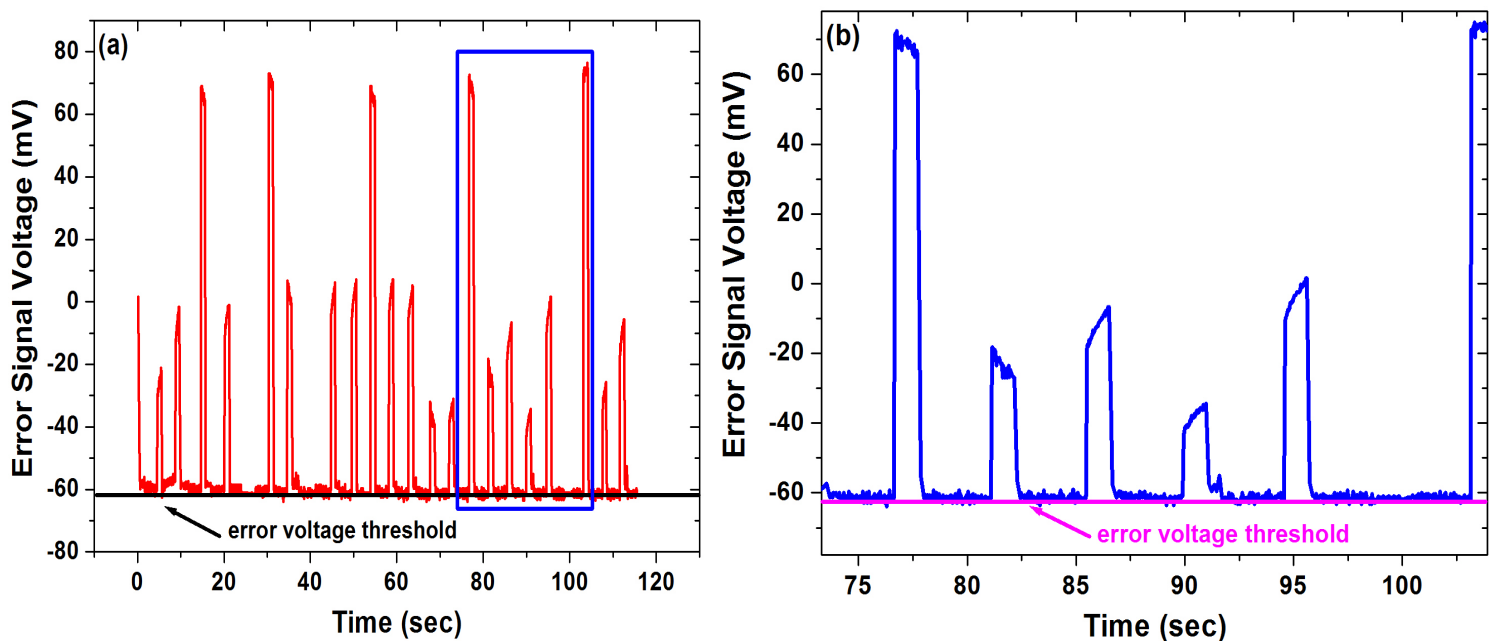


Figure 9.11: Experimental demonstration of (a) error voltage behaviour as a function of time and (b) magnification of the results in (a). The black and magenta coloured lines represent the error voltage threshold limits.

An interesting experimental result describing the performance of the dither controlled VCSEL phase correction actuator over a 120 second measurement period is presented in Figure 9.11. The result also shows the error voltage fluctuation during the measurement period. The Matlab based, dither step algorithm used for generating the

error signal given in Figure 9.11 was subtly change in order to assess the performance of phase drift compensator. To generate the error signal seen in Figure 9.11, the start voltage and the appropriate voltage operation regions was determined and initialized using the dither step algorithm. Thereafter, a suitable error voltage threshold was selected that best minimizes the error signal. An acceptable start voltage corresponding to an ideal lasing bias current of 5.31 mA and an error voltage threshold of -63 mV was chosen and initialized within the dither step algorithm. The voltage ranges used was $A=3.0$, $B=4.5$, $C=5.7$ and $D=6.7$. Once the phase compensation process was initialized and the favourable voltage regions were explored and threshold value satisfied, the locking process was initiated. A three second locking time was introduced into the dither step algorithm. This particular command was implemented in order to phase lock the transmitted signal to the stable reference signal for a period of three seconds, as demonstrated in Figure 9.10 (b). The error voltage was purposefully shifted relative to the -63 mV threshold. This process was realized by randomly changing the start voltage value between 5.3 V and 6 V, after the initialization steps were executed. This caused a rapid change in the VCSEL bias current resulting in a fluctuating error voltage. The spikes highlighted and

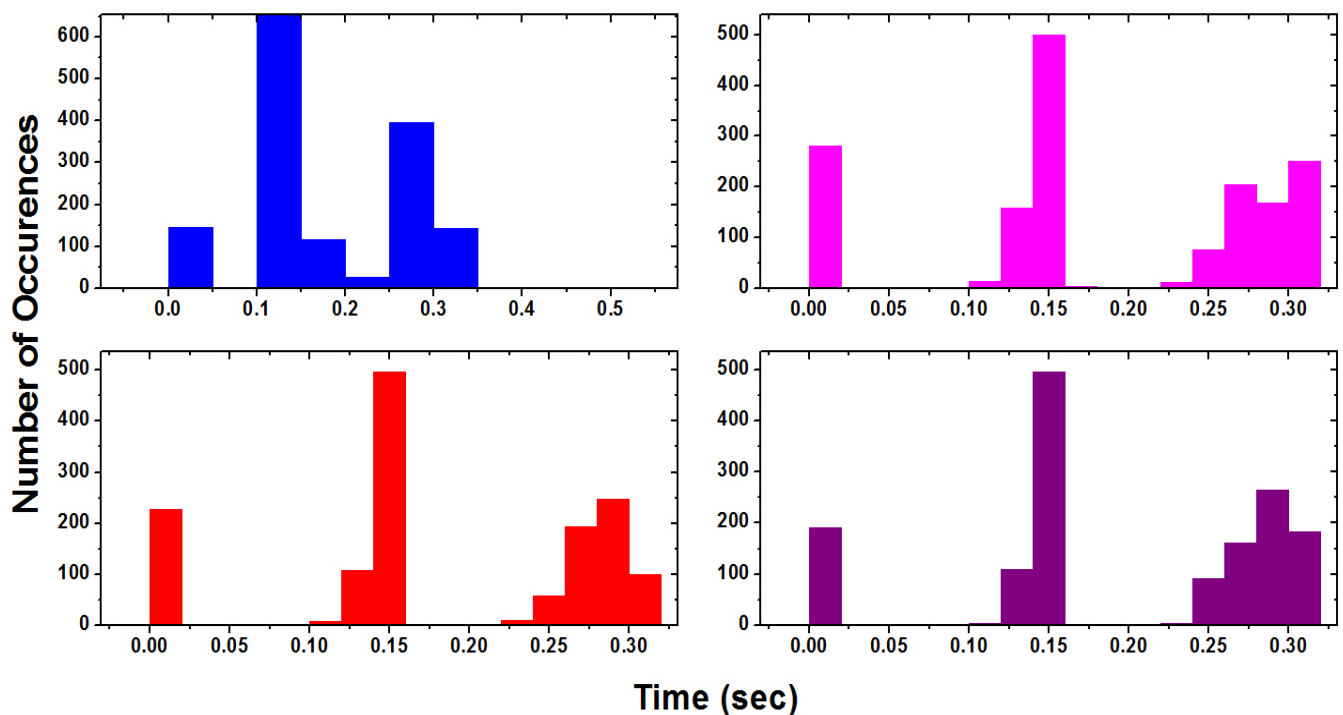


Figure 9.12: Experimental results showing the compensator response time for applying the required phase correction.

magnified in Figures 9.11 (a) and (b), respectively represents the event in which the iterative dither step sequence is activate. During this process, the error voltage is tracked and a new VCSEL actuator control voltage is selected that satisfies the voltage operational limits and the threshold condition. The new control voltage corresponding to the optimum VCSEL biasing point and a new minimized error signal is generated. Once the threshold condition is satisfied, the phase compensator is activated and the transmitted stable reference signals are phase lock for a three second period. The loop was then repeated over a period of 120 seconds. The dither controlled VCSEL compensator response time required to correct for the any phase fluctuations along the fibre is shown in Figure 9.12. From the results illustrated in Figure 9.12, it can be seen that majority of the dithering iterations took approximately 0.15 sec, after the VCSEL bias current was intentionally altered. As mentioned previously, some of the tasks executed within the iterative loop may include monitoring the error voltage, exploring the different operational regions, selecting the best error voltage threshold and applying the required phase correction. The result further shows that the shortest event occurs below 0.025 sec whereas the longest event last approximately 0.35 sec.

In summary, the compensation system described here was artificially perturbed using the dither-controlled algorithm by intentionally unlocking it for three seconds. Thereafter, the time taken for the system to lock was recorded. This process was repeated to generate Figures 9.11 and 9.12, indicative of the compensation device's performance.

9.6 Experimental Allan deviation analysis along the 26 km G.655 optical fibre transmission link

Sections 9.4 and 9.5 presented the experimental characterization and the performance analysis of the 1310 nm dither controlled VCSEL phase noise actuator, respectively. In this section, the relative frequency stability of the transmitted signal along the 26 km G. 655 optical fibre link is experimentally evaluated and presented. This was realized by comparing the measured, relative Allan deviation results of the recovered disseminated signal to the original electrical signal generated by the R&S SMB 100A. The transfer performance the R&S SMB100A signal generator expressed in terms of an Allan variance is experimentally demonstrated in Figure 9.13. The resultant 4 GHz

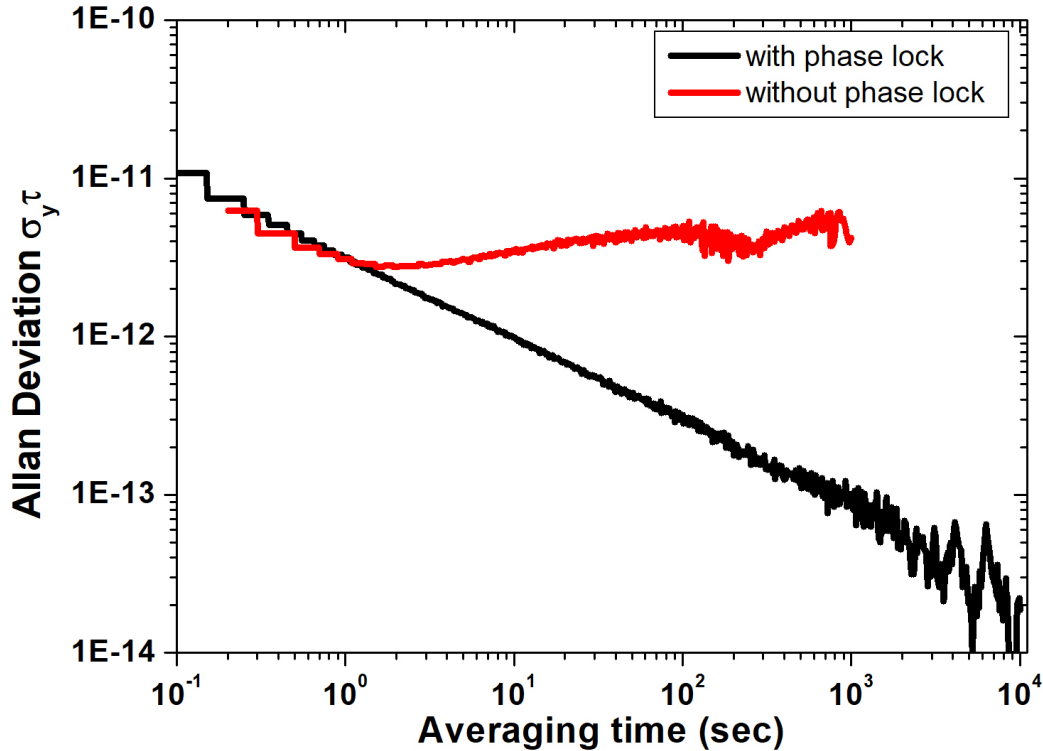


Figure 9.13: Experimentally measured frequency stability of the original electrical signal generated by the R&S SMB 100A waveform generator. The black line shows the stability result of the R&S SMB 100A phase locked to a Rb atomic clock, as shown in Figure 9.6. The red line shows the stability measurement of the R&S SMB 100A not phase locked to the Rb atomic clock.

electrical signals after the PD, measured with a frequency counter resolution of 100 mHz, was analysed with the R&S ESA as shown in Figure 9.6. Thereafter, the Allan deviation of the RF signal was computed using the computer based R&S Allan variance software. For the Allan deviations presented in this section, the following parameters were configured within the computer based R&S Allan variance software.

A delta tau ($\Delta\tau$) of 100 ms was selected whereas a tau-stop setting of 10 ks was chosen. The red line in Figure 9.13 shows the frequency stability of the 4 GHz electrical RF signal before being modulated onto the VCSEL. The red line further represents the stability of the R&S SMB100A signal generator without being phase locked to the Rb atomic clock. Frequency stabilities of $3.09251 \times 10^{-12}/1$ s and $4.20288 \times 10^{-12}/10^3$ s were experimentally measured. Furthermore, the black line shows the frequency stability result of the R&S SMB100A signal generator phase locked to the Rb atomic source. Short and long-term frequency stabilities of $3.14085 \times 10^{-12}/1$ s and $1.01619 \times 10^{-13}/10^3$ s were experimentally reported, respectively. When

drawing a comparison between the two lines given in Figure 9.13, a clear improvement can be seen in the long term averaging of the black curve. This clear result is directly attributed to the fact that the R&S SMB100A signal generator was phase locked to the Rb atomic clock. However, Figure 9.13 further shows that the short-term stability performance of the two curves are similar and follows the same trend between 0.1 s to 10 s. The instability of the R&S SMB100A signal generator described by the red line can be attributed to the noise contribution of the internal electronic components of the waveform generator. From Figure 9.13, it is to be remarked that the noise type represented by the black line may be classified as white

Table 9.1: Experimental Allan variance results.

	with phase lock	w/o phase lock
Ave. Time (sec)	Allan Deviation	Allan Deviation
1 s	3.14085×10^{-12}	3.09251×10^{-12}
10 s	9.87237×10^{-13}	3.42871×10^{-12}
100 s	2.82025×10^{-13}	4.78368×10^{-12}
1000 s	1.01619×10^{-13}	4.20288×10^{-12}

phase noise, flicker phase noise or white noise. However, Allan deviation does not differentiate between white phase noise and flicker phase noise. The noise contributions could be related to the physical resonance mechanisms of the oscillator. Furthermore, the noise contributions associated to the red Allan deviations curve given in Figure 9.13 may be categorized as white phase noise, flicker frequency noise and random walk frequency noise, respectively. Here the noise types might be related to the resonance mechanisms of the oscillator as well as the ambient surrounding conditions. These may include factors such as temperature and vibrations. Table 9.1 provides a tabulated summary of the stability performance of the R&S SMB100A signal generator before and after being phase locked to the Rb atomic clock. It is to be remarked that the source of instability changes the phase of the optical signal along the fibre.

Figure 9.14 shows the experimentally measured fractional frequency stability of free running and active phase noise compensated system. For the results presented in Figure 9.14 the R&S SMB100A waveform generator was phase locked to the Rb

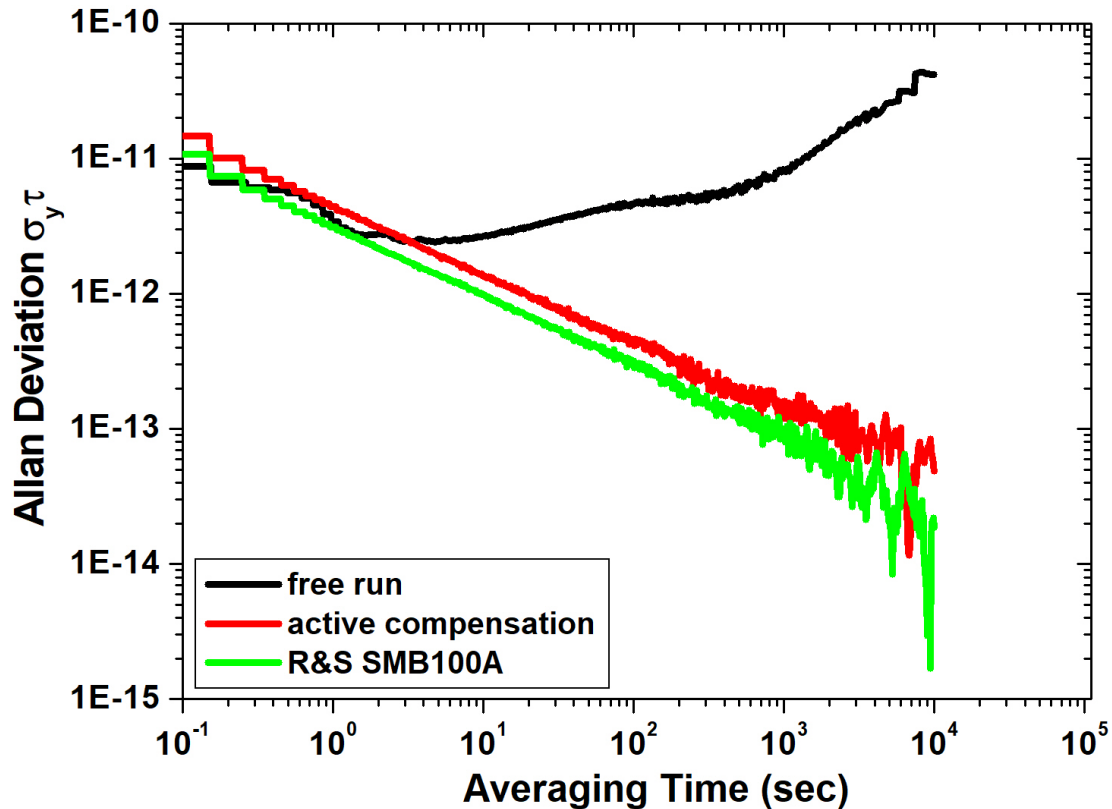


Figure 9.14: Experimental results of the measured frequency stability results. The black line shows the measured frequency stability of the dissemination system without compensation. The green line shows the stability result of the R&S SMB 100A phase locked to a Rb atomic clock. The red line represents the measured frequency stability of the dissemination system with active compensation.

atomic clock, as shown in Figure 9.6. As mentioned previously, the frequency stability measurements illustratively shown in Figure 9.14 were achieved using the R&S ESA together with the computer based R&S Allan variance software. The frequency stability of the 4 GHz signal was analyzed with a frequency counter resolution setting of 100 mHz. The green line in Figure 9.14 shows the very best, back-to-back stability performance of the R&S SMB 100A before being introduced to the VCSEL.

The black line as illustrated in Figure 9.14 represents instability of the 26 km free running optical fibre dissemination system. Short and long term frequency stabilities of 3.39791×10^{-12} after a 1 s integration time and 8.14848×10^{-12} after a 10^3 s integration time was experimentally measured, respectively. The red line illustratively shown in Figure 9.14 represents the stability of the dither controlled VCSEL phase compensation system activated. This result experimentally demonstrates that the

relative frequency stabilities were reduced to 4.43902×10^{-12} at 1 s and 1.62055×10^{-13} at 10^3 s respectively. The Allan variance result characterized by the red line shows that the frequency instability was further reduced to 4.86137×10^{-14} at 10^4 s. This result infers that during active compensation, the transmitting unit comprising of the R&S SMB100A signal generator and the VCSEL combined, was phase locked to the stable Rb atomic clock. A comparative analysis between the red and black lines given in Figure 9.14 clearly shows that the frequency stability of the disseminated optical signal improved through active compensation. Furthermore, it is evident that the phase noise of the compensated frequency dissemination system is smaller than that of the free running fibre link. The red Allan variance curve given in Figure 9.14 suggests that the residual noise introduced to the dissemination system is predominantly classified as white phase noise. The noise mechanisms associated to the black Allan deviation curve in Figure 9.14 may be related to white phase noise, flicker frequency noise and random walk frequency noise. A tabulated summary of the Allan deviation performance at periodic integration times for the results presented in Figure 9.14 is given in Table 9.2.

Table 9.2: Experimental Allan variance results.

	Free run	Active compensation
Ave. Time (sec)	Allan Deviation	Allan Deviation
1 s	3.39791×10^{-12}	4.43902×10^{-12}
10 s	2.6574×10^{-12}	1.35633×10^{-12}
100 s	4.62751×10^{-12}	4.12653×10^{-13}
1000 s	8.14848×10^{-12}	1.62055×10^{-13}
10000 s	4.18939×10^{-11}	4.86137×10^{-14}

Although the VCSEL based time and frequency compensation scheme as shown in Figure 9.6 proved to be effective, however the system suffers from some operational limitations. The VCSEL displays temporal drift and frequency chirping during modulation, which may affect the stability and accuracy of the transmitted signal along the fibre. However, there are mechanisms in place to reduce the drifting property of the VCSEL. One such technique involves temperature controlling the

VCSEL. Several techniques for reducing and limiting the chirping effect have been reported. These may involve injection locking and filtering thereby narrowing the spectrum (Gibbon et al., 2011, p. 41-45). One of the main drawbacks of dither gradient-based algorithm is its slow convergence speed. For complex search algorithms such as the one described in Section 9.2, much time is inefficiently consumed dithering each individual incoming control voltage before determining best direction and step to take. The benefits of the system described in this chapter are as follows, it reduces the design complexities and costs since there is no need to include additional components to achieve compensation. These may include fibre stretchers, acousto optic modulators (AOM's) and phase lock loop circuits. Furthermore, the noise contribution from additional components is reduced.

9.7 Summary

The time and frequency dissemination experiment presented and described in this chapter is, to my knowledge, the first such experimental demonstration at NMU Centre for Broadband Communication. Active phase compensation was experimentally achieved using the low cost and power efficient 1310 nm VCSEL optical source. The initial experimental results show that the measured error voltage remains minimized and constant over a five-hour period, while the compensation system was activated. The results further demonstrated that majority of the dither iterations that induced the phase compensation took approximately 0.15 s. Frequency stabilities of $3.09251 \times 10^{-12}/1$ s and $4.20288 \times 10^{-12}/10^3$ s were experimentally recorded when the R&S SMB100A signal generator was not phase locked to the Rb atomic clock. After phase locking the R&S SMB100A waveform generator to the Rb source, short and long-term frequency stabilities of $3.14085 \times 10^{-12}/1$ s and $1.01619 \times 10^{-13}/10^3$ s were experimentally measured. Instabilities of 3.39791×10^{-12} at 1 s and 8.14848×10^{-12} at 10^3 s were demonstrated for the free running fibre link, whereas frequency stabilities of 4.43902×10^{-12} at 1 s and 1.62055×10^{-13} at 10^3 s were measured during active compensation.

CHAPTER 10

CONCLUSION

Optical fibre plays a major role in the SKA telescope project, both in transporting huge amounts of astronomical data and in the dissemination of highly accurate and stable clock signals. Telescope array networks and conventional telecommunication networks share several key similarities and differences. Thoughtful design and technology selection is therefore essential in meeting the unique requirements of SKA astronomical telescope. The design and implementation of a precise and continuous time and frequency dissemination network in the laboratory test-bed has been demonstrated at the Centre for Broadband Communication laboratory, at Nelson Mandela University (NMU). Through thorough reviewing and studying of the related and relevant literature and embarking on various experimental works, this research has laid the foundation for future phase noise compensation research at the NMU.

In terms of the experimental finding presented in this PhD thesis, Chapter 6 contains numerous experimental results pertaining to optical fibre pulse-per-second (PPS) latency measurements along a round-trip dissemination link. This work is based on a high speed all optical VCSEL wavelength conversion and switching, by PPS optical injection within the 1550 nm transmission window. By using a 1551.70 nm injection beam from a DFB laser source, wavelength switching to 1553.30 nm occurred. This was realized by using a slave VCSEL with a wavelength tunability of 3.5 nm (437.5 GHz). A round-trip latency time of 113.2 μ s was experimentally measured along a 22 km fibre link. The velocity of the disseminated optical PPS signal along the fibre transmission path was found to be 1.944×10^8 m/s. These results highlight the urgent need for a time delay or phase drift compensation strategy.

The design and operational features of a fast switching phase correction system was explored in Chapter 7. A simulation was conducted to investigate the influence of temperature on the fibre length. The simulation results presented in this chapter suggests that a 2 km deployed fibre experiences a 28 mm optical fibre path length expansion, whereas a 20 km fibre link experiences a 280 mm change in optical fibre

path length, assuming a 2°C temperature change. These results highlight the urgent need for active phase compensation within the SKA since a 1 km fibre, buried at a 1 m depth experiences 35 mm change in the optical transmissions length, due to a 5°C temperature variation. Experimental results further showed that a + 0.1 mA change in the bias current corresponds to a 0.1 nm wavelength shift. Moreover, a – 0.1 mA change in the bias current of the VCSELs used corresponds to a 0.05 nm wavelength shift. Chapter 7 concludes by highlighting the stringent clock tone stability requirements at the respective SKA observational frequencies.

Chapter 8 presented the first experimental demonstration of an electrical error signal needed for feedback control of the VCSEL phase correction actuator. The error signal was generated using a RF frequency mixing technique. Section 8.3.2 showed that the error signal was minimized at -78.3 mV, -105.3 mV, -74.4 mV and -94.7 mV corresponding to a zero phase difference between the reference and transmitted sinusoidal waveforms. In Section 8.4 a proof of concept for using a VCSEL phase correction actuator for phase noise compensation was presented. A DFB laser was used as the actuator because it has similar wavelength tunability properties as a VCSEL. Compensation along the G.652 fibre link was achieved by taking advantage of the inherent chromatic dispersion properties as well as the tunability property of the DFB laser.

Chapter 9 presented the first ever dissemination of high precision timing signals across a 26 km G.655 optical fibre link at NMU. Performance analysis of the dither controlled phase correction actuator was experimentally demonstrated. The dither control algorithm was designed and compiled by the author. The result showed that the error voltage remains minimized and constant over the entire five-hour period for which the phase noise compensation system was activated. A -88.5 mV error voltage was experimentally recorded corresponding to zero phase difference between the transmitted and reference signal. Further experimental results showed that majority of the dither iterations that induced the phase compensation took approximately 0.15 s. Fractional frequency stabilities of $3.09251 \times 10^{-12}/1$ s and $4.20288 \times 10^{-12}/10^3$ s were experimentally recorded when the R&S SMB100A signal generator was not phase locked to the Rb atomic clock. When the R&S SMB100A signal generator was phase

locked to the Rb source, short and long-term frequency stabilities of $3.14085 \times 10^{-12}/1$ s and $1.01619 \times 10^{-13}/10^3$ s were experimentally measured. Further testing yielded instabilities of 3.39791×10^{-12} at 1 s and 8.14848×10^{-12} at 10^3 s when the fibre link was running freely. However, frequency stabilities of 4.43902×10^{-12} at 1 s and 1.62055×10^{-13} at 10^3 s were measured during active compensation.

APPENDIX A

Research outputs in journals, peer reviewed conferences and books of abstracts

Published/accepted/presented articles

2017:

- 1) G. M. Isoe, **S. Wassin**, R. Gamatham, A. Leitch, and T. Gibbon, "Capacity upgrade in short-reach optical fibre networks: simultaneous 4-PAM 20 Gbps data and polarization-modulated PPS clock signal using a single VCSEL carrier," *Journal of Modern Optics*, vol. 64, (20), pp. 2245-2254, 2017.
- 2) G. M. Isoe, **S. Wassin**, R. R. G. Gamatham, A. W. R. Leitch, and T. B. Gibbon, "A high capacity data Centre network: Simultaneous 4-PAM data at 20 Gbps and 2 GHz phase modulated RF clock signal over a single VCSEL carrier," *Journal of Modern Optics*, vol. 64, (21), pp. 2336-2344, 2017.
- 3) G. M. Isoe, **S. Wassin**, R. R. G. Gamatham, A. W. R. Leitch, and T. B. Gibbon, "Simultaneous 10 Gbps data and polarization-based pulse-per-second clock transmission using a single VCSEL for high-speed optical fibre access networks," *Proc. SPIE 10129, Optical Metro Networks and Short-Haul Systems IX*, 101290F (January 28, 2017); doi:10.1117/12.2252230, pp. 101290F-101290F-12.
- 4) **S. Wassin**, G. M. Isoe, R. R. G. Gamatham, A. W. R. Leitch, and T. B. Gibbon, "Highly accurate pulse-per-second timing distribution over optical fibre network using VCSEL side-mode injection," *Proc. SPIE. 10129, Optical Metro Networks and Short-Haul Systems IX*, 101290G. (January 28, 2017) doi: 10.1117/12.2252069, pp. 101290G-101290G-12.
- 5) G. M. Isoe, **S. Wassin**, R. R. G. Gamatham, A. W. R. Leitch, and T. B. Gibbon, "High Capacity Data Centre Network: Simultaneous 4-PAM Data at 20 Gbps and 2 GHz Phase Modulated RF Clock Signal over a Single VCSEL Carrier," *The annual 2017 Southern African Telecommunication Networks and Application Conference (SATNAC) 3rd – 10th September 2017 on the Freedom of the Seas Cruise Liner, Royal Caribbean International, Barcelona, Spain*, pp. 148-153.

- 6) **S. Wassin**, G. M. Isoe, R. R. G. Gamatham, A. W. R. Leitch, and T. B. Gibbon, "Fibre-Based Time and Frequency Distribution using a DFB Phase Error Correction Actuator," The annual 2017 Southern African Telecommunication Networks and Application Conference (SATNAC) 3rd – 10th September 2017 on the Freedom of the Seas Cruise Liner, Royal Caribbean International, Barcelona, Spain, pp. 154-157.
- 7) G. M. Isoe, **S. Wassin**, R. R. G. Gamatham, A. W. R. Leitch, and T. B. Gibbon, "Transmission performance of 10 Gbps OOK, 15 Gbps 2-PAM and 20 Gbps 4-PAM data signals over 11 km using a 1310 nm VCSEL," the 62nd annual conference of the South Africa Institute of Physics (SAIP), Stellenbosch University, 3rd – 7th July 2017.
- 8) **S. Wassin**, "VCSEL-Based Time and Frequency Dissemination System Across Optical Fibre, SKA Bursary Conference, Strand Hotel, Cape Town, 2017.
- 9) **S. Wassin**, G. M. Isoe, R. R. G. Gamatham, A. W. R. Leitch, and T. B. Gibbon, "Towards the Development of VCSEL-Based Time and Frequency Dissemination System using a DFB Phase Error Correction Actuator for the SKA," the 62nd annual conference of the South Africa Institute of Physics (SAIP), Stellenbosch University, 3rd – 7th July 2017.
- 10) **S. Wassin**, G. M. Isoe, R. R. G. Gamatham, A. W. R. Leitch, and T. B. Gibbon, "Application of VCSELs in Next-Generation Telescope Array Networks such as the Square Kilometre Array," Journal: Optics and Laser Technology, 2017, In Press.

2016:

- 1) G. M. Isoe, **S. Wassin**, D. Kiboi Boiyo, E. K. Rotich Kipnoo, R.R.G. Gamatham, A.W.R. Leitch and T. B. Gibbon, "Effect of 10 Gbps Data Transmission on 1.712 GHz 1309.97 nm VCSEL Based Radio Frequency Distribution over a Single Optical Fibre for the Telescope Array," The annual 2016 Southern African Telecommunication Networks and Application Conference (SATNAC) 4th to 7th September 2016 at Fancourt in George, Western Cape, South Africa, pp. 150-153, ISBN: 978-0-620-72418-0.
- 2) **S. Wassin**, G. M. Isoe, R. R. G. Gamatham, A. W. R. Leitch, T. B. Gibbon, "Component Power Budget Analysis and VCSEL Characterization for the Square Kilometre Array Signal and Data Transport Network," The annual 2016 Southern African Telecommunication Networks and Application Conference (SATNAC) 4th to

7th September 2016 at Fancourt in George, Western Cape, South Africa pp. 154-159, ISBN: 978-0-620-72418-0.

- 3) K. J. Leburu, G. M. Isoe, **S. Wassin**, D. Kiboi Boiyo, R.R.G. Gamatham, A.W.R. Leitch and T. B. Gibbon, "Transmission of Pulse per Second Clock Tone Signals in Optical Communication Systems over Optical Fibre and Free Space," The annual 2016 Southern African Telecommunication Networks and Application Conference (SATNAC) 4th to 7th September 2016 at Fancourt in George, Western Cape, South Africa.
- 4) G. M. Isoe, D. K. Boiyo, **S. Wassin**, R. R. G. Gamatham, A.W. R. Leitch and T. B. Gibbon, "Effect of 1.712 GHz RF-Clock Signal Distribution on 10 Gbps 1550.89 nm VCSEL Based Transmission over Single Optical Fibre for Square Kilometre Telescope Array," 61 South African Institute of Physics (SAIP) 2016 Conference, university of cape town, South Africa, 04-08 July 2016.
- 5) D. K. Boiyo, G. M. Isoe, **S. Wassin**, E. K. Rotich Kipnoo, R. R. G. Gamatham, A.W. R. Leitch and T. B. Gibbon, "Characterization and Compensation of Fibre Link Dispersion in a 10 Gb/s Flexible Network," 61 South African Institute of Physics (SAIP) 2016 Conference, university of cape town, South Africa, 04-July 8, 2016.
- 6) **S. Wassin**, G. M. Isoe, D. K. Boiyo, R. R. G. Gamatham, A.W. R. Leitch and T. B. Gibbon, "Power Budget Analysis of Passive Components along an Optical Fibre Link of a Frequency Dissemination System within the MeerKAT Telescope Array," 61 South African Institute of Physics (SAIP) 2016 Conference, university of cape town, South Africa, 04-July 8, 2016.
- 7) K. J. Leburu, G. M. Isoe, D. K. Boiyo, **S. Wassin**, R. R. G. Gamatham, A.W. R. Leitch and T. B. Gibbon, "Advantages of Free Space Optics over Optical Fibre for Clock Tone Distribution in a 2.5 GHz Transmission Link," 61 South African Institute of Physics (SAIP) 2016 Conference, university of cape town, South Africa, 04-July 8, 2016.
- 8) D. Kiboi Boiyo, G. M. Isoe, **S. Wassin**, E. K. Rotich Kipnoo, R. R. Gamatham, A. W. R. Leitch and T. B. Gibbon, "An all Optical VCSEL Wavelength Conversion for Optical Fibre Access Networks," Proceedings of 2016 international conference on Sustainable Research and innovation (SRI), Vol. 7, ISSN: 2079-6226, pp. 17-20, May 2016.
- 9) **S. Wassin**, G. M. Isoe, D. Kiboi Boiyo, R. R. Gamatham, A. W. R. Leitch and T. B. Gibbon, "The Square Kilometre Array: The Notion of Timing and Synchronization,"

Proceedings of 2016 international conference on Sustainable Research and innovation (SRI), Vol. 7, ISSN: 2079-6226, pp. 52-55, May 2016.

- 11) S. Wassin, "Pulse-Per-Second Timing Dissemination within the SKA Fibre Network," SKA Bursary Conference, Protea Fire & Ice Hotel, Cape Town, 2016.

2015:

- 1) **S. Wassin**, R. R. G. Gamatham, A. W. R. Leitch and T. B. Gibbon, "Time and frequency dissemination system using VCSELs, across an optical fibre network within the Square Kilometre Array," SKA SA-HCD 2015 Postgraduate Bursary Conference, Stellenbosch, Cape Town, 30th Nov- 8th Dec 2015.
- 2) **S. Wassin**, E. K. Rotich, R. R. G. Gamatham, A.W. R. Leitch and T. B. Gibbon, "Active phase correction using a VCSEL for clock tones transmitted along a 24 km optical fibre link," 60th South African Institute of Physics (SAIP) 2014 Conference, board work conference centre, eastern cape, South Africa.

REFERENCES

1. **Abidi**, A. A., & Meyer, R. G. (1983). Noise in relaxation oscillators. *IEEE Journal of Solid-State Circuits*, SC-18 (6), 794-802.
2. **Agilent Technolgies**. (2012). *Agilent 86142B Optical Spectrum Analyzer-Technical Overview*. [Specification sheet].
3. **Agrawal**, G. P. (2007). *Nonlinear fiber optics*. Burlington, Massachusetts: Academic Press.
4. **Agrawal**, G. P. (2012). *Fiber-optic communication systems*. New York: John Wiley & Sons.
5. **Allan**, D. W. (1966). The statistics of atomic frequency standards. *Proceedings of IEEE*, 54 (2), 221-230.
6. **Allan**, D. W. (1987) Should classical variance be used as a basic measure in standards metrology?. *IEEE Transactions*, IM-36 (2), 646-654.
7. **Analog Devices**. (2009). *Fundamentals of Phase Locked Loops (PLLs)* [Information Sheet]. Norwood, Massachusetts: Analog Devices.
8. **Australia Telescope National Facility (ATNF)**. (2015). Retrieved August 3, 2017 from <http://www.atnf.csiro.au/projects/askap/index.html>.
9. **Baghdady**, E. J., Lincoln, R. N., & Nelin, B. D. (1965). Short-term frequency stability: Characterization, theory, and measurement. *Proceedings of IEEE*, 53 (7), 704-722.
10. **Baran**, O., & Kasal, M. (2009). Allan Variances Calculation and Simulation. *IEEE 19th International Conference Radioelektronika, April, 2009, Slovakia*, 1-4.

11. **Barnes, J. A.**, Chi, A.R., Cutler, L.S., Healey, D.J., Leeson, D.B., McGunigal, T.E., *et al.* (1971). Characterization of frequency stability. *IEEE Transactions on Instrumentation and Measurement*, 20 (2), 105-120.
12. **Beck, A.**, & Teboulle, M. (2009). Gradient-based algorithms with applications to signal recovery. In *Convex optimization in signal processing and communications* (pp. 42-88). Cambridge University Press: New York.
13. **Beck, R.**, & Gaensler, B. M. (2004). Observations of magnetic fields in the Milky Way and in nearby galaxies with a Square Kilometre Array. *New Astronomy Reviews*, 48 (11-12), 1289–1304.
14. **Behrendt, K.**, & Fodero, K. (2006). The perfect time: An examination of time-synchronization techniques. In *Proc. 33rd Annual West. Prot. Rel. Conference*, (pp. 17-19), Washington, USA.
15. **Bercy, A.**, Stefani, F., Lopez, O., Chardonnet, C., Pottie, P. E., & Amy-Klein, A. (2014). Two-way optical frequency comparisons at 5×10^{-21} relative stability over 100-km telecommunication network fibers. *Physical Review A*, 90 (6), 061802.
16. **Bogatyrev, V. A.**, Bubnov, M. M., Dianov, E. M., Kurkov, A. S., Mamyshev, P. V., Prokhorov, A. M., ... & Chernikov, S. V. (1991). A Single-Mode Fiber with Chromatic Dispersion Varying Along the Length. *Journal of Lightwave Technology*, 9(5), 561-566.
17. **Boiyo, D. K.** (2017). *Optimization of Flexible Spectrum in Optical Transport Networks*. Unpublished doctoral thesis, Nelson Mandela Metropolitan University, Port Elizabeth, South Africa.
18. **Boiyo, D. K.**, Chabata, T. V., Rotich Kipnoo, E. K., Gamatham, R. R., Leitch, A. W. R., & Gibbon, T. B. (2016). Reconfigurable high-speed optical fibre networks: Optical wavelength conversion and switching using VCSELs to eliminate channel collisions,” *Optical Fiber Technology*, 33, 30-35.

19. **Boiyo**, D. K., Isoe, G. M., Wassin, S., Kipnoo, E. K. R., Gamatham, R. R., Leitch, A. W. R., & Gibbon, T. B. (2016). An all Optical VCSEL Wavelength Conversion for Optical Fibre Access Networks. *Conference Proceedings of Sustainable Research and Innovation, May, 2016, Kenya*, 17-20.
20. **Bregni**, S. (1997). Clock Stability Characterization and Measurement in Telecommunications. *IEEE Transactions on Instrumentation and Measurement*, 46 (6), 1284-1294.
21. **Bureau International des Poids et Mesures (BIPM)**. (2014). *The International System of Units, 8th Edition*. France: BIPM.
22. **Calhoun**, M., Sydnor, R., & Diener, W. (2002). A stabilized 100-megahertz and 1-gigahertz reference frequency distribution for Cassini radio science. *IPN Progress Report*, 42 (148), 1-11.
23. **Camparo**, J. (2007). The rubidium atomic clock and basic research. *American Institute of Physics*, 33-39. Retrieved 04 September 2017, from http://www-meg.phys.cmu.edu/physics_33340/experiments/PhysicsToday_11-07_AtomicClock.pdf.
24. **Carilli**, C. L., Furlanetto, S., Briggs, F., Jarvis, M., Rawlings, S., & Falcke, H. (2004). Probing the dark ages with the Square Kilometer Array. *New Astronomy Reviews*, 48, 1029-1038.
25. **Carilli**, C., & Rawlings, S. (Eds.). (2004). Science with the Square Kilometer Array: motivation, key science projects, standards and assumptions. *New Astronomy Reviews*, 48, 979–984.
26. **Chang**, C. H., Chrostowski, L., Chang-Hasnain, C. J., & Chow, W. W. (2002). Study of long-wavelength VCSEL-VCSEL injection locking for 2.5-Gb/s transmission, *IEEE Photonics Technology Letters*, 14 (11), 1635-1637.

27. **Clivati**, C., Ambrosini, R., Artz, T., Bertarini, A., Bortolotti, C., Frittelli, M., ... & Negusini, M. (2017). A VLBI experiment using a remote atomic clock via a coherent fibre link. *Scientific Reports*, 7, 40992.
28. **Cordes**, J. M., Kramer, M., Lazio, T. J. W., Stappers, B. W., Backer, D. C., & Johnston, S. (2004). Pulsars as Tools for Fundamental Physics & Astrophysics. *New Astronomy Reviews*, 48, 1413–1438.
29. **Damour**, T. & Esposito-Farese, G. (1998). Gravitational-wave versus binary-pulsar tests of strong-field gravity. *Physics Review D*, 58 (4), 042001.
30. **Danielsen**, S. L., Mikkelsen, B., Hansen, P. B., Poulsen, H. N., Kloch, A., & Stubkjaer, K. E. (1997). Wavelength conversion techniques and devices. *Conference: Lasers and Electro-Optics Society Annual Meeting, December 1997, 1*, 94-95.
31. **Daussy**, C., Lopez, O., Amy-Klein, A., Goncharov, A., Guinet, M., Chardonnet, C., ... & Clairon, A. (2005). Long-distance frequency dissemination with a resolution of 10^{-17} . *Physical Review Letters*, 94 (20), 203904-1-203904-4.
32. **Dawkins**, S., McFerran, J., & Luiten, A. (2007). Considerations on the measurement of the stability of oscillators with frequency counters. *IEEE Transactions on Ultrasonics, Ferroelectrics and Frequency Control*, 54 (5), 918 –925.
33. **Dewdney**, P. E., Hall, D., McCool, R., Roddis, N., Turner, W., Gunst, A. UCAM, &CSIRO. (2011). *SKA1: HIGH LEVEL SYSTEM DESCRIPTION*. Retrieved October 14, 2017, from https://www.skatelescope.org/public/201102_System_delta_CoDR_Document/Presentations/S3P1-Dewdney_SKA1_highlevel_description_v2.pdf
34. **Dewdney**, P. E., Hall, P. J., Schilizzi, R. T., & Lazio, T. J. L. W. (2009). The Square Kilometre Array. *Proceedings of the IEEE*, 97 (8), 1482-1496.

35. **Dickstein**, L. (2012). Introduction to Phase Noise in Signal Generators. Retrieved July 23, 2017 from <http://www.gigatronics.com/RequestForm/Phase-Noise-Whitepaper-Request-Form.html>.
36. **Dong**, J. W., Wang, B., Gao, C., Guo, Y. C., & Wang, L. J. (2016). Highly accurate fiber transfer delay measurement with large dynamic range. *Optics Express*, 24 (2), 1368-1375.
37. **Durhuus**, T., Mikkelsen, B., Joergensen, C., Danielsen, S., L., & Stubkjaer, K. (1996). All-Optical Wavelength Conversion by Semiconductor Optical Amplifiers. *Journal of Lightwave Technology*, 14 (6). 942-954.
38. **Epstein**, B. R., Olsson, R. H., & Rotman, R. (2016). Phased Array Technologies. *Proceedings of IEEE*, 104 (3), 482-486.
39. **Essen**, L., & Parry, J. V. L. (1955). An Atomic Standard of Frequency and Time Interval: A Cæsium Resonator. *Nature*, 176, 280-282.
40. **Fan**, L., Wu, M. C., Lee, H. C., & Grodzinski, P. (1994). 10.1 nm range continuous wavelength-tunable vertical-cavity surface-emitting lasers. *Electronics Letters*, 30 (17), 1409-1410.
41. **Foreman**, S. M., Ludlow, A. D., de Miranda, M. H., Stalnaker, J. E., Diddams, S. A., & Ye, J. (2007). Coherent optical phase transfer over a 32-km fiber with 1 s instability at 10⁻¹⁷. *Physical Review Letters*, 99 (15), 153601.
42. **Fujieda**, M., Kumagai, M., Gotoh, T., & Hosokawa, M. (2009). Ultrastable frequency dissemination via optical fiber at NICT. *IEEE Transactions on Instrumentation and Measurement*, 58 (4), 1223-1228.

43. **Fujieda**, M., Kumagai, M., Nagano, S., Yamaguchi, A., Hachisu, H., & Ido, T. (2011). All-optical link for direct comparison of distant optical clocks. *Optics Express*, *19* (17), 16498-16507.
44. **Gaensler**, B. M., Beck, R., & Feretti, L. (2004). The origin and evolution of cosmic magnetism. *New Astronomy Reviews*, *48*, 1003–1012.
45. **Gao**, S., Li, Z., Xie, Y., Liu, Q., Zhang, X., Shi, Y., & He, S. (2010). All-Optical Wavelength Conversion Based on Four-Wave Mixing in Silicon Waveguides. *The 9th International Conference on Optical Communications and Networks (ICOON2010)*, October, 2010, China, 195-200.
46. **Gardner**, F. M. (1979). *Phaselock Techniques*. New Jersey: John Wiley & Sons.
47. **Garrington**, S., Spencer, R., Shenton, C., Bentley, M., & McCool, R. (2011). Concept Description for Synchronisation & Timing For The SKA. Retrieved August 14, 2017 from https://www.skatelescope.org/public/2011-06-28_Signal_Transport_and_Networks_CoDR/CoDR_reviewdocuments/15_WP_2-030.070.000-TD-001v.1%20SynchandTime.pdf.
48. **Gibbon**, T. B. et al. (2015). Fiber-to-the-telescope: MeerKAT, the South African precursor to Square Kilometre Telescope Array. *Journal of Astronomical Telescopes, Instruments, and Systems*, *1* (2), 028001.
49. **Gibbon**, T. B., Prince, K., Pham, T. T., Tatarczak, A., Neumejr, C., Rönneberg, E., ... & Monroy, I. T. (2011). VCSEL transmission at 10Gb/s for 20km single mode fiber WDM-PON without dispersion compensation or injection locking. *Optical fiber technology*, *17* (1), 41-45.
50. **Goldenberg**, H. M., Kleppner, D., & Ramsey, N. F. (1960). Atomic hydrogen maser. *Physical Review Letters*, *5* (8), 361-362.

51. **Gollapalli**, R. P., & Duan, L. (2010). Atmospheric timing transfer using a femtosecond frequency comb. *IEEE Photonics Journal*, 2 (6), 904-910.
52. **Gomis-Bellmunt**, O., & Campanile, L. F. (2010). Actuator Design Analysis. In *Design Rules for Actuators in Active Mechanical Systems* (29-78). London: Springer
53. **Gordon**, J. P., & Kogelnik, H. (2000). PMD fundamentals: Polarization mode dispersion in optical fibers. *Proceedings of the National Academy of Sciences*, 97 (9), 4541-4550.
54. **Grainge**, K. et al. (2017). Square Kilometre Array: The Radio Telescope of the XXI Century. *Astronomy Reports*, 61 (4), 288–296.
55. **Greenhall**, C. A. (1998). Spectral ambiguity of Allan variance. *IEEE Transactions on Instrumentation and Measurement*, 47 (3), 623-627.
56. **Grosche**, G., Terra, O., Predehl, K., Holzwarth, R., Lipphardt, B., Vogt, F., ... & Schnatz, H. (2009). Optical frequency transfer via 146 km fiber link with 10^{-19} relative accuracy. *Optics Letters*, 34 (15), 2270-2272.
57. **Hajimiri**, A., & Lee, T. H. (1998). A General Theory of Phase Noise in Electrical Oscillators. *IEEE Journal of Solid-State Circuits*, 33 (2), 179-194.
58. **Hall**, P. J., Schilizzi, R.T., Dewdney, P. E. F., & Lazio, T. J. W. (2008). The Square Kilometer Array (SKA) Radio Telescope: Progress and Technical Directions. *Radio Science Bulletin*, 326, 4-19.
59. **Harder**, C., Vahala, K., & Yariv, A. (1983). Measurement of the linewidth enhancement factor-alpha of semiconductor lasers. *Applied Physics Letters*, 42 (4), 328–330.

60. **Heismann**, F. (1998). Tutorial: Polarization mode dispersion: Fundamentals and impact on optical communication systems. *24th European Conference on Optical Communication (ECOC), September, 1998*, 2, p. 51-79.
61. **Hellwig**, H. W. (1975). Atomic frequency standards: A survey. *Proceedings of IEEE*, 63 (2), 212-228.
62. **Holman**, K. W., Jones, D. J., Hudson, D. D., & Ye, J. (2004). Precise frequency transfer through a fiber network by use of 1.5- μm mode-locked sources. *Optics Letters*, 29 (13), 1554-1556.
63. **Hou**, D., Li, P., Liu, C., Zhao, J., & Zhang, Z. (2011). Long-term stable frequency transfer over an urban fiber link using microwave phase stabilization. *Optics express*, 19 (2), 506-511.
64. **Howe**, D. A. (2005). Frequency Stability. In *Encyclopedia of RF and Microwave Engineering* (pp. 1706-1720). New Jersey: John Wiley & Sons, Inc.
65. **Howe**, D. A., & Walls, F. L. (1983). A compact hydrogen maser with exceptional long-term stability. *IEEE Transactions on Instrumentation and Measurement*, 32 (1), 218-223.
66. **Howe**, D. A., Allan, D. W., & Barnes, J., A. (1981). Properties of Oscillator Signals and Measurement Methods. *Proceedings of the 35th Annual Symposium on Frequency Control*. 1-47.
67. **Huttner**, B., Gisin, B., & Gisin, N. (1999). Distributed PMD Measurements with a Polarization-OTDR in Optical Fibers. *IEEE Journal of Lightwave Technology*, 17 (10), 1843-1848.
68. **Huynh**, M. T. & Lazio, J. (2013). An Overview of the Square Kilometre Array. <https://arxiv.org/abs/1311.4288>, 1-13.

69. **Idachaba**, F., Ike, D. U., & Hope, O. (2014, July). Future trends in fiber optics communication. In *Proceedings of the World Congress on Engineering* (Vol. 1, pp. 438-442).
70. **Integrated Device Technology (IDT)**, Inc. (2014). *Jitter Specifications for Timing Signals* [Application Note]. San Jos.
71. **International Organization for Standardization (ISO)**. (2012). International vocabulary of metrology — Basic and general concepts and associated terms. Retrieved July 23, 2017 from <https://www.iso.org/obp/ui/#iso:std:iso-iec:guide:99:ed-1:v2:en>.
72. **International Telecommunication Union-ITU**. (2012). *G.694.1-Spectral grids for WDM applications: DWDM frequency grid*. Geneva, Switzerland, 1-7.
73. **Ito**, H., Hosokawa, M., Umezu, J., Morikawa, T., Tsuda, M., Takahei, K., Uehara M., & Mori, K. (2003). 3-4 Hydrogen Maser. *Journal of the National Institute of Information and Communications Technology*, 50 (1/2), 85-94.
74. **ITU-T, International Telecommunication Union**. (2009). *Characteristics of a single-mode optical fibre and cable, Recommendation ITU-T G.652* [Information Sheet]. Geneva, Switzerland.
75. **ITU-T, International Telecommunication Union**. (2009). *Characteristics of a non-zero dispersion-shifted single-mode optical fibre and cable, Recommendation ITU-T G.655* [Information Sheet]. Geneva, Switzerland.
76. **Jiang**, H., Kéfélian, F., Crane, S., Lopez, O., Lours, M., Millo, J., ... & Santarelli, G. (2008). Long-distance frequency transfer over an urban fiber link using optical phase stabilization. *Journal of the Optical Society of America B*, 25 (12), 2029-2035.

77. **Kaur**, A., Singh, K., & Utreja, B. (2013). Wavelength Converters in Optical Communication Systems. *Engineering Science and Technology: An International Journal (ESTIJ)*, 3 (2), 338-344.
78. **Kazovsky**, L. G., Cheng, N., Shaw, W., Gutierrez, D., & Wong, S. (2011). *Broadband Optical Access Networks*. New York: John Wiley & Sons, Inc.
79. **Keiser**, G. (2000). *Optical Fiber Communications*. 3rd ed. New York: McGraw-Hill Companies.
80. **Kim**, K. Y. (Eds.). (2010). *Advances in Optical and Photonic Devices*. Croatia: INTECH.
81. **Kipnoo**, E. K. R., Kourouma, H., Waswa, D., Leitch, A. W. R., & Gibbon, T. B. (2012). Analysis of VCSEL transmission for the square kilometre array (SKA) in South Africa. In *Proceedings of the Southern Africa Telecommunication Networks and Applications Conference (SATNAC)*, George, South Africa (pp. 483-484).
82. **Kipnoo**, E. K. R., Waswa, D., Leitch, A. W. R., & Gibbon, T. B. (2012). VCSEL Technology for Square Kilometre Array (SKA) Optical Fibre Network. In *Proceeding of SAIP2012: The 57th Annual Conference of the South African Institute of Physics*, Pretoria, South Africa: University of Pretoria (pp. 523-527)
83. **Koch**, T. L., & Linke, R. A. (1986). Effects of nonlinear gain reduction on semiconductor wavelength chirping. *Applied Physics Letters*, 48, 613–616.
84. **Kourogi**, M., Nakagawa, K., & Ohtsu, M. (1993). Wide-span optical frequency comb generator for accurate optical frequency difference measurement. *IEEE Journal of Quantum Electronics*, 29, 2693-2701.

85. **Kramer**, M., Backer, D. C., Cordes, J. M., Lazio, T. J. W., Stappers, B. W., & Johnston, S. (2004). Strong-field tests of gravity using pulsars and black holes. *New Astronomy Reviews*, 48, 993-1002.
86. **Lacey**, J. P. R., Pendock, G. J., & Tucker, R. S. (1996). Gigabit-per-second all-optical 1300-nm to 1550-nm wavelength conversion using cross-phase modulation in a semiconductor optical amplifier. *Optical Fiber Communication (OFC) Conference, February, 1996*, 2, 125-126.
87. **Land**, D. V., Levick, A. P., & Hand, J. W. (2007). The use of the Allan deviation for the measurement of the noise and drift performance of microwave radiometers. *Measurement Science and Technology*, 18, 1917-1928.
88. **Lavrova**, O. A., Rau, L., & Blumenthal, D. J. (2002). 10-Gb/s Agile Wavelength Conversion With Nanosecond Tuning Times Using a Multisection Widely Tunable Laser. *Journal of Lightwave Technology*, 20 (4), 712-717.
89. **Lazio**, T. J. W., Tarter, J. C., & Wilner, D. J. (2004). The cradle of life. *New Astronomy Reviews*, 48, 985-991.
90. **Levine**, J. (1999). Introduction to time and frequency metrology. *Review of Scientific Instruments*, 70 (6), 2567-2596.
91. **Lewis**, L. L. (1991). An introduction to frequency standards. *Proceedings of IEEE*, 79 (7), 927-935.
92. **Li**, S., Guo, R., Li, L., Shi, Y., Lu, J., Lu, L., Zheng, J., & Chen, X. (2014). Experimental demonstration of DFB semiconductor lasers with varying longitudinal parameters. *Optics Express*, 22 (4), 4059-4064.

93. **Li, S., Wang, C., Lu, H., & Zhao, J.** (2017). Performance evaluation at the remote site for RF frequency dissemination over fiber. *IEEE Photonics Journal*, 9 (3), 7202608
94. **Lombardi, M. A.** (2002). Fundamentals of Time and Frequency. In Bishop, R. H (Ed.), *The Mechatronics Handbook*. Florida, CRC Press.
95. **Lopez, O., Amy-Klein, A., Daussy, C., Chardonnet, C., Narbonneau, F., Lours, M., & Santarelli, G.** (2008). 86-km optical link with a resolution of 2×10^{-18} for RF frequency transfer. *The European Physical Journal D-Atomic, Molecular, Optical and Plasma Physics*, 48 (1), 35-41.
96. **Lorimer, D. R., & McLaughlin, M. A.** (2009). Probing fundamental physics with pulsars. *Proceedings of the International Astronomical Union*, 5 (H15), 131-136.
97. **Major, F. G.** (1998). *The quantum beat - The Physical Principles of Atomic Clocks*. New York: Springer.
98. **Marki, F. & Marki, C.** (2010). *Mixer Basics Primer, A Tutorial for RF & Microwave Mixers* [Information Sheet]. California: Marki Microwave, Inc.
99. **Marra, G.** (2013). *Transfer of Optical Frequency Combs Over Optical Fibre Links*. Unpublished doctoral thesis. University of Southampton, Southampton, United Kingdom.
100. **Marra, G., Margolis, H. S., & Richardson, D. J.** (2012). Dissemination of an optical frequency comb over fiber with 3×10^{-18} fractional accuracy. *Optics Express*, 20 (2), 1775-1782.
101. **Marra, G., Slavik, R., Margolis, H. S., Lea, S. N., Petropoulos, P., Richardson, D. J., & Gill, P.** (2011). High-resolution microwave frequency transfer over an 86-km-long optical fiber network using a mode-locked laser. *Optics Letters*, 36 (4), 511-513.

102. **Massa**, N. (2000). Fibre optic telecommunication. In *Fundamental of photonics*, (pp. 293-347). Connecticut: University of Connecticut.
103. **McCool**, R., Bentley, M., Argo, M. K., Spencer, R., & Garrington, S. (2008). Transfer of a 1486.3 MHz frequency standard over installed fibre links for local oscillator distribution with a stability of 1 picosecond. *Proceedings of ECOC, September 2008*, 1–2.
104. **Michalzik**, R. (Eds.). (2012). *VCSELS: fundamentals, technology and applications of vertical-cavity surface-emitting lasers*. Germany: Springer.
105. **Miura**, Y., Nakajima, J., Mizutani, K., & Sasaki, W. (2007). Compact and Inexpensive Frequency Stabilization Technique for 850nm Vertical Cavity Surface Emitting Lasers based on Fabry-Perrot Resonator. In *Proc. of SPIE Vol* (Vol. 6673, pp. 66730T-1).
106. **Mohammed**, E., S., & Radman, A., A. (2017). *Wavelength Conversion Technology*. Retrieved June 28, 2017, from http://www.academia.edu/4066054/Wavelength_Converter_Technology.
107. **Moreira**, P. M. O. F. (2014). *Timing Signals and Radio Frequency Distribution Using Ethernet Networks for High Energy Physics Applications*. Unpublished doctoral thesis. University College of London, London, England.
108. **Morgan**, D. K. (2003). *CD4046B Phase-Locked Loop: A Versatile Building Block for Micropower Digital and Analog Applications* [Application Report]. Dallas, Texas: Texas Instruments.
109. **Muller**, H., Peters, A., & Braxmaier, C. (2006). Optical fibers with interferometric path length stability by controlled heating for transmission of optical signals and as components in frequency standards. *Applied Physics B: Lasers and Optics*, 84 (3), 401-408.

110. **Musha**, M., Hong, F. L., Nakagawa, K. I., & Ueda, K. I. (2008). Coherent optical frequency transfer over 50-km physical distance using a 120-km-long installed telecom fiber network. *Optics Express*, *16*(21), 16459-16466.
111. **Musha**, M., Nakagawa, K. I., Ueda, K. I., & Hong, F. L. (2008). Precision optical carrier transmission over 110km through urban fiber network. *Proceedings of URSI General Assembly 2008*, A02.
112. **Narbonneau**, F., Lours, M., Bize, S., Clairon, A., Santarelli, G., Lopez, O., ... & Chardonnet, C. (2006). High resolution frequency standard dissemination via optical fiber metropolitan network. *Review of scientific instruments*, *77* (6), 064701.
113. **Norris**, R. P. (2010, December). Data challenges for next-generation radio telescopes. In *e-Science Workshops, 2010 Sixth IEEE International Conference on* (pp. 21-24). IEEE.
114. **OFS Optics**. (2017). *TrueWave® RS Optical Fiber* [Specification sheet]. USA.
115. **Ohhara**, T., Yoshimi, T., & Sasaki, W. (2010). Precise frequency stabilization technique for 850-nm vertical cavity surface emitting lasers by controlling their optical beat frequency. In *Proc. SPIE* (Vol. 7597, pp. 759724-1).
116. **Optiphase**. *Fiber Stretchers*. Retrieved October 10, 2017, from <http://www.optiphase.com/products.html>
117. **Percival**, R. (1999). Time and frequency standards. *Applied Microwave and wireless*, *11* (12), 36–48. Retrieved 04 September 2017, from student.agh.edu.pl/~mikro/pliki/Applied%20Microwave%20and%20Wireless.xls
118. **Petrov**, A. A., & Davydov V. V. (2015). Improvement Frequency Stability of Caesium Atomic Clock for Satellite Communication System. In. Balandin S.,

- Andreev S. & Koucheryavy Y. (Eds). Internet of Things, Smart Spaces, and Next Generation Networks and Systems, *Springer, Cham, 9247, 739-744.*
119. **Poole**, C. D., & Nagel, J. (1997). Polarization effects in lightwave systems. In Kaminow, I. P., & Koch, T. (Ed.), *Optical Fiber Telecommunications IIIA*, (pp. 114-161). California: Academic Press.
120. **Poole**, I. *PLL Phase Locked Loop Tutorial*. Retrieved October 18, 2017, from <http://www.radio-electronics.com/info/rf-technology-design/pll-synthesizers/phase-locked-loop-tutorial.php>
121. **Predehl**, K., Grosche, G., Raupach, S. M. F., Droste, S., Terra, O., Alnis, J., ... & Schnatz, H. (2012). A 920-kilometer optical fiber link for frequency metrology at the 19th decimal place. *Science*, 336 (6080), 441-444.
122. **Raghunathan**, V., Claps, R., Dimitropoulos, D., & Jalali, B. (2004). Wavelength conversion in silicon using Raman induced four-wave mixing. *Applied Physics Letters*, 85 (1), 34-36.
123. **Ramamurthy**, B., & Mukherjee, B. (1998). Wavelength Conversion in WDM Networking. *IEEE Journal on Selected Areas In Communications*, 16 (7), 1061- 1073.
124. **Rashleigh**, S. C. (1983). Origins and Control of Polarization Effects in Single-Mode Fibers. *IEEE Journal of Lightwave Technology, LT-1* (2), 312-331.
125. **Rawlings**, S., Abdalla, F. B., Bridle, S. L., Blake, C. A., Baugh, C. M., Greenhill, L. J., & van der Hulst, J. M. (2004). Galaxy evolution, cosmology and dark energy with the Square Kilometer Array. *New Astronomy Reviews*, 48, 1013-1027.
126. **Raycan**. (2015). *1310 nm Vertical-Cavity Surface Emitting Laser RC24xxx1-Fft* [Data Sheet]. 100615 v1.1. Daejon, Korea: Raycan.

127. **Raycan.** (2015). *1550 nm Vertical-Cavity Surface Emitting Laser RC34xxx1-Fft* [Data Sheet].140616 v1.1. Daejon, Korea: Raycan.
128. **Razavi,** B. (1996). A study of phase noise in CMOS oscillators. *IEEE Journal of Solid-State Circuits*, 31 (3), 331–343.
129. **Riley,** W. J. (2008). *Handbook of Frequency Stability Analysis*. Washington: U. S. Government Printing Office.
130. **Rotich,** E. K. (2015). *Fibre Optic Network Supporting High Speed Transmission in the Square Kilometre Array, South Africa*. Unpublished doctoral thesis, Nelson Mandela Metropolitan University, Port Elizabeth, South Africa.
131. **Rubiola,** E. (2009). *Phase Noise and Frequency Stability in Oscillators*. New York: Cambridge University Press.
132. **Rutman,** J. (1978). Characterization of Phase and frequency instabilities in precision frequency sources: Fifteen years of progress. *Proceedings of the IEEE*, 66 (9), 1048-1075.
133. **Sato,** K. (1994). Transport network evolution with optical paths. *Proceedings of ECOC, September 1994, Italy*, 2, 919-926.
134. **Sato,** K., Hara, T., Kuji, S., Asari, K., Nishio, M., & Kawano, N. (2000). Development of an Ultrastable Fiber Optic Frequency Distribution System Using an Optical Delay Control Module. *IEEE Transactions On Instrumentation And Measurement*, 49 (1), 19-24.
135. **Sato,** K., Okamoto, S., & Hadama, H. (1994). Network Performance and Integrity Enhancement with Optical Path Layer Technologies. *IEEE Journal on Selected Areas in Communications*, 12, 159-170.

136. **Schediwy**, S. W., Gozzard, D., Baldwin, K. G., Orr, B. J., Warrington, R. B., Aben, G., & Luiten, A. N. (2013). High-precision optical-frequency dissemination on branching optical-fiber networks. *Optics Letters*, 38 (15), 2893-2896.
137. **Schilizzi**, R. (2013). *SKA SADT Technical Development Plan*. SKA Organization. Retrieved August 10, 2017 from http://skatelescope.org/wp-content/uploads/2013/09/SKA-TEL-SADT-PROP_TECH-001_Redacted_final_24Sept13.pdf.
138. **Schilizzi**, R. T., Alexander, P., Cordes, J. M., Dewdney, P. E., Ekers, R. D., Faulkner, A. J., Gaensler, B. M., Hall, P. J., Jonas, J. L., & Kellermann, K. I. (2007). Preliminary Specifications for the Square Kilometre Array. Retrieved August 8, 2017 from https://www.skatelescope.org/uploaded/5110_100_Memo_Schilizzi.pdf.
139. **Schilizzi**, R. T., Dewdney, P. E. F., & Lazio, T. J. W. (2008). The Square Kilometre Array. *Proceedings of SPIE*, 7012, 70121I-1- 70121I-13.
140. **Shillue**, W., Grammer, W., Jacques, C., Brito, R., Meadows, J., Castro, J., Banda, J., & Masui, Y. (2011). The ALMA Photonic Local Oscillator System. *Proceedings of USRI General Assembly and Scientific Symposium*, 1–4.
141. **SKA Africa**. (2013). Our Journey to bring the SKA to Africa. Retrieved August 4, 2017 from http://www.ska.ac.za/download/our_journey_brochure.pdf.
142. **SKA Organization**. (2011). The Square Kilometre Array Fact sheet for industry. Retrieved August 4, 2017 from http://skatelescope.org/wp-content/uploads/2011/05/SKA_Factsheet-for-Industry_May2011_web.pdf.
143. **SKA Organization**. Retrieved November 29, 2017 from <https://skatelescope.org/sadt/>

144. **SKA Organization.** Retrieved November 29, 2017 from <https://skatelescope.org/signal-processing/>
145. **SKA.** (2017). Participating Countries. Retrieved August 3, 2017 from <http://skatelescope.org/participating-countries/>.
146. **SKA.** (2017). The History Of The SKA Project. Retrieved August 2, 2017 from <http://skatelescope.org/history-of-the-skaproject/>.
147. **Sliwczynski, Ł., Krehlik, P., Buczek, Ł., & Lipinski, M.** (2011). Active propagation delay stabilization for fiber-optic frequency distribution using controlled electronic delay lines. *IEEE Transactions on Instrumentation and Measurement*, 60 (4), 1480-1488.
148. **Sokoloff, D. D., Bykov, A. A., Shukurov, A., Berkhuijsen, E. M., Beck, R., & Poezd, A. D.** (1998). Depolarization and Faraday effects in galaxies. *Royal Astronomical Society*, 299 (1), 189–206.
149. **Stein, S. R.** (1985). Frequency and Time-Their Measurement and Characterization. In Gerber, E.A. & Ballato, A. (Eds). *Precision Frequency Control*, 2, Academic Press, New York, Academic Press, 191-416.
150. **Stubkjaer, K.E., Mikkelsen, B., Joergensen, C., Danielsen, S. L., Vaa, M., Pedersen, R. J., et al.** (1997). Wavelength Conversion Technology. In Prati G. (Ed.), *Photonic Networks.: Advances in Optical Communications*, (pp 103-117). London Springer.
151. **Sullivan, D., Allan, D., Howe, D., & Walls, F.** (Eds). (1990). *Characterization of clocks and oscillators* [NIST Tech Note 1337]. Washington: U. S. Government Printing Office.
152. **Tavella, P.** (2008). Statistical and mathematical tools for atomic clocks. *Metrologia*, 45 (6), S183-S192.

153. **Taylor**, A. R., & Braun, R. (Eds.). (1999). *Science with the Square Kilometer Array*. Dwingeloo: Netherlands Foundation for Research in Astronomy.
154. **Tratnik**, J., Lemut, P., Dragonja, U., Batagelj, B., & Vidmar, M. (2013). Distribution of RF-clock signal over single optical fiber with temperature-drift and vibration compensation. In *Microwave Photonics (MWP), 2013 International Topical Meeting, IEEE*, October 2013 (pp. 162-165).
155. **Turner**, W. (2014). *SKA Phase 1 System (Level 1) Requirements Specification*. SKA Organization. Retrieved August 9, 2017 from http://skatelescope.org/wp-content/uploads/2014/03/SKA-TEL-SKO-0000008-AG-REQ-SRS-Rev06-SKA1_Level_1_System_Requirement_Specification-P1-signed.pdf.
156. **Vanier**, J., & Tétu, M. (1978). Time Domain Measurements of Frequency Stability. *Proceedings of the 10th Annual Precise Time and Time Interval (PTTI) Applications and Planning Meeting*. November, 1978, Maryland, 247-291.
157. **Wang**, B., Gao, C., Chen, W. L., Miao, J., Bai, Y., Li, T. C., & Wang, L. J. (2012). Fiber-based time and frequency dissemination between THU and NIM. In *IEEE International Frequency Control Symposium (FCS), May, 2012*, 1-4.
158. **Wang**, B., Gao, C., Chen, W. L., Miao, J., Zhu, X., Bai, Y., ... & Wang, L. J. (2012). Precise and continuous time and frequency synchronisation at the 5×10^{-19} accuracy level. *Scientific Reports*, 2, 1-5.
159. **Wang**, B., Gao, C., Chen, W. L., Zhang, J. W., Feng, Y. Y., Li, T. C., & Wang, L. J. (2012, May). A 10– 18/day fiber-based RF frequency dissemination chain. In *Lasers and Electro-Optics (CLEO), 2012 Conference on* (pp. 1-2). IEEE.

160. **Wang**, B., Zhu, X., Gao, C., Bai, Y., Dong, J. W., & Wang, L. J. (2015). Square kilometre array telescope—precision reference frequency synchronisation via 1f-2f dissemination. *Scientific reports*, 5.
161. **Wassin**, S., Isoe, G. M., Gamatham, R. R. G., Leitch, A. W. R., & Gibbon, T. B. (2017). Highly Accurate Pulse-Per-Second Timing Distribution over Optical Fibre Network using VCSEL Side Mode Injection. *Proceedings of SPIE, January, 2017, USA, 10129*, 101290G-1-101290G-12.
162. **Whiiten**, W. B. (1980). Time delay multiplexing of optical spectra with a fiber optic array. *Analytical Chemistry*, 52 (14), 2355–2357.
163. **White**, R. L., Becker, R. H., Fan, X., & Strauss, M. A. (2003). Probing the Ionization State of the Universe at $z > 6^*$. *The Astronomical Journal*, 126 (1), 1-14.
164. **Wilcox**, R., Byrd, J. M., Doolittle, L., Huang, G., & Staples, J. W. (2009). Stable transmission of radio frequency signals on fiber links using interferometric delay sensing. *Optics Letters*, 34 (20), 3050-3052.
165. **Ye**, J., & Cundiff, S. T. (Eds.). (2005). *Femtosecond Optical Frequency Comb: Principle, Operation, and Applications*. Massachusetts, Kluwer Academic Publishers/Springer.
166. **Ye**, J., Peng, J. L., Jones, R. J., Holman, K. W., Hall, J. L., Jones, D. J., ... & Hollberg, L. W. (2003). Delivery of high-stability optical and microwave frequency standards over an optical fiber network. *Journal of the Optical Society of America B*, 20 (7), 1459-1467.